

SINTERING MECHANISMS AND SURFACE DIFFUSION  
FOR ALUMINUM OXIDE

by

JOSEPH MICHAEL DYNYS

B.S. Alfred University (1976)

B.A. Alfred University (1976)

SUBMITTED IN PARTIAL FULFILLMENT  
OF THE REQUIREMENTS FOR THE  
DEGREE OF

DOCTOR OF PHILOSOPHY


at the

MASSACHUSETTS INSTITUTE OF TECHNOLOGY


February 1982

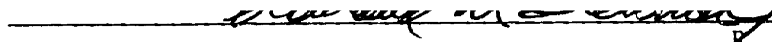
© Massachusetts Institute of Technology

Signature of Author


  
Department of Materials Science and Engineering  
January 8, 1982

Certified by

  
R. L. Coble  
Thesis Supervisor

  
R. M. Cannon  
Thesis Supervisor

Accepted by

  
Regis M. Pelloux  
Chairman, Department Committee on Graduate Students

Archives

MASSACHUSETTS INSTITUTE  
OF TECHNOLOGY

MAY 3 1982

LIBRARIES

SINTERING MECHANISMS AND SURFACE DIFFUSION FOR  
ALUMINUM OXIDE

by

JOSEPH MICHAEL DYNYS

Submitted to the Department of Materials Science and Engineering on January 8, 1982 in partial fulfillment of the requirements for the degree of Doctor of Philosophy.

ABSTRACT

Studies reporting surface diffusivities for  $Al_2O_3$  materials are extensively reviewed, including the measurement techniques, data analysis, experimental procedures, and sample purity levels. The preferred techniques are either thermal grooving or multiple scratch smoothing. For  $1600 < T < 1800^\circ C$ , a ranking of these results suggests that purer samples have lower surface diffusivities.

Surface diffusivities for  $Al_2O_3$  were determined by studying the thermal grooving of grain boundaries on Lucalox<sup>®</sup> and three different grades of high purity materials. Most samples were embedded in powder of nominally the same composition and annealed in air and in vacuum at temperatures between 900 and  $1840^\circ C$  for times ranging from 1 to 5496 hours.

The calculated surface diffusivities are non-Arrhenius. For  $T < 1300^\circ C$ , the implied surface diffusivities for the pure and Lucalox materials are similar in magnitude and variability, and adequately described by an activation energy of  $\sim 65$  kcal/mole. For  $T > 1400^\circ C$ , the surface diffusivities for the pure and Lucalox materials are described by lines with activation energies of 125 kcal/mole and  $\sim 165$  kcal/mole, respectively. Implied surface diffusivities are lower for the purer materials at  $T \geq 1600^\circ C$ .

Variable thermal grooving rates were observed for all samples. Although impurities are also important, the variability is primarily attributed to the orientation dependencies of the surface diffusivity and surface energy. More variability was found for the lower temperature anneals.

Surface diffusivities calculated from the grooving data vary widely. Most of the variability results from using models which assume that the surface energy ( $\gamma$ ) and surface diffusivities ( $D_s$ ) are isotropic. It is shown that the coefficient in the thermal grooving model depends on the anisotropy in both  $\delta$  and  $D_s$ . Consequently, the absolute variability in  $D_s$  cannot be determined from thermal grooving data.

Faceting is found on most samples. A discussion of the importance of this with respect to the measurement of the thermal groove widths and its influence on the grooving kinetics is presented. Where extensive faceting developed on pure alumina samples, at 1600°C, the thermal grooving kinetics did not indicate control by surface or lattice diffusion (i.e.,  $d \log W/d \log t \ll 1/4$  or  $1/3$ , respectively). Slow diffusion on the facet planes or slow facet translation (adding layers to or subtracting layers from the facet plane) are postulated as rate controlling steps.

The development and types of faceting depend on the purity of the alumina material, and on the annealing temperature. Evidence suggests that the amount of faceting is reduced by preventing the loss of MgO from samples deliberately doped with magnesia (Lucalox materials). Calcia and silica impurities must also be present for MgO to be effective in reducing the amount of faceting, as deduced from comparisons of the Lucalox materials with pure and MgO-doped pure materials.

Initial stage sintering mechanisms are considered using the surface diffusivities from this study and literature values for boundary and lattice diffusion coefficients. Boundary diffusion is the dominant mass transport mechanism. Surface redistribution of mass (transported by boundary diffusion) could control sintering for orientations or sample compositions with low surface diffusivity.

Thesis Supervisors: Robert L. Coble  
Title: Professor of Ceramics

Rowland M. Cannon  
Title: Associate Professor of Ceramics

TABLE OF CONTENTS

<u>Chapter</u>		<u>Page</u>
	TITLE PAGE	1
	ABSTRACT	2
	TABLE OF CONTENTS	4
	LIST OF FIGURES	8
	LIST OF TABLES	10
	ACKNOWLEDGEMENTS	11
I	INTRODUCTION	12
II	LITERATURE REVIEW	13
	A. Models, Assumptions and Data Analysis	13
	1. Driving Forces	13
	2. Thermal Grooving	16
	3. Multiple Scratch Smoothing	20
	4. Single Scratch Smoothing	22
	5. Cylindrical Void Instability	24
	6. Sintering by Surface Diffusion	26
	7. The Growth of an Isolated Linear Facet	27
	8. Errors Associated with the Analysis of Thermal Grooving	32
	B. Studies Reporting Surface Diffusion Coefficients	38
	1. Thermal Grooving	38
	2. Multiple Scratch Smoothing	47
	3. Single Scratch Smoothing	51
	4. Cylindrical Void Instability	52
	5. Sintering	56
	6. Summary of the Literature Review	59

TABLE OF CONTENTS (Cont'd.)

<u>Chapter</u>		<u>Page</u>
III	GOALS OF THIS THESIS RESEARCH	63
IV	EXPERIMENTAL PROCEDURES	64
	A. Sample Preparation	64
	1. Materials	64
	2. Polishing	66
	3. Acid Washings	73
	4. Specimen Configuration and Anneals	73
	B. Measurement of Groove Width and Depth	75
V	RESULTS	80
VI	ANALYSIS OF RESULTS	93
	A. Microstructure Characterization	93
	1. Composition	93
	(a) Auger Electron Spectroscopy Results	93
	(b) Second Phases	95
	2. Surface Morphology	98
	(a) Factors Affecting the Measurement and Variability of Thermal Groove Widths	98
	(b) Observations on Faceting	107
	(c) Simultaneous Free Evaporation	120
	B. Time Dependence	120
	C. Dihedral Angle Determinations	133
	D. Diffusion Coefficients	135

TABLE OF CONTENTS (Cont'd.)

<u>Chapter</u>		<u>Page</u>
VII	DISCUSSION	141
	A. Variability in the Thermal Groove Widths	141
	1. Groove Width Variability Due to Grain Boundary Migration	141
	2. Groove Width Variability Due to an Initial Thermal Groove Width	142
	3. Effects of Faceting on the Thermal Grooving Process	143
	(a) Altered Geometry Considering Volume Conservation in 2-d	143
	(b) Effect of Faceting on Mass Transport in 2-d	144
	4. Variability in the Groove Width Due Only to Anisotropy in Surface Diffusion	151
	5. Impurity Effects on the Surface Tension and Diffusivities	153
	B. Dihedral Angles	155
	C. Interpretation of Grooving Behavior for Temperature $>1500^{\circ}\text{C}$	155
	D. Interpretation of Grooving Behavior for Temperatures $<1500^{\circ}\text{C}$	159
	E. Summary of Surface Diffusivities	161
	F. Dependence of Faceting on Impurities	163
	G. The Role of Surface Diffusion in Initial State Sintering	165
VIII	CONCLUSIONS	169
IX	SUGGESTIONS FOR FUTURE WORK	171
X	REFERENCES	172

TABLE OF CONTENTS (Cont'd.)

<u>Chapter</u>		<u>Page</u>
APPENDIX I	Mechanisms of Atom Transport During Initial Stage Sintering	175
APPENDIX II	Correction for the Specimen Tilt in the SEM	190
APPENDIX III	Comparison of Thermal Groove Widths Measured by the SEM-Technique with Two-Beam Interferometry	192
APPENDIX IV	Correction for the Temperature Drift in Experiments GBG27 and GBG29	193
BIOGRAPHICAL NOTE		195

LIST OF FIGURES

<u>Figure</u>		<u>Page</u>
1	Log $\omega D_s$ versus $1/T$	14
2	Schematic of Thermal Grooving	17
3	Schematic of Multiple Scratch Smoothing	21
4	Schematic of Single Scratch Smoothing	23
5	Linear Faceting Geometry	28
6	Linear Faceting Geometry and Chemical Potentials	28
7	$K^*$ for Linear Faceting	30
8	Errors in Analyzing Thermal Grooving Data	33
9	Sample Configuration	74
10	SEM Correction Geometry	77
11	Limit of Resolution for the SEM-Technique	81
12	Near Limit of Resolution for the SEM-Technique	81
13	Second Phase on Sample GBG27	96
14	Second Phase on Sample GBG24	96
15	Thermal Grooving on Sample GBG11	99
16	Thermal Grooving on Sample GBG12	100
17	Thermal Grooving, Interferogram, Schematic Facet Profile	101
18	Thermal Grooving on Sample GBG15	104
19	Thermal Grooving on Sample GBG16	105
20	Thermal Grooving on Sample GBG27	106
21	Interferograms on Sample GBG27	108
22	Thermal Grooving on Sample GBG17	112
23	Thermal Grooving on Sample GBG29	113
24	Thermal Grooving on Sample GBG28	115
25	Thermal Grooving on Sample GBG6	117



LIST OF FIGURES (Cont'd.)

<u>Figure</u>		<u>Page</u>
26	Thermal Grooving on Sample GBG11	118
27	Thermal Grooving on Sample GBG12	118
28	Thermal Grooving on Sample GBG25	119
29	Log W versus Log time for 1300°C Annealings	122
30	Log W versus Log time for 950°C Annealings	123
31	Log W versus Log time for Specific Boundaries, GBG27	124
32	Log W versus Log time for Specific Boundaries, GBG29	128
33	Log $\omega D_s$ versus $1/T$	137
34	Log $D_L$ versus $1/T$	138
35	$W/W_{iso}$ versus $\alpha$	145
36	Single Facet on a Thermal Groove Profile	147
37	Multiple Faceted Thermal Groove	148
38	Log $\omega D_s$ versus $1/T$ , estimates of lines representing data	162
39	Log $\omega D_s$ versus $1/T$ , boundary versus surface diffusion controlled sintering	166
40	Log $\delta D_b$ versus $1/T$	168

LIST OF TABLES

<u>Table</u>		<u>Page</u>
I	Literature Data Ranked by Decreasing Magnitude of $\omega D_s$ for Temperatures of 1500 to 1800°C	60
II	Samples Used in Thermal Grooving Experiments	65
III	Experimental Procedures	67
IV	Thermal Groove Width for Individual Boundaries as a Function of Time for the LD Material GBG27	83
V	Thermal Groove Width of Individual Boundaries as a Function of Time for ADL, GBG29	85
VI	Summary of Grain Boundary Grooving Results	86
VII	Measured and Calculated Dihedral Angles	91
VIII	Auger Results	92
A1	Comparison of Thermal Groove Widths Measured by the SEM-Technique with Two-Beam Interferometry	192
A2	Ratios Showing the Increased Thermal Groove Width Due to a Step Increase of 15°C for a Surface or Lattice Diffusion Process Assuming Plausible Activation Energies	194

### ACKNOWLEDGEMENTS

I wish to thank Professors R. L. Coble and R. M. Cannon for their continued support during the course of this work and for the exposure to a broad range of materials problems not related to this thesis.

The assistance of my friends during the battle to finish this work is gratefully acknowledged here. Special thanks go Pat Kearney for shooting the slides and micrographs, to Carol Handwerker, Elaine Rothman, and John Blendell for proofreading and keeping my sanity, to Tom Coyle for drafting, and to Linda Sayegh for her skillful typing of this manuscript. My managers at IBM, Rao Tummala and Charles Perry, are also thanked for their understanding and allowing time to finish this manuscript.

I also wish to thank a number of friends for the times of fun and also for numerous enlightening discussions, including Mike Barsoum, Bill Coblenz, Dave Cranmer, Todd Gattuso, Andy Glaeser, Tom Ketcham, Rico, Rock, Ellen Tormey, Bill Tasker, Yo Tajima and those I have failed to mention.

Finally, and most importantly, I wish to extend my deepest appreciation to my wife, Shelley, for her patience and encouragement during this work.

This research was funded by the Department of Energy.

## I. INTRODUCTION

Many sintering studies have been conducted on alumina over the last twenty years. Although the sintering of alumina is generally thought to occur by solid state diffusion over most of the conditions of interest, there is no consensus regarding the dominant or rate controlling transport path. Furthermore, there are no adequate explanations for the effects of additives, such as MgO, on the sintering behavior of  $\text{Al}_2\text{O}_3$ . There are several reasons for this state of affairs: (1) disagreement has existed as to the "proper" sintering model for each transport path, (2) the data base for the mass transport coefficients is incomplete and unreliable, and (3) complications from size distribution effects, packing irregularities, and particle rearrangement make interpretation of sintering behavior of powder compacts difficult. Further discussion of these is included in Appendix I.

Within the data base on aluminum oxide, surface diffusion is the most poorly understood. For this reason, this thesis critically reviews existing data, presents the results of a series of experiments which define limits on the values for surface diffusion over a broad temperature range, and discusses the problems and uncertainties inherent for this material and for the type of experiments used.

## II. LITERATURE REVIEW

### A. Models, Assumptions and Data Analysis

There are two principal methods for determining surface diffusion coefficients: measurement of the spreading of tracer atoms along a surface or by measurement of the mass transport for a process where surface diffusion is responsible. The diffusivity of a specific element results from tracer studies while the latter methods determine a phenomenological diffusion coefficient. Only mass transport methods have been investigated on alumina. The processes from which surface diffusivities have been deduced include: thermal grooving, multiple scratch smoothing, single scratch decay, the breakup of cylindrical voids, and sintering kinetics.

Those results do not present a clear indication of the value of the surface diffusivity over any temperature range, see Figure 1. There are many reasons for these disagreements including samples of varying purities, anisotropy in the surface energy or faceting, variance due to a wide range of experimental procedures and environments and in some cases misinterpretation of data. For these reasons, a brief description of driving forces, model assumptions and data analysis is presented prior to a detailed review of all reported studies on surface diffusion on alumina. A review of the linear faceting process is also included as it is important in data interpretation.

#### 1. Driving Forces

The mass transport processes of interest are caused by capillarity forces or surface excess free energy, commonly referred to as surface

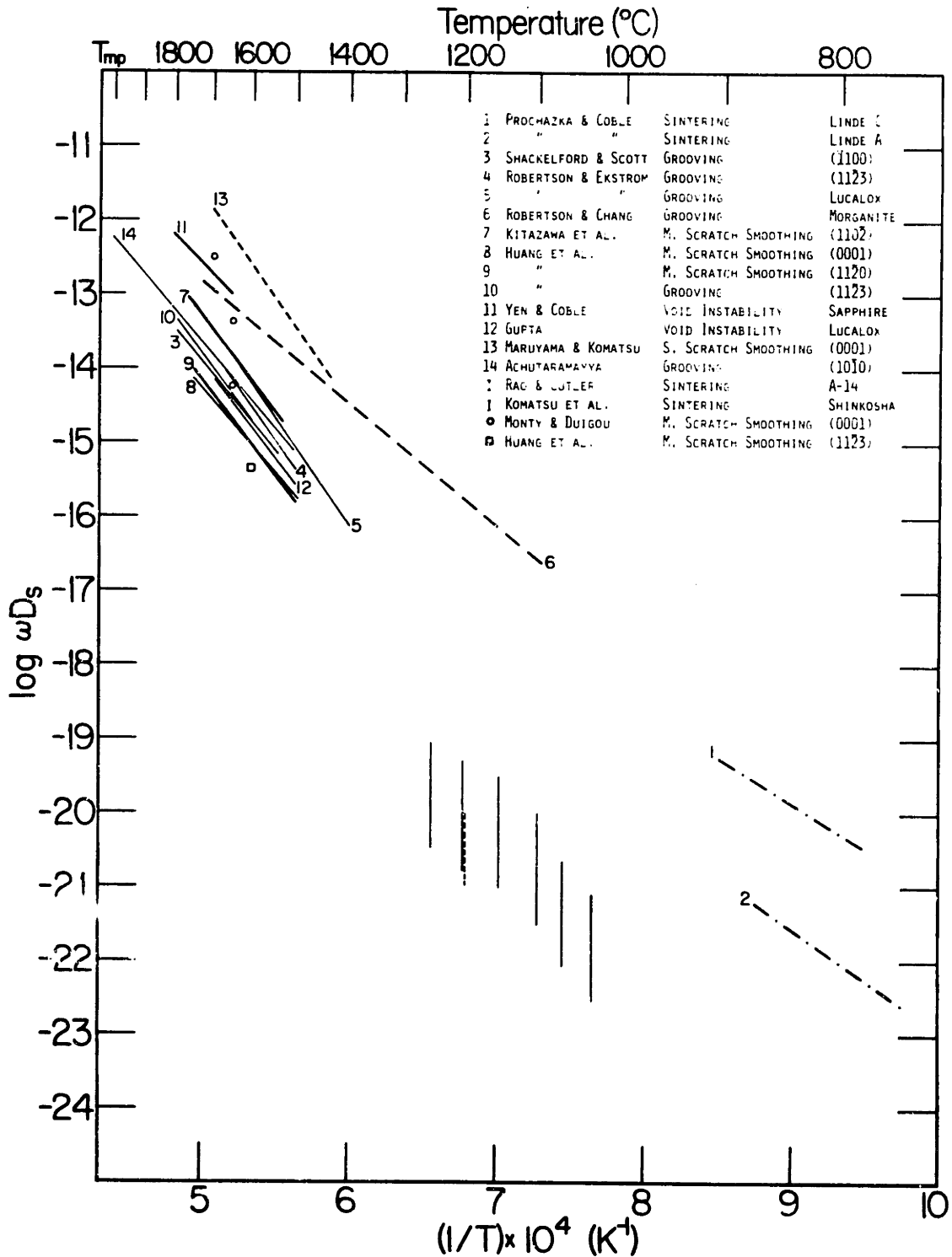


Figure 1 - Log ωDs versus 1/T. Summary of literature values.

tension. Herring (1951) has shown that the chemical potential of surface atoms is related to the surface tension and surface curvature:

$$\mu - \mu_h - \mu_o = \Omega \left[ \left( \gamma + \frac{\partial^2 \gamma}{\partial n_x^2} \right) K_1 + \left( \gamma + \frac{\partial^2 \gamma}{\partial n_y^2} \right) K_2 \right] \quad (1)$$

where  $\mu$ ,  $\mu_h$ , and  $\mu_o$  are the chemical potentials of atoms, vacancy type defects, and atoms on a flat surface, respectively;  $\Omega$  is a molar volume,  $\gamma$  is the local surface tension;  $n_i$  is the component in the  $i$ -direction of a unit normal vector; and  $K_i$  is the curvature with respect to the  $i$ -direction where  $K > 0$  for a convex surface,  $K = 0$  for a flat surface, and  $K < 0$  for a concave surface. This equation is valid for a one component, stress free solid in equilibrium with its vapor. Note, however, that chemical potential is not defined by this equation for flat surfaces at which there are cusps in  $\gamma$ -plots.

The flux of surface atoms is related to the gradient in  $K$  along the surface by the Nernst-Einstein equation; where there is only 1 component of curvature or  $\gamma'' = 0$ , then, after Mullins (1957, 1963):

$$J = \frac{-D_s(\gamma + \gamma'')\Omega n_s}{kT} \nabla_s K \quad (2)$$

Here  $D_s$  is the surface diffusion coefficient,  $n_s$  the number of diffusing atoms per unit area, and  $kT$  has its usual meaning. By multiplying the divergence of the surface flux by  $\Omega$ , the governing differential equation relating the velocity of the surface element along its normal to the surface diffusion coefficient results:

$$V_n = B \nabla_s^2 K \quad (3)$$

where

$$B = \frac{D_s (\gamma + \gamma'') \Omega^2 n_s}{kT} = \frac{D_s (\gamma + \gamma'') \Omega}{kT} \quad (4)$$

Conventionally,  $n_s$  is taken as  $\Omega^{-2/3}$  which is not necessarily true. In this thesis, the quantity  $\omega$  is used as an effective surface thickness,  $\omega = n_s \Omega \approx \Omega^{1/3}$ , which is treated as unseparable from the calculated surface diffusion coefficients; the quantity  $\omega D_s$  is therefore often referred to as the surface diffusivity instead of the surface width-diffusivity product. Many surface diffusion controlled mass transport processes have been solved by applying the appropriate boundary conditions and geometrical expressions to Equation (3). Where the problems are sufficiently well prescribed and the solutions sufficiently accurate, the kinetics of these processes may be used to determine  $\omega D_s$ .

## 2. Thermal Grooving

Thermal or grain boundary grooving is a mass transport process that is initiated by the requirement that all surface tensions and associated torque terms balance along a common line of intersection, as shown by Herring (1951)

$$\sum_{i=1}^3 (\gamma_i \hat{t}_i + \partial \gamma_i / \partial \hat{t}_i) = 0 \quad (5)$$

Here  $\gamma_i$  is the surface or grain boundary tension and  $\hat{t}_i$  a unit tangent vector for the  $i$ -surface at the line of intersection. This expression is greatly simplified for the case of a grain boundary normal to an isotropic surface:

$$\gamma_b = 2\gamma_s \sin \beta = 2\gamma_s \cos \theta/2 \quad (6)$$



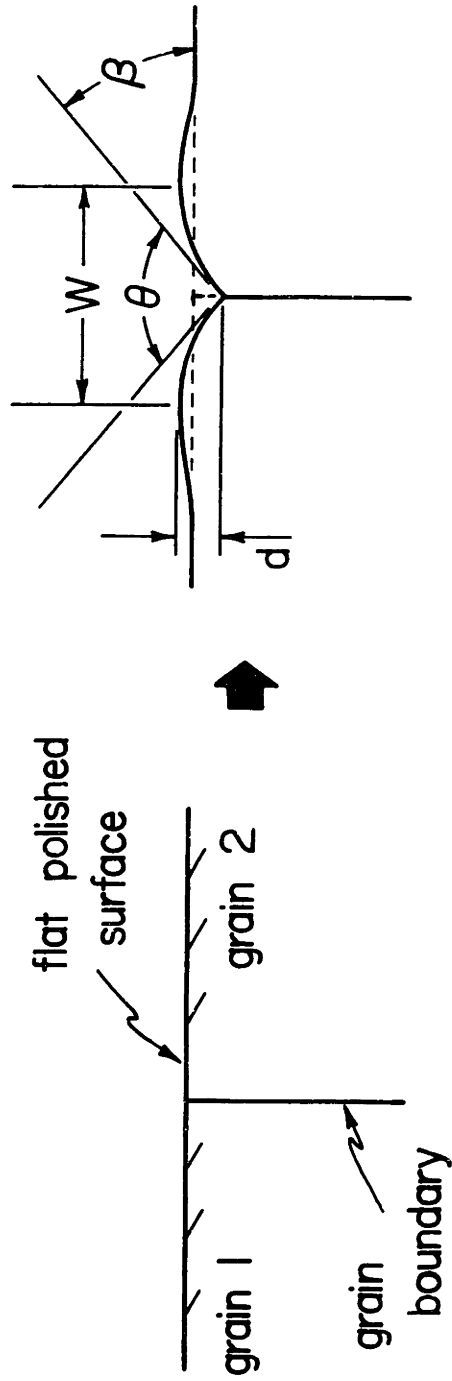


Figure 2 - A Schematic of the Thermal Grooving Process

where  $\gamma_b$  and  $\gamma_s$  are the grain boundary and solid-vapor surface tensions;  $\beta$  is the angle between the flat grain surface and the surface tangent at the groove root, and  $\theta$  is the dihedral angle. Equation (6) defines a boundary condition for the solution to the thermal grooving problem, (Mullins (1957, 1963)). The process occurs in the following manner. Where a grain boundary intersects a flat free surface (as shown in Figure 2), an imbalance in the surface tensions occurs, and atoms migrate from this region in order to satisfy this inequality. Consequently, ridges or humps with positive curvature form on both sides of the boundary. These ridges flatten out in response to the surface curvature gradient, thereby tending to upset the equilibrium at the groove root. Thus, mass continually diffuses from the groove root area towards the flat surface resulting in a self-sustaining process.

Mullins has solved for the geometry and kinetics of thermal groove formation due to surface diffusion at constant temperature. The results show that the profile shape remains constant with the equilibrium value of  $\beta$  maintained at the intersection of the grain boundary with the free surface, Figure 2. The width and depth, defined in Figure 2, grow as:

$$W = 4.6 (Bt)^{1/4} \quad (7)$$

$$d = 0.973m (Bt)^{1/4} \quad , \quad (8)$$

where  $W$  is the thermal groove width defined by the distance between the groove hump maxima;  $d$  is the groove depth and  $m = \tan \beta$ . These derivations assume a small slope at the groove root,  $m \leq 0.3$ , and that  $(\gamma + \gamma'')$  is a smoothly varying, continuous function over the exposed surface.

Robertson (1971) has reported values for the numerical coefficients

in equations (7) and (8) for  $0 \leq m \leq 4.0$ . These calculations show that the groove width is relatively insensitive to the dihedral angle; the error in using equation (7) is <5% for  $m \leq 4.0$  and <2% for  $m \leq 0.7$ . The groove depth, however, is quite dependent on the dihedral angle; errors of >10% result from using equation (8) to predict the depth for  $m > 0.7$ .\* Therefore, the use of equation (7) to calculate  $\omega D_s$  values is justifiable over a broad range of dihedral angles while equation (8) should be used with caution. Additionally, dihedral angles calculated from the combination of equations (7) and (8) are incorrect for large  $m$ ; they are larger than the true values. For instance, the calculated angle is approximately  $5^\circ$  larger than a true value of  $110^\circ$ ; for dihedral angles of  $150^\circ$ , the difference is less than  $1^\circ$ .

Solutions for thermal grooving by volume diffusion,  $D_L$ , have also been derived by Mullins (1960). The profile shape is nearly identical to that formed by surface diffusion and:

$$W = 5.0 (Ct)^{1/3} \quad (9)$$

$$d = 1.01m (Ct)^{1/3} \quad (10)$$

where

$$C = \frac{D_L (\gamma + \gamma'') \Omega}{kT} \quad (11)$$

Thermal grooving experiments typically involve polishing a bicrystal or polycrystalline sample to a flat surface, followed by isothermal annealings. Groove widths and depths are measured at specific times between or during the anneals. Data analysis involves plotting  $\log(W$  or  $d)$  versus  $\log t$  where the slope on this plot,  $d\log(W$  or  $d)/d\log t$ ,

---

\* For  $m = 0.7$ , the dihedral angle,  $\theta$ , is  $110^\circ$ ; for  $m = 0.5$ ,  $\theta \approx 127^\circ$ .

indicates the appropriate diffusion mechanism. Alternatively, linear plots of  $W$  or  $d$  against  $t^{1/n}$  may be used; if a single mechanism is operative over the entire time interval, a straight line representing the data should pass through the origin. Negative intercepts may be attained using  $n=4$  when volume diffusion is contributing significantly to the grooving process; likewise, positive intercepts may result for  $n=3$  where surface diffusion is an important mechanism.

### 3. Multiple Scratch Smoothing

Multiple scratch smoothing (MSS) involves measuring the amplitude decay of a sinusoidal profile etched into the surface of a single crystal, Figure 3. Again, Mullins (1963) described the physics of the process. The time dependent amplitude is

$$A(t) = A_0 \exp \left[ -(B\omega_s^4 + C\omega_s^3)t \right] = A_0 \exp -k't \quad , \quad (12)$$

where  $\omega_s = 2\pi/\lambda$ ;  $A_0$  is the initial amplitude;  $\lambda$ , the wavelength of the sinusoidal profile; and  $k'$ , a kinetic coefficient. This solution, as in thermal grooving, is valid only for small slopes of the surface, i.e.,  $A\omega \ll 1$ . Note also that amplitude growth occurs for  $(\gamma+\gamma'') < 0$ , amplitude decay results when  $(\gamma+\gamma'') > 0$ , and that the shape remains sinusoidal only if  $\gamma''$  is constant which usually means  $\gamma'' = 0$ .

In multiple scratch smoothing experiments, the periodic profiles are usually produced by masking and etching techniques. Since the resulting profile is nonsinusoidal (Figure 3) a smoothing heat treatment is required. Further annealing results in continued amplitude change. Data analysis may be performed by calculating  $k'$  from the variation of

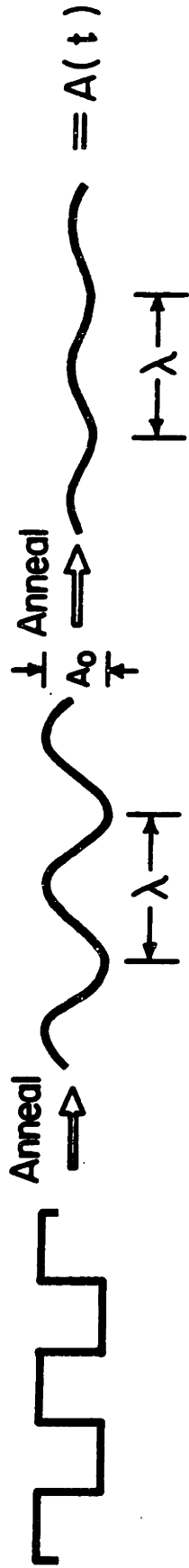


Figure 3 A Schematic of Multiple Scratch Smoothing

$\ln A/A_0$  with time, then determining the dependence of  $k'$  on  $\lambda$ . Alternatively, a slope-intercept analysis may be done using:

$$S = \frac{-d \ln A/A_0}{dt} = B\omega_s^4 + C\omega_s^3 \quad (13)$$

Here  $S/\omega_s^3$  is plotted against  $\omega_s$ ; B is the slope and C the intercept. In principle, both B and C can be determined from these kinetic measurements. However, in practice, a limited range of profile wavelengths or scatter in the data may necessitate knowledge of either B or C so that the other may be determined.

#### 4. Single Scratch Smoothing (SSS)

Surface or lattice diffusion coefficients may be deduced from the "healing" of a single, symmetric scratch (Figure 4). As in multiple scratch smoothing, annealing is required in order to form a standardized profile, i.e., one where the small slope approximation is valid and where the shape remains constant. Further annealing results in growth of the distance between the maxima and decay of scratch depth. The equations describing the changes in these dimensions resulting from surface diffusion are:

$$W = 7.0 (Bt')^{1/4} \quad (14)$$

$$d = 0.08 (Bt')^{-3/4} \quad (15)$$

and by volume diffusion:

$$W = 6.22 (Ct')^{1/3} \quad (16)$$

$$d = 0.082 (Ct')^{-1} \quad (17)$$

after King and Mullins (1962) and Mullins (1963). Here  $t' = t_0 + t_{\text{expt}}$

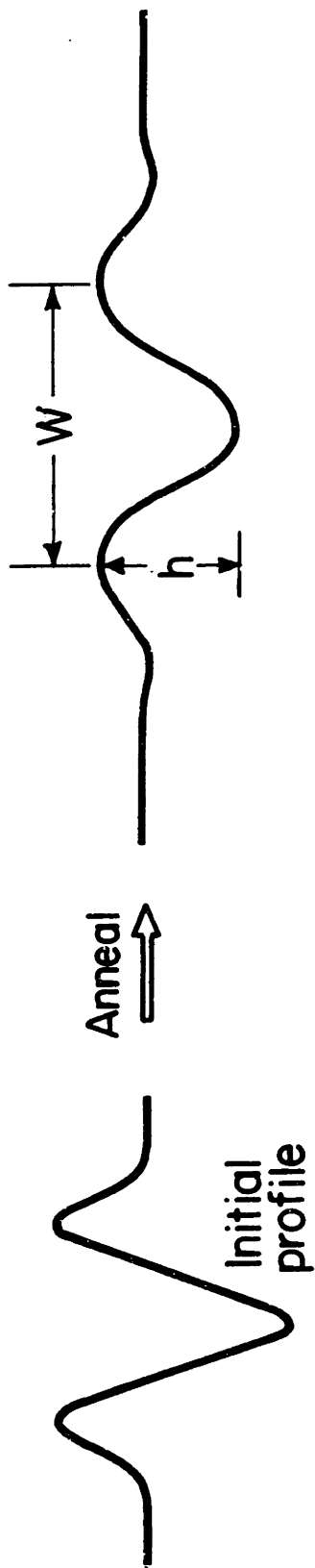


Figure 4 A Schematic of Single Scratch Smoothing

where  $t_{\text{expt}}$  is the experimental time and  $t_0$  is the fictitious time required for the scratch to decay from a delta-function profile to the experimentally observed profile. The term  $t_0$  is deduced, in principle, from taking the ratio of any two data points if it is known or assumed that either a surface or volume diffusion mechanism is controlling. For instance, if the smoothing process is controlled by surface diffusion, the ratio of any pair of data points using equation (14) or (15) should give only one value for  $t_0$ . A plot of  $\log W$  against  $\log t'$  would then have  $\frac{d \log W}{d \log t'} = 1/4$ . If the data show that  $t_0$  is not a constant, nonconformity with the model assumptions or mixed surface and lattice diffusion kinetics may be indicated. For further discussion of this latter situation, see King and Mullins (1962).

### 5. Cylindrical Void Instability

A cylindrical void in a solid is unstable. Nichols (1976) has shown that a finite cylinder with hemispherical ends will form a single spherical pore when the length/diameter (L/D) ratio is  $< 7.2$ ; for  $L/D \geq 7.2$ , the cylindrical void breaks up into a string of "egg-shaped" pores which then spheroidize. This is termed ovulation when the break-up occurs successively from the ends. However, long cylindrical voids may also break up from longitudinal perturbations. Nichols and Mullins (1965b) have determined the wavelength at which the perturbation growth rate is maximum,  $\lambda_m$ , for an infinite cylinder,  $\lambda_m = 8.89r_0 = 4.73r_1$  for surface diffusion, and  $\lambda_m = 12.96r_0 = 6.07r_1$  for volume diffusion, where  $r_0$  is the unperturbed cylindrical radius, and  $r_1$ , the spherical pore radius. The relation between  $r_0$  and  $r_1$  results if the



spacing of the resulting spherical pores,  $\lambda$ , is equal to  $\lambda_m$  as may be anticipated if the cylinders are initially relatively perfect. For break-up of a semi-infinite cylinder by ovulation,  $\lambda = 8.17r_0 = 4.41r_1$  for surface diffusion, after Nichols and Mullins (1965a). A similar analysis for volume diffusion was not done. However, a coefficient in the  $\lambda-r_0$  relationship slightly  $<12.96$  would be expected based on close agreement found for the two processes involving surface diffusion. The time intervals for the ovulation by surface diffusion were also evaluated and found to be nearly equal for two different end conditions: a hemisphere and the "as-ovulated" geometry. The time for each ovulation even on a semi-infinite cylinder is:

$$\tau = \frac{4415}{B} \left( \frac{\pi r_0}{16} \right)^4 . \quad (18)$$

Nichols (1976) has shown that the numerical coefficient in this expression is dependent on the L/D ratio. Nichols' results indicate that use of equation (18) is inappropriate when  $L/D < 13$ , but is reasonably accurate for larger L/D values. The ovulation time for a volume diffusion controlled process was not solved.

A cylindrical void is also unstable to shrinkage. The above solutions assume that this process is negligible and that void volume is conserved. It also neglects void coarsening. These processes may occur by lattice diffusion or by boundary diffusion when the cylindrical void is intersected by a grain boundary. However, shrinkage and coarsening are probably relatively slow compared to spheroidization due to the longer diffusion distances involved. For  $Al_2O_3$ , these processes would be negligible if either process depended on oxygen lattice diffu-

sion. Additionally, the presence of a grain boundary may significantly change the characteristic pore spacings since spherical pores would not be stable for dihedral angles less than  $180^\circ$ . Furthermore, the observed pore spacings will be larger than those predicted, as based on the radius of the apparent cylindrical void, because the cross-section of all pores is lenticular in shape; the lenticular pore radius is larger than the apparent radius. This has the effect of increasing the implied surface diffusivities since  $\omega D_s \propto (\lambda \text{ or } r)^4$ .

#### 6. Sintering by Surface Diffusion

Where surface diffusion is the primary mode of mass transport during sintering, only neck growth between particles in contact occurs initially; as time progresses, particle disappearance caused by the sintering of small, loosely coordinated particles onto larger ones, and coarsening of the pore and particle networks successively become important. As no shrinkage occurs, this entire process is termed coarsening. Shrinkage due to the approach of the centers of particles occurs when boundary or lattice diffusion are important mechanisms. Therefore, the surface area reduction kinetics (without shrinkage) are potentially capable of providing a measure of the surface diffusion coefficient. The initial stage models are simple; the best choice of the many reported models on neck growth by surface diffusion, as discussed by Coblenz et al. (1979), is that due to Nichols and Mullins (1965a). The neck growth has been related to the surface area reduction by Prochazka and Coble (1970):

$$\frac{\Delta S}{S_0} = \frac{-c}{4} \left( \frac{25Bt}{a^4} \right)^{1/3}, \quad (19)$$

where  $\Delta S$  and  $S_0$  are the changes in and the initial value of the surface area;  $c$  is the coordination number; and  $a$  is the radius of the spherical, mono-sized particles assumed in the models. However, nature is rarely so kind as to give spherical, mono-sized particles which can be packed with a constant coordination number. Wide distributions in particle sizes and shapes commonly characterize the typical powder. Powders with these characteristics often cannot be packed uniformly. Consequently, the poorly prescribed geometry, and rapid sintering of the fines usually preclude an independent determination of the surface diffusivity by this technique.

#### 7. The Growth of an Isolated Linear Facet

Thermal faceting is a mass transport process that is likely to evolve for any material with an anisotropic surface tension. Where thermal grooving and faceting develop concurrently, considerably more complicated geometries may be formed (as observed in this study). The only treatment of a faceting process, the growth of a linear facet by Mullins (1961), is therefore reviewed.

Mullins' model assumes two half thermal grooves separated by a facet plane as shown in Figure 5. For this geometry a fixed coordinate system is defined with its origin at the center of the facet plane. This requires that no mass be added to or subtracted from this plane; growth of the plane occurs by adding mass to the edge of the facet at P and by taking atoms away from the intersection of the facet and complex surface at Q.

The distance  $\chi^*$  is a measure of the scale of the facet;  $\alpha$  is the

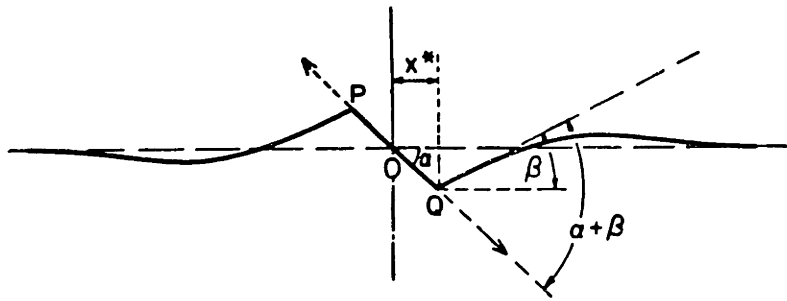


Figure 5 - The Linear Faceting Geometry [Mullins (1961)]

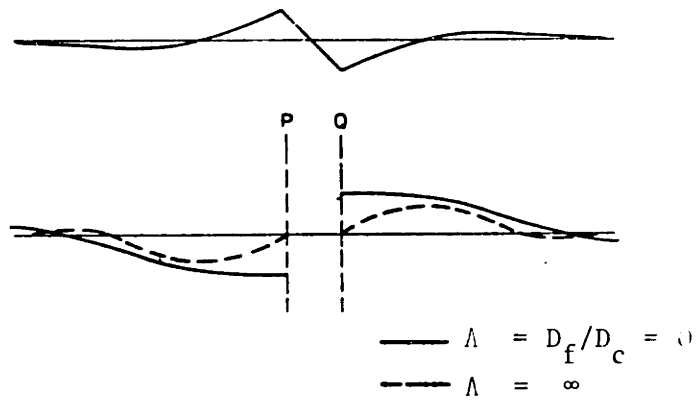


Figure 6 - The Linear Faceting Geometry and the Corresponding Chemical Potentials [Mullins (1961)]

angle between the facet plane and the sample surface. The angle  $\beta$  depends on the surface tensions of the facet and complex surfaces,  $\gamma_f$  and  $\gamma_s$  respectively, and the torque term associated with the facet plane,  $\partial\gamma_f/\partial\phi$

$$\gamma_c \cos(\alpha+\beta) = \gamma_f \quad (20)$$

$$\gamma_c \sin(\alpha+\beta) \leq \partial\gamma_f/\partial\phi \quad . \quad (21)$$

Growth of this facet proceeds on a time scale analogous to the thermal grooving process:

$$\chi^* = K^*(Bt)^{1/4} \quad . \quad (22)$$

The coefficient B is defined previously using the diffusivity on the unfaceted surface, which is assumed to be constant for all orientations. The values of  $K^*$  and the evolving profile shapes depend on the ratio  $m/n = \tan \beta/\tan \alpha$  and on the ratio of the surface diffusion coefficients on the facet and complex surfaces

$$\Lambda = \frac{D_f}{D_c} \quad ; \quad (23)$$

see Figures 6 and 7. This latter term has a significant influence on the direction of mass transport as depicted in the form of the chemical potentials plotted as a function of position along the surface for the limiting cases of  $\Lambda$ , see Figure 6. The values of  $\mu$  are fixed by the curvature of the complex surfaces immediately adjacent to P and Q by equation (1) and the curvature is controlled by  $D_s$ ;  $\mu$  is not defined along a faceted surface by this equation. Where there is no diffusion across the facet plane ( $\Lambda = 0$ ), mass flow across points P and Q must equal zero demanding that  $\partial\mu/\partial x = 0$  at these locations on the complex

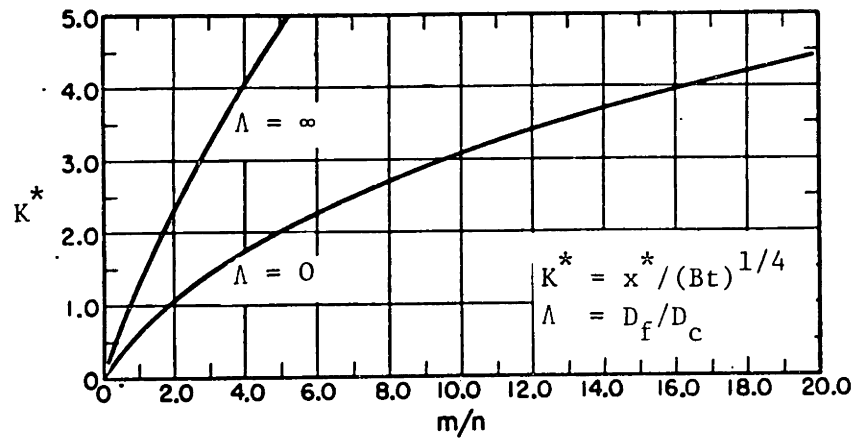


Figure 7 - The dependence on the Coefficient  $K^*$  on  $m/n$  ( $\tan\beta/\tan\alpha$ ) and on  $\Lambda$  [Mullins (1961)]

surface. Matter flows down the chemical potential gradients towards point P and away from point Q resulting in growth of the facet in both the positive and negative x-direction. The profile on either side of the facet has the character of a thermal groove profile formed by surface diffusion.

When  $D_f$  is finite ( $\Lambda > 0$ ), some mass flows from the region of positive curvature on the right of Q across the facet to the surface with negative curvature adjacent to point P. Consequently, the profile shape and the corresponding form of the chemical potential are changed. The rate of facet growth increases and the humps in the profile shapes contain considerably less mass than the amount removed from the region adjacent to the facet at Q. In the limit when diffusion on the facet is very rapid, the facet plane acts as a "short circuit" unable to support a chemical potential gradient, requiring  $\mu = \mu_0$  at P and Q. Most of the mass transported during the faceting process diffuses across the facet rather than along the complex surface. The rate of facet growth increases but only by a factor of 2 to 3, Figure 7; faster rates do not occur because diffusion across the facet becomes limited by the redistribution of matter by  $D_s$  on either side of the facet.

The solution to the linear faceting problem assumes that a negligible time is necessary for the characteristic shape to evolve, i.e., a zero incubation time. In practice, however, a range of incubation times is expected; no nucleation is required for a surface parallel to a facet plane. Consequently, scratches or the evolving grain boundary groove profile are regions where early facet nucleation is probable. Once nucleated,

facets grow according to the kinetics described by equation (22) until the facets interact. For a perfectly spaced and sized array of facets, the process ceases. Otherwise, the relatively slower process of Ostwald ripening (coarsening) ensues. No 3-dimensional treatment of faceting has been reported in the literature, although it is expected that similar growth and interaction steps occur.

### 8. Errors Associated with the Analysis of Thermal Grooving

Several conditions can influence the time dependent behavior of thermal grooving data plotted in log-log plots. Assuming an isotropic surface energy, the situations of interest are:

1. a transition from surface to lattice diffusion controlled thermal grooving,
2. as in #1, only with variable surface diffusivities,
3. the influence of an initial thermal groove width,
4. the influence of an error in the starting time, as would result from boundary migration.

Case 1 is depicted in Figure 8a. Here the expression for the groove width resulting from contributions of both surface and volume diffusion is

$$(\phi W) - \frac{1}{2}(\phi W)^2 + \frac{1}{3}(\phi W)^3 - \ln(1 + \phi W) = \frac{1}{4} \phi^4 4.6^4 Bt \quad , \quad (24)$$

where it is assumed that the profile is the same for either independent mechanism, and

$$\phi = \frac{c}{2.69B} \quad , \quad (25)$$

after Mullins and Shewmon (1959). Four orders of magnitude in time are



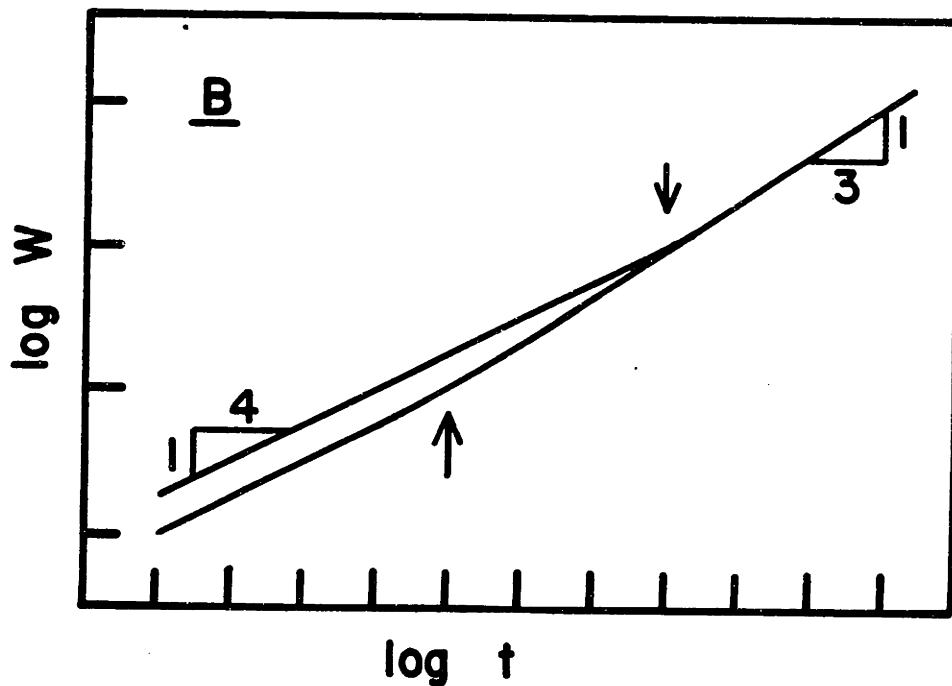
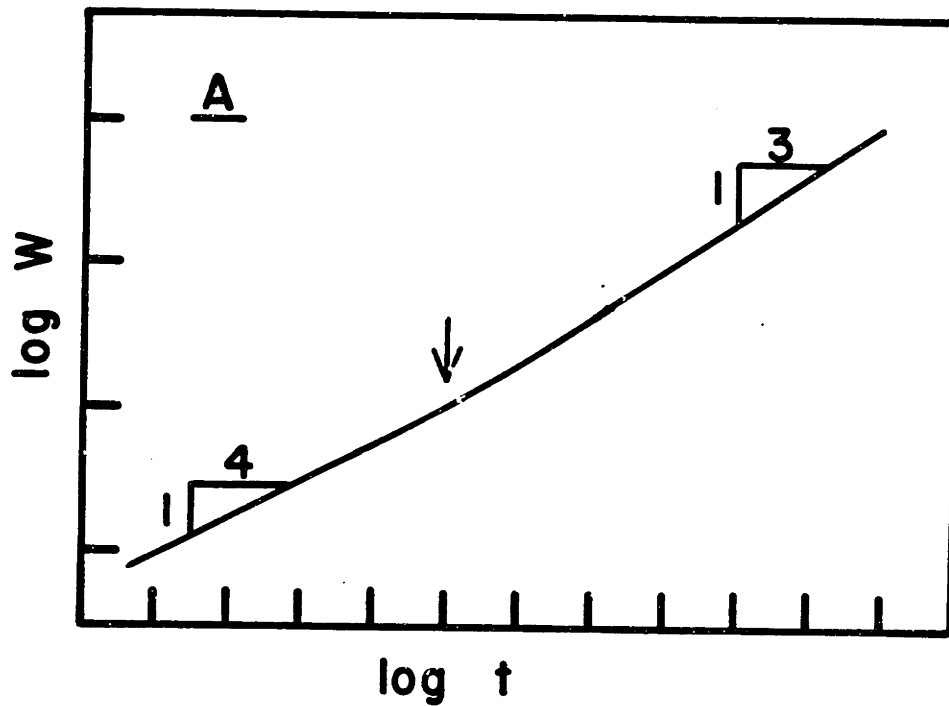


Figure 8(a) - Transition from surface to lattice diffusion controlled thermal grooving for log (width) versus log (time) plots. Four decades in time are necessary for complete transition.

Figure 8(b) Same as (a), only showing the effect of a 10X change in the surface diffusivity. Note the " $t_{\text{crossover}}$ " point is altered by 1000X for this change

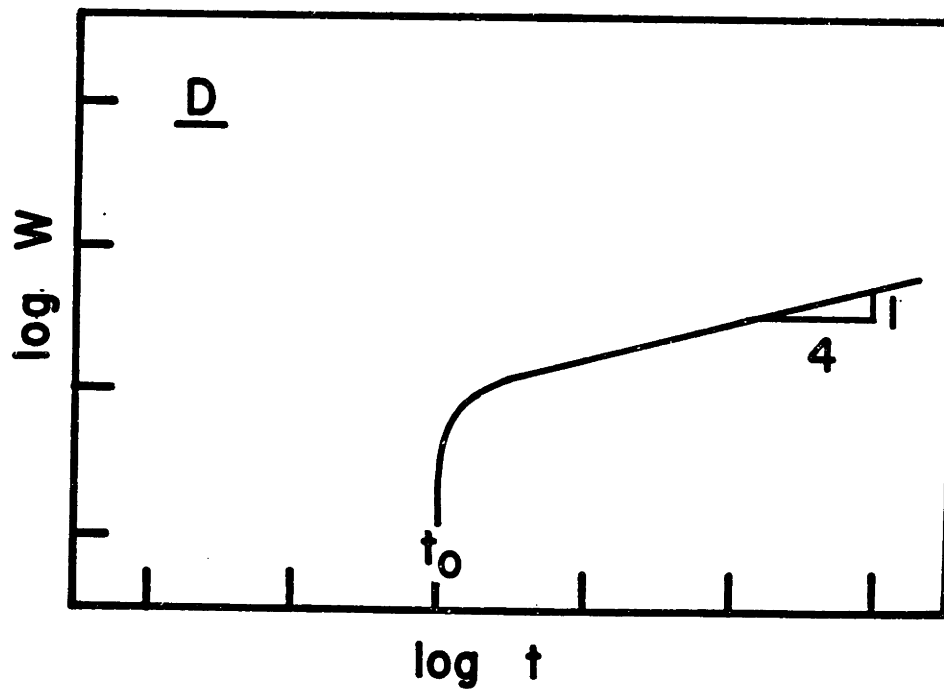
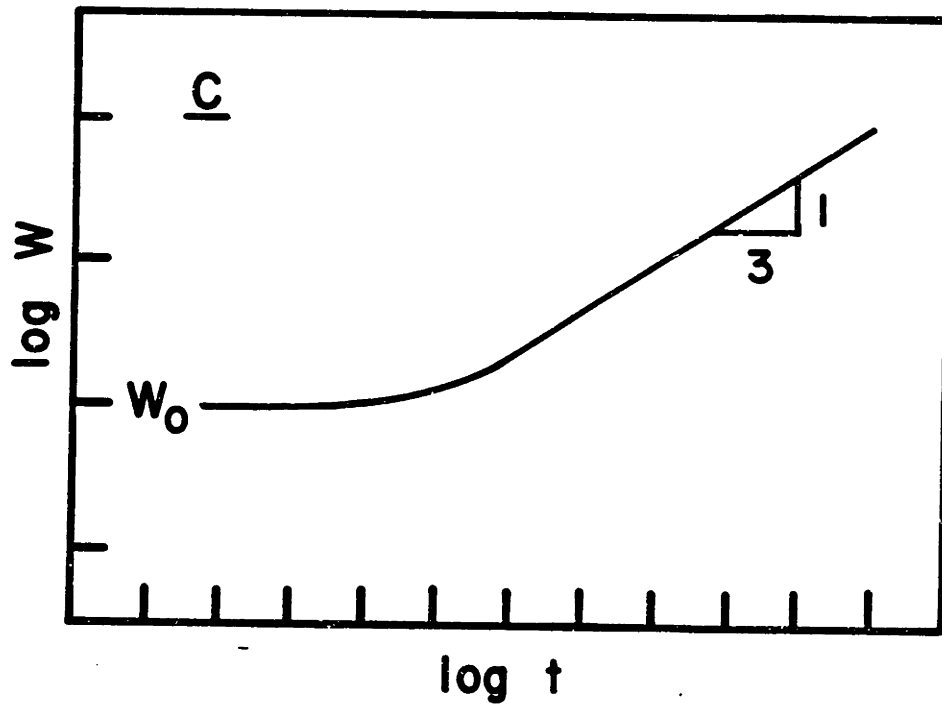


Figure 8(c) - Influence of an initial groove width ( $W_0$ ) on data plotted as  $\log(\text{width})$  versus  $\log(\text{time})$ ,  $W_0^n > k'(t-t_0)$

Figure 8(d) - Influence of an error in the starting time ( $t_0$ ),  
 $W_0^n < k't_0$

required for a complete transition from surface to lattice diffusion controlled kinetics, although most of the change in slope,  $d \log W / d \log t$ , occurs over two orders of magnitude. Obviously, groove width data over a broad time range is essential in order to see such a transition.

Case 2 is similar to case 1, only the effect of lowering the surface diffusion coefficient by a factor of 10x is shown, Figure 8b. This change lowers the thermal groove width values by  $10^{1/4}$  in the regime where surface diffusion is the dominant transport mechanism. More importantly, the point in time where surface and lattice diffusion have equal contributions to the thermal grooving process ( $t_{x\text{-over}}$ ) is decreased by three decades in time. Remembering that these transitions are gradual, as in Case 1, the need for thermal grooving data on many individual boundaries over a broad time span is obviously necessary if any variability in  $D_s$  is anticipated. If lattice diffusion is also variable by a factor of 10x, a band of curved lines, with  $1/4 < d \log W / d \log t < 1/3$ , representing the various combinations of surface and lattice diffusion to the thermal grooving process is expected for data on different boundaries.

Cases 3 and 4 consider the errors that result from measuring the slope on log-log plots owing to the presence of an initial thermal groove width or errors in the starting time, respectively. The generalized form of the equation that corrects for these according to Feingold and Li (1968) is:

$$W^n - W_0^n = k'(t - t_0) \quad . \quad (26)$$

The slope of a line defined by equation (26) when plotted as  $\log W$

versus  $\log t$  is:

$$\frac{d \log W}{d \log t} = \frac{1}{n} \frac{kt}{kt - kt_0 + W_0^n}, \quad (27)$$

where  $n$  is the characteristic exponent for surface or lattice diffusion, 4 and 3 respectively;  $W$  is the thermal groove width;  $W_0$  is the thermal groove width at time  $t_0$ ;  $k'$  is the kinetic constant; and  $t$  is the experimental time. In essence, all data are compared to the first datum point assuming constant temperature. For cases 3 and 4, the limiting conditions defined in Figures 8c and 8d are incorporated into equations (26) and (27). These can be used to illustrate the possible errors resulting from plotting  $\log W$  versus  $\log t$  when  $kt_0 \neq W_0^n$ ; here the initial thermal groove width is  $W_0$  and the altered starting time is  $t_0$ .

Case 3 demonstrates that the presence of an initial grain boundary groove may decrease the time dependence as judged from  $d \log W / d \log t$ , Figure 8c. For instance, an actual lattice diffusion controlled process may appear to be controlled by surface diffusion when a limited number of observations over a narrow time span are made, the frequent experimental procedure. With a sufficient number of accurate observations over a time span greater than  $10x$ , an upward curvature to the  $\log W$  versus  $\log t$  curve results. An important point with respect to this error is that  $W_0$  is insignificant unless it is greater than  $1/3$ - $1/2$  the first experimentally determined grain boundary groove width depending on whether  $n = 3$  or  $4$ .

Case 4 portrays a situation where the time dependence may be increased due to an error in the starting time. For instance, a grain

boundary may breakaway from its thermal groove and rapidly migrate to a new position. If the time expired during migration is negligible with respect to the thermal grooving process, a "normal" grooving process then begins at the instant the boundary stops migrating, time  $t_0$ . The effect of this is rapidly damped out in time, however, as shown in Figure 8d. At a time equal to  $3t_0$ , the error in the actual thermal groove width as compared to one that grew from time zero is less than 10%; at  $10t_0$ , the error is less than 3%.

If thermal grooving data exhibit features noted in cases 3 and 4, equation (26) may be used for correction;  $\log(W^n - W_0^n)$  is plotted against  $\log(t - t_0)$  where  $W_0$  and  $t_0$  are now the first datum point. For surface diffusion controlled thermal grooving, a straight line of slope = 1 results when  $n = 4$ . Note that  $d \log W / d \log t = 1/4$  would be found on a plot of  $\log W$  versus  $\log t$  only if  $W_0^4 = kt_0$  or if  $W_0^4 \ll kt$ , indicating surface diffusion. An analogous set of curves can be generated for lattice diffusion kinetics. For thermal grooving by contributions from both surface and lattice diffusion, a downward curvature with the slope  $< 1$  results for  $n = 4$ ; an upward curvature with the slope  $> 1$  characterizes a plot where  $n = 3$ . The point to be emphasized is that "good" data over a broad time span are essential.

McAllister and Cutler (1970, 1972a) have reported that the best method of data analysis is to use the intercept on plots of  $W$  against  $t^{1/n}$  as an indication of the diffusion process. The basic contention is that negative intercepts are unphysical instead of realizing that this feature could result from a change in mechanism, as pointed out by

Gjostein (1970); again, a limited number of available data points over a short time span was used as a motivation for this analysis. McAllister and Cutler further claim that positive intercepts are then an indication of the presence of more rapid growth of an initial grain boundary groove width; hence, equation (26) evolved as a method for correcting for an initial groove width. However, this correction carries the implicit assumption that the thermal groove profile at the first observation in time is that characteristic of a surface or lattice diffusion process. A remnant groove resulting from insufficient polishing or from an interval of chemical etching or vapor transport controlled thermal grooving is not appropriately treated by equation (26). The level of error depends on the magnitude of the altered starting profile relative to the profile being measured.

## B. Studies Reporting Surface Diffusion Coefficients

### 1. Thermal Grooving

The first reported value of a surface diffusion coefficient for alumina was deduced from the thermal grooving of a Morganite alumina materials by Robertson and Chang (1966). After washing with acetone, samples were annealed in air in a covered "high purity" alumina crucible at temperatures ( $\pm 20^\circ\text{C}$ ) within a broad range, 1100-1720°C. Three to nine time intervals within a span of one to two orders of magnitude were investigated at each temperature up to 1600°C; only one measurement was made at 1720°C. The average thermal groove width for each experiment was determined from the symmetric grooves on at least four interference micrographs. By the method of least squares, values of  $d \log W / d \log t$

were found to vary from 0.20-0.28; these results were used to conclude that surface diffusion is the dominant transport path. No systematic trend between  $d \log W / d \log t$  and temperature was found, although the data contain considerable scatter.

The observed thermal grooving rates for this material are larger than those found on other alumina materials, see below. Relatively high concentrations of Si and Ca are known to be present in this material\* which is consistent with the observation of second phases in the micrographs of Robertson and Chang (1966). As this material is relatively impure, the line 6 representing the surface diffusivities determined from the thermal grooving behavior is dashed in Figure 1. Interestingly, little faceting was observed in this study which may be associated with the impurity levels in these materials.

Shackelford and Scott (1968) measured the thermal groove widths as a function of time and the dihedral angle on fabricated bicrystals with symmetric  $[\bar{1}100]$  tilt-boundaries; the amount of tilt ( $4^\circ$ ,  $6^\circ$ , and  $61^\circ$ ), twist and rotation between grains was also documented but not correlated to the grooving process due to the large amount of scatter in the data. Experiments were conducted in vacuum ( $5 \times 10^{-6}$  torr) at only two temperatures,  $1540^\circ$  and  $1800^\circ\text{C}$ , with the samples contained in an inductively heated tungsten crucible. A variability of  $\sim 1.5x$  in the groove widths was recorded for all three samples at each of the three time intervals used; only a  $10x$  difference in time was investigated. By the method of least squares,  $d \log W / d \log t$  was found to vary between  $1/5$  and  $1/6$ .

---

\* For instance, based on the high creep rates of furnace tubes of this material and the contamination of samples fired in these tubes.

However, given the scatter in the data a line with  $d \log W / d \log t = 1/4$  adequately represented the data; the best line with a slope of  $1/4$  defines the  $\omega D_g$  values, line 3 plotted in Figure 1.

Unfortunately, several experimental details are omitted from this paper, including: the source or purity of the sapphire, the cleaning procedures, the temperature control, and whether a covered crucible or any alumina source was included near the sample during the annealings. No observations regarding surface faceting were mentioned although faceted pores did develop along grain boundaries during bicrystal fabrication. Additionally, the groove profile shown is slightly asymmetric.

Robertson and Ekstrom (1969) conducted a comparative study on the thermal grooving of three alumina materials and documented impurity levels by "spectroscopic analysis". The three materials were: Morganite  $\Delta RR$  <sup>®</sup>, Lucalox <sup>®</sup>, and Linde <sup>®</sup> sapphire containing a few lineage boundaries. For sapphire, the angle between the c-axis and the normal to the sample surface is approximately  $55^\circ$ , probably the  $(11\bar{2}3)$  plane. All experimental procedures are the same as those listed by Robertson and Chang, only with  $\pm 2^\circ\text{C}$  temperature control.

The Lucalox and Linde samples were found to have consistently slower rates of thermal grooving than the Morganite material; the data for the Morganite samples were those reported by Robertson and Chang plus four new data points at  $1500^\circ\text{C}$ . Lines 4 and 5 represent the results for the Linde and Lucalox samples, respectively. The similar grooving rates noted on the Lucalox and Linde specimens were regarded as very interesting in light of the fact that the impurity levels were



similar for the Lucalox and Morganite samples. A higher concentration of Mg and a lower concentration of Ca in the Lucalox samples were the only significant differences between the two materials; other impurities, K, Na, etc., were detected at nearly identical concentration. However, these data do not indicate the concentrations on the surfaces. Some boundaries in the Morganite material had significantly smaller groove widths than the average. A considerable number of asymmetric groove profiles and a few boundaries with narrow groove widths were also found on Lucalox specimens. Some of these latter boundaries were associated with migration but many appeared to be stationary. It was not stated whether these smaller widths are included in the averages. No comments on the profiles for the Linde material or with regard to faceting on any of the samples were included.

In an attempt to sort out the effects of surface contaminants, the following powders were sprinkled onto the surface of the Linde material:  $\text{SiO}_2$ ,  $\text{Na}_2\text{O}$ , 70%  $\text{SiO}_2$ -30%  $\text{Na}_2\text{O}$ , and 60%  $\text{SiO}_2$ -40%  $\text{CaO}$ . All additions formed second phase particles on the surface at  $1500^\circ\text{C}$ . Little effect on the grooving rate occurred for the  $\text{Na}_2\text{O}$  and/or  $\text{SiO}_2$  additions. For the  $\text{SiO}_2$ - $\text{CaO}$  additions, wide grooves were found in areas where liquid phase had formed. In other areas, the additions had no measurable effect or a slight enhancement of the grooving rate. No correlation between the local impurity concentration on the surface and the grooving rate could be ascertained. However, these results indicate the  $\text{CaO}$ - $\text{SiO}_2$  additions to the surface may increase the surface diffusion coefficient.

Achutaramayya (1972) has measured the thermal groove widths on the  $(10\bar{1}0)$  surface for boundaries associated with both the growth twins in

Linde sapphire and the deformation twins introduced in Verneuil grown crystals during bicrystal fabrication by his thesis advisor, W. D. Scott.\* Samples were washed with soap and water followed by several rinses with hot water, then isopropyl alcohol. Anneals were carried out in sapphire crucibles with tightly fitted lids in a vacuum induction furnace using a tungsten susceptor at pressures of  $2 \times 10^{-5}$  torr and temperatures ( $\pm 5^\circ\text{C}$ ) ranging from 1500–2000°C. Four time intervals were investigated within a period less than a decade of total experimental time for all but one temperature; at 1800°C, nine time intervals were examined over one and a half decades in time. The thermal groove widths have an "uncertainty of  $1/2\mu\text{m}$ ", as determined by interferometry. Data from the samples with growth twins were averaged to designate one set of points while the average from the sample with deformation twins defined a second set of points. Some scatter in the averaged data was present but it was adequately fit by a single, straight line. Values of  $d \log W / d \log t$ , determined by the least squares method, range from 0.210 to 0.296; no systematic trend with temperature was noted. The groove profiles shown are usually asymmetric, though little if any faceting appears to be present. The  $(10\bar{1}0)$  plane is noted to be one where thermal faceting is minimal; however, no reference to the source of this information is given. The results\*\* of this study are represented by line 14, Figure 1.

McAllister and Cutler (1972b) studied the thermal groove develop-

---

\* Hence, these may be the same samples investigated by Shackelford and Scott (1968).

\*\* The pre-exponential factor in equation (28) of Achutaramayya is a factor of 1.72x too large.

ment as a function of time for pure alumina and samples doped with varying amounts of Fe and Mn. Lucalox and Ti doped samples were also used in experiments where the samples were annealed only once. The sources of material included samples from the thesis work of others, a commercial product, pure samples made from unknown starting materials, and unspecified small grain size samples that were fused with a carbon-arc torch on a pure graphite pedestal. All samples were washed with acetone except for the Lucalox samples which were boiled in aqua regia for one hour; this acid mixture dissolves the  $\text{MgAl}_2\text{O}_4$  spinel included in these samples. Polished faces of the samples were placed against one another and the samples were buried in powder of a similar composition in a covered, "high-purity" alumina crucible. Samples were annealed in alumina furnace tubes with an  $\text{H}_2$ -protected Mo-winding. Although unreported, the annealing atmosphere is assumed to be air, except where experiments involved the changing of oxidation states. Groove widths were primarily determined by interferometry and Nomarski interference contrast on plastic replicas which facilitated retracing only the "ideal" thermal grooves. Four time intervals were investigated over a period of approximately 1-1/2 decades in time at temperatures of 1400, 1500 and 1600°C.

The data for pure samples, reported as  $W$  versus  $t^{1/3}$ , are not quantitatively represented by straight lines due to scatter. It is not stated whether these data are averages for several boundaries or for

one specific boundary.\* In all cases a positive intercept on the W-axis resulted; however, replotting the data as W versus  $t^{1/4}$  results in an intercept that is much closer to zero and sometimes slightly negative. In spite of these trends, McAllister and Cutler assert that the data fit only lattice diffusion kinetics. Interpreting the grooving rates in terms of lattice diffusion kinetics results in implied diffusivities that are approximately 10-20x larger than those deduced from creep data on pure alumina (by Hollenberg and Gordon (1973) and Lessing and Gordon (1977)). Re-interpreting these results in terms of surface diffusion gives diffusivities that are best represented by line 7 in Figure 1.

The thermal grooving data from doped samples presents some interesting and inconsistent trends. At 1400°C, the grooving rates were negligibly different for the pure samples and those doped with up to 10<sup>W</sup>/o Fe<sub>2</sub>O<sub>3</sub>. This result suggests that iron-doping has no significant effect on the surface diffusivity, and that the lattice diffusion coefficient is not enhanced to a level sufficient for it to contribute. At higher temperatures, grooving rates were enhanced indicating that either the surface and/or lattice diffusivity are enhanced by Fe-additions. The calculated lattice diffusivities are in fair agreement with those deduced from creep data for similarly doped samples (after Gordon and co-workers).

---

\* Furthermore, most of the grooving data for pure samples at 1500°C, Figure 3(B) of McAllister and Cutler, are reported to be from one of Robertson's papers; but, no data corresponding to those plotted could be found in Robertson's papers! It is therefore difficult to judge the merit of McAllister and Cutler's contentions since many rely on comparisons to this data.

For Mn-doped samples at 1500°C, the grooving rate increased with the dopant level and the slopes of the lines characterizing the data increase with time on the  $W$  versus  $t^{1/3}$  plots. This latter behavior does not indicate a surface to lattice diffusion transition in kinetics; however, it could be caused by the presence of an initial groove width,  $W_0$ , or could be due to equilibration of the doped samples during annealing. No equilibration anneals were mentioned in the paper. In additional experiments, samples doped with varying Mn-concentrations were buried in powder doped with a higher Mn-level than any of the samples. The grooving rate was unchanged as compared to the samples buried in powder of the same composition.

The effects of changing  $P_{O_2}$  for Ti and Fe-doped samples were also investigated at 1500°C. The grooving rate decreased for the Ti-doped specimens upon going from an oxygen to a tank hydrogen atmosphere; this trend is consistent with the behavior in creep samples where the kinetics are controlled by lattice diffusion (Gordon and co-workers). The grooving rates decreased on the Fe-doped samples in going from oxidizing to reducing conditions, opposite to the effect found on creep rates (Gordon and co-workers). This ambiguity was blamed on the precipitation of Fe-rich phases as the  $P_{O_2}$  was lowered.

In summary, the implied surface diffusivities from McAllister and Cutler's grooving results on undoped samples are in good agreement with those determined in other studies. Iron-doping at higher temperatures, Ti-doping for high  $P_{O_2}$ , and Mn-doping seem to enhance the lattice diffusion contribution to thermal grooving, as based on similar trends ob-

served in steady state creep behavior; steady state creep has no contributions from surface diffusion. Limited evidence (Fe-doping at 1400°C, and experiments adding extra Mn suggests that the surface diffusivity is relatively insensitive to changes in the dopant concentration at these relatively high levels of doping.

Henrichsen (1973) studied the thermal grooving of low angle boundaries on Linde sapphire plaques which were determined to be within 3° of the (11 $\bar{2}$ 3) plane using the Laue back reflection method; these are the standard Linde sapphire wafers specified as having the angle between the surface normal and the c-axis equal to 60°. Specimens were rinsed with acetone, ethanol, and distilled water prior to annealing in an open Morganite  $\Delta RR^{\text{R}}$  crucible in a vacuum of  $10^{-6}$  torr. The furnace used a tungsten heater and tantalum heat shields. Four to seven measurements over one and a half decades in time were made at temperatures of 1600, 1700, and 1800°C. A marked difference in the grooving rate was found between top and bottom faces of the samples. Symmetric thermal grooves were found on the top side while much larger, "irregular" groove widths and surface deposits characterized the bottom face. Only the top side groove widths were recorded, although the number of grooves or measurements is not stated. The deposits were later reported to contain Ca, Si and Ta by Huang, Henrichsen and Li (1975); the degree to which the grooving rate was enhanced, however, was not documented. As  $0.22 \leq d \log W / d \log t \leq 0.25$ , it was concluded that surface diffusion controlled thermal grooving. No estimate of the uncertainty or variability in the width measurements is given. The

surface diffusion coefficients calculated from the grooving behavior, line 10, Figure 1, were approximately 3x larger than those deduced from the multiple scratch smoothing technique; this difference was thought to be at least partially due to an "impurity atmosphere" caused by the Morganite crucible. No mention of faceting was made.

## 2. Multiple Scratch Smoothing

Huang, Henrichsen and Li (1975) measured the decay of "nearly sinusoidal" gratings as a function of the profile wavelength, 7 to 12.7 $\mu$ m, for the (0001) and (11 $\bar{2}$ 0) planes of Linde sapphire at temperatures ranging from 1500 to 1750°C; the (11 $\bar{2}$ 3) plane was only annealed at 1600°C. Four sets of profiles were etched into each plague, each in the sequence rotated by 45°. Profile etching was accomplished by either ion-milling or by chemical means. Diffusion coefficients were reported only for data taken on ion-milled profiles. In his thesis, Henrichsen (1973) reports similar data from gratings that were chemically etched using molten KOH. These specimens were then subjected to a K<sub>3</sub>Fe(CH<sub>3</sub>)<sub>6</sub>-KOH bath to remove the Cr-mask used in the profile production, soaked in aqua regia for 4-5 hours, followed by a series of rinses in trichloroethylene, acetone and finally, ethyl alcohol. Samples were contained in a crucible with a lid, both fabricated from Linde sapphire. Annealings were done in an ion-pumped vacuum chamber using a tungsten heater and tantalum heat shields at a pressure of  $\sim 10^{-6}$  torr.

A number of interesting and other beguiling features resulted from this study. Faceting or profile distortion due to surface anisotropy was commonly a problem depending on the orientation of the grating on

the surface. It was reported that these problems were minimized by orienting the grating in a direction parallel to a line connecting the pole of the surface with the pole of the nearest low index plane. Using this criterion, it was concluded that a cusp in the surface energy/orientation plot exists for the (0001) plane. However, the interference micrographs and corresponding pole plots do not clearly support this contention. It appears as though another plane has low surface energy. Further information with respect to faceting cannot be extracted from these interferographs on the four grating orientations unless a crystallographic direction along the surface is known. Faceting was not reported for the other two surface orientations, although asymmetric profiles did evolve on the  $(11\bar{2}0)$  plane for all four grating directions; the  $(11\bar{2}3)$  plane was shown to develop rather perfect sinusoidal profiles presumably indicating less anisotropy on this surface.

A large variability in the decay rate,  $S$ , was noted for each wavelength grating in both reports. In Huang et al., positive decay rates are shown for all wavelength gratings that were etched by ion-milling. Most of the data, regardless of the etching technique, are characterized by markedly sharp decreases in the decay rate with increasing wavelength; the longer wavelength profiles reported in Henrichsen's thesis, often grew in amplitude over the entire 250 hours of annealing at  $1600^{\circ}\text{C}$ . The shorter wavelength gratings were found to grow initially then decay. No record of annealings prior to the data acquisition nor micrographs showing the profile morphology at the various states of decay were included in Henrichsen's thesis. Consequently, it is not known whether



the amplitude growth of the profile is related to the initial smoothing of the rough, "as-etched" gratings. No acknowledgement of these problems nor further experimental detail are given in Huang et al.

The straight lines representing the data plotted as  $S/\omega^3$  against  $\omega$  often have negative intercepts inferring that  $C < 0$ , and therefore  $D_L < 0$ . Since this is physically unrealistic, positive  $c$ -values were assigned using a  $D_L$  based on the observed thermal grooving rates. This  $D_L$  is less than the Al-lattice diffusivity in  $Al_2O_3$ , after Paladino and Kingery (1962).\*

These data are interesting in spite of the uncertainties and experimental problems. The best estimates of the surface diffusivities on the (0001)\*\* and (11 $\bar{2}$ 0) planes represent a lower bound of all the values plotted in Figure 1, lines 8 and 9, respectively. However, the profiles from which these implied diffusivities were deduced are either faceted or asymmetric; the quantitative influence on the smoothing rates caused by these geometric changes is not known. Interestingly, an even lower surface diffusivity, by  $\sim 3x$ , is implied by the smoothing data from the (11 $\bar{2}$ 3) plane on which the grating developed a markedly sinusoidal profile. Although the results are limited, some anisotropy in the product of the surface energy-surface diffusivity is suggested.

Kitazawa et al. (1979) studied the decay of periodic gratings for wavelengths of 6.3 to 17.4 $\mu$ m on the (110 $\bar{2}$ ) plane of Linde sapphire at temperatures ranging from 1530°C to 1770°C. These experiments were

\* Assuming the transport were entirely due to surface diffusion, i.e.  $C = 0$ , would only increase the reported surface diffusivities by less than 20%.

\*\* The pre-exponential of the equation summarizing the diffusivity on the (0001) plane is 10x too large in Huang et al.

conducted in air in an alumina tube furnace with an  $H_2$  protected Mo-winding. In general, little experimental detail is given; it was not stated whether samples were contained in a crucible or exposed to the furnace atmosphere. Gratings were etched by RF sputtering with Ar/1%  $O_2$  or by a  $H_3PO_4-H_2SO_4$  solution; no difference in results was found. The profiles developed with an asymmetric character but decayed exponentially with time; considerable variability in the decay rate was present. However, the average decay rate was found to depend on the inverse wavelength to approximately the fourth power indicating that surface diffusion was the primary mode of mass transport. This surface diffusivity, line 7, Figure 1, is approximately 8x larger than that deduced from the results of Huang et al. for the (0001) and  $(11\bar{2}0)$  planes. However, it is not known whether to attribute this enhancement to anisotropy in the  $\gamma\omega D_s$  product, to the air rather than vacuum environment, or to contamination which could result if the gratings were not adequately shielded from exposure to the general furnace atmosphere. Kitazawa et al. also reported that preliminary experiments on the (0001) plane were hampered by strong anisotropy effects, and therefore efforts on specimens with this orientation were abandoned.

Recently, Monty and Duigou (1981) have reported results on the decay of  $10\mu m$  wavelength gratings parallel to the  $[01\bar{1}0]$  direction on the (0001) plane of pure and 1000 ppm MgO-doped sapphire in air. A factor of  $\sim 6x$  smaller decay rate, and therefore implied surface diffusivity, was reported for the MgO-doped sample annealed at  $1650^\circ C$ . At  $1700^\circ C$ , the pure and doped specimens decayed at the same rate. Surface

diffusivities calculated from these rates, Figure 1, are open to question since substantial faceting and asymmetry of the grating profile developed simultaneously. For the pure specimen at 1650°C, the profile resembles a square wave while the doped sample was characterized by a small amount of distortion and the evolution of pits on the surface. The profiles on both the pure and doped material evolved into facets with a sawtooth character. The decay rates on the pure samples are approximately 20 to 60x larger than those observed in a vacuum environment by Huang et al. A further enhancement of 2x was found using an Ar atmosphere. Monty and Duigou report that these larger decay rates in air and argon are indicative of enhanced vapor transport in a dense atmosphere. This reasoning is incorrect and in no way supported by thermochemical data.

### 3. Single Scratch Smoothing

Achutaramayya (1972) has also investigated scratch smoothing on the (1010) plane of sapphire. After scratching the surface parallel to the twin boundary grooves, specimens were annealed at 1800°C to smooth out the irregular profile. Samples were then heat treated at only one annealing temperature, 1600°C, under conditions discussed previously. The hump spacing,  $W$ , was measured at four time intervals within a 24 hour period. The profile shapes that developed are quite asymmetric although apparently not faceted. From the analysis of the data, the interpreted  $t_0$  value was claimed to be consistent with a surface diffusion mechanism and the implied  $\omega D_g$  values were noted to be in good agreement with those deduced from thermal grooving. However, a compa-

rison of all combinations of pairs of data points yields widely varying values of  $t_0$ . Consequently, it is concluded that the data do not confirm either surface or lattice diffusion kinetics.

Maruyama and Komatsu (1975) studied scratch smoothing on the (0001) plane of Nakazumi sapphire at temperatures from 1430 to 1700°C. The samples were wrapped in platinum foil and air annealed in a Mo-resistance furnace. The samples were cleaned after the heat treatments; the reasons for this procedure were not explained. Neither surface or lattice diffusion control of the kinetics can be justified since only calculated surface diffusivities were presented. A micrograph included in this paper shows the profiles to be faceted and asymmetric; therefore, these results are judged to be unreliable, and the line representing the data is dashed in Figure 1, line 13.

#### 4. Cylindrical Void Instability

Yen and Coble (1972) studied the spheroidization of tubular voids in sapphire annealed over the temperature range of 1650 to 1810°C ( $\pm 10^\circ\text{C}$ ). In these experiments, parallel cylindrical voids originated during the "healing" of cracks (initiated in polished sapphire discs using a WC-scribe); the healing period was a 10 hour anneal at the experimental temperature. Prior to the introduction of the cracks, care was taken to first wash the samples with soap, water, and a series of organic solvents. A series of annealings in air was performed in an alumina tube furnace with the specimens held in polycrystalline alumina boats. Two sources of sapphire were used, Lexington Laboratory CVD and Linde Verneuil sapphire. Both materials gave equivalent results.

The changes in morphology of selected pores were recorded at the end of each time interval. By noting the progress of individual ovulation events,  $\tau$  was estimated. For the specific pores, the relationship of the void spacings to the initial cylindrical pore radius and to the resulting spherical pore radius were also determined,  $\lambda = (9.075 \pm 0.446)r_0 = (4.74 \pm 0.784)r_1$ . These  $\lambda$ - $r$  relationships were interpreted as an indication of a surface diffusion controlled process. Line 11, Figure 1, represents these results.

In addition to the voids that broke up in a manner prescribed by Nichols and Mullins, several unexplained complex shape changes were noted. These pore morphologies were thought to be a manifestation of impurity effects, as was surface etching. One of the complicated pore shapes was a "dumbbell with a long connecting stringer which did not pinch off." In at least one instance, a dumbbell-shaped void spheroidized into a single pore, as depicted in Figure 3 of Yen and Coble. The simultaneous formation of several spherical voids also occurred, as in the break up of an infinite cylinder; this is not surprising considering that longitudinal undulations are probable when the two "rough" fracture surfaces are joined. In a related area, it is not known whether a grain boundary has been formed. The presence of a grain boundary would be consistent with the larger coefficient in the observed  $\lambda$ - $r$  relationship. The possible contributions by volume diffusion are estimated to be negligible based on the Al-lattice diffusivity measured by Palodino and Kingery (1962). Judging from the persistence and stability of the "spheroidized" voids on further annealing, no

measurable amount of either shrinkage or coarsening occurred.

Gupta (1978) has also studied the instability of cylindrical voids, only in a polycrystalline alumina material, Lucalox. The cracks were formed by thermal shock from dropping hot samples into cold water. These specimens were then annealed in the range of 1500 to 1700°C for varying lengths of time in a vacuum of approximately 5 torr. The type of furnace was not mentioned.

The evolution of individual voids could not be followed in these experiments because the samples are not transparent. However, the fracture surfaces of these specimens depict a number of approximately tubular voids. Some of these cylindrical pores had broken up into rows of approximately equisized, equispaced "spherical" voids, while the spacings and sizes of other voids varied considerably. Many of the voids were faceted, but treated as spherical in the analysis. Hence, the uniformly spaced and sized sets of pores were analyzed in the following manner. The number of voids ( $N_v$ ) is related to the number of ovulations ( $N_{ov}$ ) by  $N_v = N_{ov} + 1$ , for the break up of a cylinder by ovulation. Based on the predicted recession of the cylinder length for each ovulation event,  $N_{ov} = (1/3.35)L/D$ , where  $L/D$  is the length/diameter ratio for the cylinder and  $D$  is related to the spherical pore radius,  $r_1$ ,  $D = r_1/0.92$ . Using these relationships, the actual number of pores ( $N_A$ ) was determined to be 0.5 to 0.6  $N_v$ . It was concluded from these results that both ovulation and "spheroidization", as in that noted by Nichols (1976) for  $L/D < 7.2$ , develop simultaneously, with ovulation being the dominant process. It is not clear, however,

how or if this "spheroidization" process occurs for cylinders where  $L/D > 7.2$ . The published photomicrographs show that some of the long cylinders have roughly periodic undulations along their length. This presumably indicates that the cylinder is breaking up by an instability analogous to that of an infinite cylinder, as well as by ovulation at the ends. However, the occurrence of both modes of break up does not explain why  $N_A < N_V$  because the  $\lambda-r_0$  relationships are probably not significantly different.

The data were also plotted as the void spacing against the apparent spherical void diameter. These results are characterized by a considerable amount of scatter although the agreement with a surface diffusion controlled process is better than for lattice diffusion. This agreement seems to be inconsistent with the fact that  $N_A < N_V$ . The inconsistency is presumably related to the assumption that perfect spheres and cylinders are present rather than the polyhedra or other complex shapes shown in the photomicrographs. Furthermore, the presence of a grain boundary is likely, given the material is polycrystalline and often characterized by intergranular fracture. Consequently, pore coarsening and sintering are probably occurring and complex geometries are expected even if faceting is not. Finally, the reported void spacings and diameters may be less than their actual values since data were extracted from SEM micrographs; distances may appear to be shortened using SEM micrographs due to the specimen tilt. (see Experimental Procedures).

The agreement in the comparison of the pore sizes and spacings was

thought to be an adequate indication of a surface diffusion controlled process. Consequently,  $\omega D_s$  values, line 12 of Figure 1, were estimated using equation (18) assuming that the ovulation time was approximately experimental time for the rows of pores and for isolated "unduloids" about to pinch off. Here it is not stated explicitly that the experimental time is divided by the apparent number of ovulation events; however, it is assumed that this method was used. Either way the ovulation time is overestimated, so the implied  $\omega D_s$  values are low. In the case of the "unduloids", the  $\omega D_s$  values are also reported to be less than the actual values because the estimated spherical pore radius is probably too small. Unfortunately, a more quantitative treatment of these complexities in geometry and detailed corrections for experimental problems are not available. Therefore, it is difficult to assess the level of error in these results as reported, but most of the systematic error would cause the estimated  $\omega D_s$  values to be low.

### 5. Sintering

Prochazka and Coble (1970) deduced the amount of surface area reduction in powder compacts by measuring the changes in gas permeability resulting from air annealings for various lengths of time in the temperature range 750 to 900°C. No shrinkage was observed. Two different alum-derived powders from Union Carbide Corporation were studied; the Linde A powder is a mixture of  $\gamma$  and  $\alpha$ -alumina where the  $\gamma$ -phase is a fine, high surface area, metastable phase and the  $\alpha$ -phase is characterized by particle sizes in the 0.1 to 0.3 $\mu$ m range and "wormlike" agglomerates composed of a few to many particles; the Linde C powder is 100%



$\alpha$ -alumina where the  $\alpha$ -characteristics are similar to that in Linde A, but the particle sizes are coarser, 0.5-1.0 $\mu$ m. These powders were ball-milled in order to break down the agglomerate structure as much as possible, and die-pressed to a relative density of 0.5 to 0.6.

The implied surface area reduction kinetics for the two powders were significantly different as depicted by the  $\sim 50\times$  difference in the  $\omega D_s$  values deduced from these measurements, lines 1 and 2 in Figure 1. Most of this variance probably arises from complex packing and geometric constraints which are not accounted for in the simple models that relate the geometry to the gas permeability of the powder compact. As a consequence of these uncertainties, neither the magnitude nor the activation energies of the implied  $\omega D_s$  values can be regarded as being reliable. Therefore, lines 1 and 2 are dashed in Figure 1.

Rao and Cutler (1972) measured the amount of neck growth between particles, 4 to 10 $\mu$ m in diameter, after sintering for 50 hours at 1200°C in air. The approximately spherical and probably polycrystalline powder was formed by passing Alcoa A-14 alumina powder through an oxygen-acetylene flame. The relative neck sizes shown in the photomicrographs fall into two size ranges: one range is approximately 0.1, and the other about 0.3. The larger necks were reportedly formed during the spheroidization process, although no micrographs showing the initial powder were included. No shrinkage measurements were made so some contribution to the neck growth by boundary diffusion is anticipated. If boundary diffusion were contributing to neck growth, larger implied surface diffusivities should result by neglecting it. By assigning

all the growth for the smaller necks to surface diffusion, a range of  $\omega D_s$  values was calculated, as shown in Figure 1. Very small values of  $\omega D_s$  relative to those of Prochazka and Coble are implied. The implied  $\omega D_s$  value would be increased by 1000x if growth of the larger neck from zero time were considered. These considerations illustrate the level of error that many accompany the "determination" of diffusivities from sintering data.

Komatsu et al. (1977) have measured the surface area reduction kinetics of a noncompacted, 99.99%,  $\alpha$ -alumina powder in air over the temperature range 1035 to 1250°C. The powder was fabricated by calcining a Shinkosha  $\gamma$ -alumina powder and then classified into a narrow size distribution, 0.2 to 0.4 $\mu$ m, with an average particle size of 0.28 $\mu$ m; the equivalent spherical diameter as indicated by the initial surface area was 0.24 $\mu$ m. Shrinkage kinetics of compacts formed from this powder were later measured by Moriyoshi and Komatsu (1978) for temperatures from 1180 to 1260°C. Hence, a shrinkage mechanism, probably boundary diffusion, is also contributing to the surface area reduction; although no confirming microstructural evidence was offered. The reduction in surface area is greater than the amount that would necessarily accompany shrinkage. The results of this work represent the only known surface area reduction study on a narrow size distribution powder of  $\alpha$ -alumina. Consequently, these data have been reanalyzed and the behavior found to be in accordance with that predicted by equation (19).\*

---

\* Except for a factor of 8, the initial stage surface area reduction due to boundary diffusion would have the same kinetics as equation (19). The implied values of  $\omega D_s$  result from (incorrectly) assuming all neck growth was due to surface diffusion.

$\omega D_s$ -values are reported as a range which encompasses the uncertainties with respect to size and coordination number, see Figure 1.

Other studies on sintering kinetics have been used to estimate values for the surface diffusion coefficient: Moriyoshi and Komatsu (1973,1976,1978) and Moon et al. (1977). These references are included here only for the sake of completeness. A detailed review of these studies is omitted because a) shrinkage kinetics were interpreted in terms of surface diffusion only, or surface and volume diffusion (neglecting boundary diffusion), and/or b) broad size distribution powders were used in experiments. To justify serious consideration of such studies, both surface area reduction and shrinkage must be measured on monosized powder.

## 6. Summary of the Literature Review

In general, the results of the studies reporting surface diffusion coefficients indicate a) that there are no reliable surface diffusion coefficients below a temperature of 1500°C, and b) above 1500°C, different techniques and materials result in a broad range of implied surface diffusion coefficients.

There is no clear trend in reviewing these studies indicating that one technique yields consistently high or low surface diffusivities, see Table I. Such a trend is unlikely because all methods are not ideal and due to the wide range of experimental techniques, materials and variables. Consequently, these studies should be divided into two categories. For those in which the geometry is sufficiently well prescribed and the analyses accurate, the measurements can be

Table I. Literature Data Ranked by Decreasing Magnitude of  $\omega_D$ s for Temperatures of 1500 to 1800°C.

Line	Source	Material	Crucible/ Sample Holder	Furnace	Atmosphere	Technique
13	Maruyama & Komatsu	Sapphire	crucible-? (Pt-foil wrapping)	Al <sub>2</sub> O <sub>3</sub>	Air	SSS
11	Yen & Coble	Sapphire	Al <sub>2</sub> O <sub>3</sub> -boat, open	Al <sub>2</sub> O <sub>3</sub>	Air	VI
6	Robertson & Chang	Morganite	Morganite, closed	Al <sub>2</sub> O <sub>3</sub>	Air	GBG
	Monty & Duigou	Sapphire	?	Al <sub>2</sub> O <sub>3</sub>	Air/Air	MSS
7	Kitazawa et al	Sapphire	?	Al <sub>2</sub> O <sub>3</sub>	Air	MSS
5	Robertson & Ekstrom	Lucalox	Morganite, closed	Al <sub>2</sub> O <sub>3</sub>	Air	GBG
4	Robertson & Ekstrom	Sapphire	Morganite, closed	Al <sub>2</sub> O <sub>3</sub>	Air	GBG
14	Achutaramayya & Scott	Sapphire	Sapphire, closed	Cold Wall	vacuum (2x10 <sup>-5</sup> torr)	GBG
10	Huang et al.	Sapphire	Morganite, open	Cold Wall	vacuum ( ~ 10 <sup>-6</sup> torr)	GBG
3	Shackelford & Scott	Sapphire	Tungsten, o/c?	Cold Wall	vacuum ( < 10 <sup>-5</sup> torr)	GBG
12	Gupta	Lucalox	?	?	vacuum ( ~ 5 torr)	VI
8 & 9	Huang et al.	Sapphire	Sapphire, closed	Cold Wall	vacuum ( ~ 10 <sup>-6</sup> torr)	MSS
(1123)	Huang et al.	Sapphire	Sapphire, closed	Cold Wall	vacuum ( ~ 10 <sup>-6</sup> torr)	MSS

regarded as determinations of the surface diffusion coefficients. Only grain boundary grooving and multiple scratch smoothing seem to fit in this category, even there anisotropy causes significant errors. The problems with most of the other techniques are so complex that the calculations of surface diffusivity serves as a check on the quality of the simple modeling of a complex problem; these results should not be regarded as independent measurements of  $\omega D_s$ . The results from sintering experiments are included here in this spirit and because of the interest in determining the importance of surface diffusion in sintering.

The results of these studies on surface diffusion present an approximate trend with respect to sample purity and experimental cleanliness if the following set of presumptions is made:

- 1) An open crucible in a vacuum system allows impurity evaporation and therefore results in cleaner experiments; a closed crucible has less impurity evaporation; in air, little impurity evaporation takes place; impurity transfer will occur from Morganite or similar commercial  $Al_2O_3$  crucibles to cleaner samples.
- 2) Cold wall furnaces favor the evaporation of impurities while alumina tube furnaces tend to transfer impurities to the sample unless the sample is protected.
- 3) Sapphire materials are cleaner than Lucalox materials which are cleaner than Morganite or other alumina materials.
- 4) Those studies where details are not explicitly recorded

are down rated, i.e., assumed to be less pure.

Using these criteria on the experimental conditions listed in Table I, the literature data support the contention that the higher purity samples have lower surface diffusivities for all but perhaps 1 or 2 of the 13 values listed. The results are tabulated in the order of the ranking of the diffusivities at 1600-1700°C.

### III. GOALS OF THIS THESIS RESEARCH

The primary goals of this research are a) to determine reliable surface diffusion coefficients for temperatures lower than the available literature data because a considerable amount of sintering occurs in this temperature regime, b) to compare the results with those in the literature, and c) to determine the effects of impurities on the surface diffusivity, especially the effect of MgO.

The technique chosen for the measurement of the surface diffusion coefficient is grain boundary grooving. Of the available techniques, thermal grooving offers the advantages of relatively easy sample preparation. Because of the small thermal groove widths resulting from the lower temperature annealings, the use of the scanning electron microscope is necessary. Air is the preferred atmosphere because this is the ambient for much of the available sintering data. Also, vapor transport of impurities is significantly reduced in air. Further steps taken to prevent the transport of impurities include wrapping the samples in platinum foils, embedding these in a powder of nominally the same composition as the samples, and containing this arrangement in closed crucibles.

#### IV. EXPERIMENTAL PROCEDURES

##### A. Sample Preparation

##### 1. Materials

Four types of  $\text{Al}_2\text{O}_3$  were used in experiments on thermal grooving; the specific materials are listed in Table II. Most study involved a commercially available material, Lucalox<sup>R</sup>, General Electric Company's translucent alumina which contains Mg-doping above its solubility limit. Three subgroups of these samples are distinguished: (1) lamp tubes precut to a convenient length ( $\sim 3\text{mm}$ ) and heat-treated in vacuum at  $1875^\circ\text{C}$  as noted in Table III, (2) as-received lamp tubes cut to a similar size, and (3) as-received rod sliced into discs of  $1.5\text{ mm}$  thickness.

The three other types of  $\text{Al}_2\text{O}_3$  were nominally pure. One of these was a high-purity, polycrystalline material produced by W.H. Rhodes. Thermal grooving samples were cut from as-received bend-bars which had originally been sliced from hot pressed billets. Sapphire tubes that contain several grains per sample were also investigated. Specimens with lengths of  $\sim 3\text{mm}$  were cut from these tubes. Some of this material was doped with magnesia by embedding specimens in a two-phase mixture of alumina and spinel (7:3 molar ratio  $\text{Al}_2\text{O}_3$ :  $\text{MgO}$ ) and annealing at  $1605^\circ\text{C}$  for 7 days.

Finally, pure samples were fabricated from four grades of Baikowski powders: CR1, CR15, CR30, and AS4. The CR-grades are deagglomerated, jet-milled mixtures of  $\gamma$  and  $\alpha$ - $\text{Al}_2\text{O}_3$ , where the number indicates the specific surface area in  $\text{m}^2/\text{gm}$ . The AS4 is an  $\gamma$ -powder derived from an alum recrystallized four-times; the specific surface area is  $>100\text{ m}^2/\text{g}$ . Processing included loading powder under a laminar flow hood into methanol-



TABLE II. Samples Used in Thermal Grooving Experiments

- RLC - Sample W2 is from R. L. Coble [discussed in Coble (1961)]; 0.3  $\mu\text{m}$  Linde A alumina powder milled with 0.25 w/o MgO, pressed at 10 TSI, sintered at 1675°C for 10<sup>4</sup> minutes in air.
- LTVA - Lucalox<sup>R</sup>\* lamp tubes (9mm O.D. x ~0.8 mm wall thickness); vacuum heat-treatments by J. E. Blendell [discussed in Blendell (1979)] as noted in Table III by # hours at 1875°C/# cooling rate K-sec<sup>-1</sup> to 1100°C then furnace cool to R.T.; grain sizes, 40-100+  $\mu\text{m}$ .
- LTAR- As-received Lucalox<sup>R</sup>, commercial lamp tubes; grain sizes 10-40  $\mu\text{m}$ .
- LD - Lucalox<sup>R</sup> Discs cut from 8 mm rod, sample # 35-2-4 from R. J. Charles\*\*, grain sizes 10-30  $\mu\text{m}$ .
- BK - Baikowski\*\*\* deagglomerated powders, nominally 99.99% Al<sub>2</sub>O<sub>3</sub>; number on CR-grade in specific surface area; samples fabricated by isostatically pressing at 50 KSI, vacuum (< 10<sup>-5</sup> torr) fired at 1550°C for 95 hours; relative density 99.6%, grain sizes 5-100  $\mu\text{m}$ .
- ADL - A.D. Little<sup>+</sup> sapphire tubes (7 mm O.D. x ~0.8 mm wall thickness); float zone crystal growth using a laser heat source; feed stock is alum derived powder, ~99.98% pure<sup>++</sup>; several large grains (>100  $\mu\text{m}$ ) per tube.
- RHP -- Samples hot pressed from high purity powder by W.H. Rhodes while at AVCO<sup>+++</sup> [discussed in Rhodes and Cannon (1969) and Cannon et al. (1980)]; typical impurity levels by mass spectrographic analysis gave 80 ppm cation and 140 ppm anion; grain size < 10  $\mu\text{m}$ , most 1-2  $\mu\text{m}$ .

---

\* General Electric, Cleveland, OH, commercial product.

\*\* General Electric Research Laboratory, Schenectady, NY.

\*\*\* Baikowski International Corp., Charlotte, N.C.

<sup>+</sup> A.D. Little Co., Cambridge, MA.

<sup>++</sup> J. Haggerty, MIT, private communication.

<sup>+++</sup> AVCO Corp., Lowell, MA.

cleaned, standard, black, isostatic press bags. Excess air was evacuated and the sample were isostatically pressed at 50 KSI. Preheating samples at  $\sim 200^{\circ}\text{C}$  in air for four hours was done prior to vacuum firing<sup>+</sup> at a total pressure  $< 2 \times 10^{-5}$  torr. The powder compacts were held in an open Mo-crucible; the heater and heat shields are made of tungsten. Sintering times of 1, 12 and 95 hours were used at a temperature of  $1550^{\circ}\text{C}$ . An immersion density of each sample was measured at the end of each time interval. The CR-grade materials attained a final relative density of 99.6% while the AS4 sample reached 97.4% relative density. The AS4 material was not used in thermal grooving experiments because of its low relative density.

## 2. Polishing

Samples were polished with a series of diamond pastes ranging from a maximum size of  $15\ \mu\text{m}$  (usually  $5\ \mu\text{m}$ ) down to  $1/4\ \mu\text{m}$  as the final size. Most of the LTVA samples were polished prior to heat-treatment so typically less material needed to be removed. However, samples were polished in groups of four or more so it is unlikely that less than an average grain thickness was polished off every sample, given the slight sample height variations. Therefore, all samples probably started with grain boundaries that were inclined with respect to the polished surface.

One sample from experiment GBG27, on which the thermal groove width was measured as a function of time, was repolished taking off only enough material ( $\sim 0.5\ \mu\text{m}$ ) to reflaten the surface. This sample was then annealed under similar condition to GBG27, see Table III.

---

<sup>+</sup>Richard D. Brew Co., Model 1968 Vacuum Furnace, Concord, NH.

TABLE III. Experimental Procedures

GBG #	Sample	History	T (°C)	t (hr)	Wash	Powder <sup>+</sup>	Atm
W2	RLC	see Table II	1195	40	1	XA-139 unground	air
1A	LTVA	unkn/unkn	1195	3	1	XA-139 unground	air
1B				17	1		
2	LTVA	unkn/unkn	1170	11.2	1	XA-139 unground	air
3	LTVA	unkn/unkn	1080	36.8	1	XA-139 unground	air
4	LTVA	19h/1 K/s	1328	10	2a	XA-139 unground	air
5	LTVA	8h/0.1 K/s	1086	104.5	2a	XA-139 unground	air
6	LTVA	20h/10 K/s	1250	33.3	2a	XA-139 unground	air
7	RHP	HP-1326-1	1131	21.6	2a	XA-139 unground	air
8	LTVA	20h/100 K/s 3h/1 K/s	970	89.5	2a	XA-139 unground	air
9	LTVA	4h/10 K/s 4h/100 K/s	905	232	2b	XA-139 unground	air
10	RHP	HP-1326-1	970	231	2b	XA-139 unground	air
11	LTVA	6h/100 K/s <sup>+++</sup> 20h/100 K/s	1296	300	2b	XA-139 unground	air

TABLE III (Cont'd.)

GBC #*	Sample**	History**	T (°C)	t (hr)	Wash***	Powder†	Atm
12	LTVA	8h/0.25 K/s	1306	111.3	2b	XA-139 unground + 0.5 w/o MgO (as nitrate)	air
13	LTVA	8h/0.25 K/s	1296	32.5	2b	Same as GBC12	air
14	LTVA	8h/0.25 K/s	1032	403.3	2b	Linde A + ~5 w/o MgO	air
15	RHP	HP 1326-1	1247	394	2b	Linde A	air
16	LTVA	8h/0.25 K/s	1485	86.8	2b	Linde A + 0.5 w/o MgO	air
17	LTAR	"as-received"	1456	286	2b	Baikowski CR15 + 5 w/o MgO	air
18A	LTAR	"as-received"	950	2280	3	Baikowski CR15 + 5 w/o MgO	air
18B	LTAR	"as-received"	950	3216	3	Baikowski CR15 + 5 w/o MgO	air
18C	LTAR	"as-received"	950	5496	3	Baikowski CR15 + 5 w/o MgO	air
19	LTAR	"as-received"	1394	2667	3	Baikowski CR15 + 5 w/o MgO	air
20	LTAR	"as-received"	- T drift -	-	3	Baikowski CR15 + 5 w/o MgO	air

TABLE III (Cont'd.)

CBG #	Sample**	History**	T (°C)	t (hr)	Wash***	Powder+	Atm
21	LTAR	"as-received"	-	T drift -	3	Baikowski CR15 + 5 w/o MgO	air
22	LTAR	"as-received"	1192	480	3	Baikowski CR15 + 5 w/o MgO	air
23	LD	"as-received"	-	T drift -	3	Baikowski CR15 + 5 w/o MgO	air
24	LD	"as-received"	1092	1163	3	Baikowski CR15 + 5 w/o MgO	air
25	LD	"as-received"	1842	0.65	3	Free evaporation	vacuum
26	LD	"as-received"	1842	0.65	3	low density com- pacts. 5:1 molar ratio Baikowski CR15: MgO	vacuum
27A	LD	"as-received"	1602	3.0	3	Baikowski CR15 + 5 w/o MgO	air
27B			1602	10	3		
27C			1602	30	3		
27D			1602	62	3		
27E			1602	103	3		
27F			1602 <sup>++</sup>	291	3		

TABLE III (Cont'd.)

GBG #*	Sample**	History**	T(°C)	t (hr)	Wash***	Powder <sup>+</sup>	Atm
28	BK1,15,30	See text	1602	1	3	Baikowski CR15	air
29A	ADL	See Table II	1602	3	3	Baikowski CR15	air
29E			1602	11.3	3		
29C			1602	31.5	3		
29D			1602	64.7	3		
29E			1602	95	3		
29F			1602 <sup>++</sup>	283	3		
30	ADL	See Table II	1840	6	3	none used	vacuum
31	BK15,30	See Text					
32	ADL+MgO	See text	1594	1	3	low density compacts	air
33	LD(GBG27)	See text		171		4:1 molar ratio Baikowski CR15:MgO	

\* Grain Boundary Grooving Experiment Number

\*\* Samples and History - See Table II

\*\*\* Wash Procedures:

(1) - trichloroethylene and/or acetone wash

TABLE III (Cont'd.)

(2) -trichloroethylene and/or acetone wash

-boil 2-5 minutes in aqua regia

-at R.T., 2-5 minutes in HF + few drops  $\text{HNO}_3$

-boil 2-times in de-ionized  $\text{H}_2\text{O}$

(a) final rinse in trichloroethylene

(b) final rinse in pure ethyl alcohol

(3) -acetone rinses

-boil 2-5 minutes in  $\text{HNO}_3$  + few drops HCl

-at R.T., 2-5 minutes in HF + few drops  $\text{HNO}_3$

-boil 2-times in de-ionized  $\text{H}_2\text{O}$

-final rinse in pure ethyl or methyl alcohol

<sup>+</sup>XA-139 -Aluminum Co. of America, Pittsburgh, PA: Bayer Process  $\text{Al}_2\text{O}_3$ , nominally 99.98%, unground, coarse "mudcake" granules  $\sim 100 \mu\text{m}$  diameter.

Linde A -Linde Division of Union Carbide, San Diego, CA; alum derived powder, nominally 99.98%, mixture of  $\gamma$  and  $\alpha$ - $\text{Al}_2\text{O}_3$ ,  $\sim 0.2 \mu\text{m}$  particle size.

TABLE III (Cont'd.)

MgO	-for GBC 12-GBC14; Mallinckrodt Chemical Works, St. Louis, MO; reagent grade oxide or nitrate
MgO	-for GBC16-GBC29; C.A. Handwerker, MIT; derived from hydroxide via autoclave of 99.999% Mg-metal
++	Temperature of GBC27F drifted up 15°C for $\leq 0.67$ total time, total time = 291 hrs.
	Temperature of GBC29F drifted down 15°C for $\leq 0.67$ total time, total time = 283 hrs.
+++	Primary sample



The quality of the polish was tested at random intervals during the final lapping with (a) optical microscopy using 100-400 times magnification, (b) two-beam interference microscopy at 250 times magnification, and/or (c) most thoroughly using SEM with magnifications up to 100,000 times, after the entire cleaning procedure noted below.

### 3. Acid Washings

The various acid washings and rinsing procedures used are listed in Table III. In all cases the samples were handled with cleaned plastic or stainless steel tweezers while wearing talc-free plastic gloves.

### 4. Specimen Configuration and Anneals

For air fired samples, the samples were wrapped in a platinum foil and buried in  $Al_2O_3$  powder; the powder compositions and sources are noted in Table III. After cleaning the samples (and platinum foils), pairs were placed with polished faces abutted and wrapped as tightly as possible in the foil in order to keep powder off the polished surfaces. This sample arrangement was contained by an alumina crucible within a crucible,\* as shown in Figure 9. Anneals were carried out in alumina tube furnaces. The temperature was measured by a Pt/Pt-10% Rh thermocouple equipped with a standard ice-point apparatus. The temperature was recorded at intervals which depended on the length of the experiment and the stability of the particular furnace setup. In some cases, chart recorders were used for the entire run; in others only the stability over a 24-48 time period was recorded. The temperature was controlled to within  $1^\circ C$  (except as noted) and the actual value known within  $\pm 5^\circ C$  due to thermocouple uncertainty.

---

\* Coors Alumina.

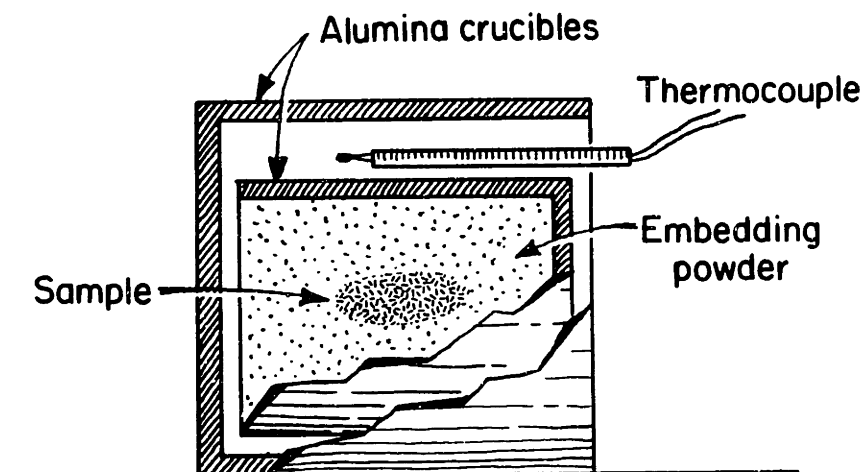


Figure 9 Sample embedding arrangement

Samples from which multiple time data were measured were treated as though each interval were a separate experiment; washing and packing were conducted as noted above.

Three different experimental conditions were used for the vacuum fired samples. The freely evaporating samples were placed on the bottom of an open tungsten crucible with the polished surface exposed to the vacuum. In the second configuration, the specimens were sandwiched between pre-fired, very low-density compacts as a simulation of the powder bed incorporated above. This sample arrangement was contained within a covered tungsten crucible. Lastly, three pure alumina materials were contained within a high-purity alumina crucible<sup>\*</sup> with a tightly-fitted lid. No powder was used in this experiment. Anneals were carried out in a Brew vacuum furnace equipped with a tungsten heater and tungsten heat shields. The temperature was measured with a series of optical pyrometers<sup>\*\*</sup> on flat surfaces and from black-body radiation holes drilled in tungsten bodies. Comparisons were made with a Pt/Pt-10% Rh thermocouple over the appropriate temperature ranges. A confidence interval of  $\pm 10-15^{\circ}\text{C}$  was reached, with the greatest uncertainty at the lowest temperatures.

#### B . Measurement of Groove Width and Depth

Two-beam interference microscopy was used to measure the width and depth of the thermal groove when the width was greater than  $1.0\ \mu\text{m}$ . This width is the practical resolution limit for the 250X magnification photomicrograph. Most groove widths and depths were measured using a machinist's ruler under a stereo microscope using 10-20X magnification.

---

\* Union Carbide Crystal Products Division, San Diego, CA.

\*\* (1) Coloratio Pyrometer  
(2) Leeds and Northrup  
(3) Pyro Micro-Optical Pyrometer

The scanning electron microscope<sup>\*</sup> (SEM) was used to determine the majority of thermal groove widths in this study. Conductive coatings are required for these samples. Au/Pd films with a thickness of 100-300 Å were applied using an Ar-sputter coater.<sup>\*\*</sup> An alternative method consisted of evaporating 50-100 Å of carbon followed by 100-150 Å of 60Au/40Pd using a rotating-tilting stage to expose all segments of the surface to direct coating. Either preparation technique gave useful resolution on the order of 100 Å.

The use of stereo pairs to determine the thermal groove width was investigated early in this study. However, the apparent groove width was primarily influenced by the brightness:darkness contrast in the photomicrograph due to the orientation of the surface. The use of stereo pairs was therefore discontinued. Using more sample tilt and electronically adjusting the output signals on the scanning electron microscope were steps taken to maximize contrast in the SEM micrographs. Minimum groove widths were approximately 600 Å.

The scanning electron microscope introduces distortions on the recorded image due to the orientation of each surface element with respect to the electron beam axis (optic axis) and electron detector. The shape or contour of the surface is also important. Details of geometric corrections are presented in Appendix II, where it is shown that the pertinent problem reduces to the projection of a plane with small perturbations onto a plane normal to the optic axis. Figure 10 defines the geometry and correction terms. Grain boundary groove widths were corrected

---

\* JEOL JSM-35

\*\* AMR 1000A

Hummer III Sputter-Coater

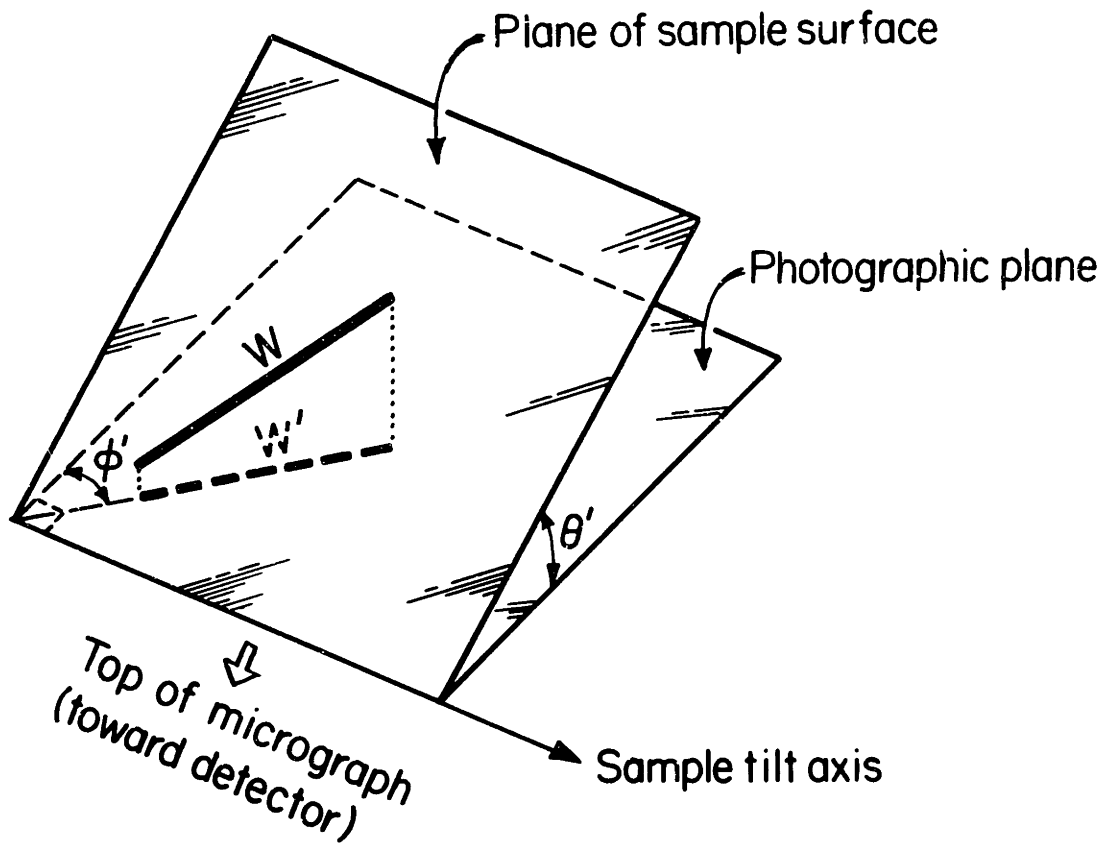


Figure 10

The SEM projection geometry

for this distortion using:

$$W = W' \left[ \cos^2 \phi' \left( \frac{1}{\cos^2 \theta'} - 1 \right) + 1 \right]^{1/2} \cdot \frac{1}{M} \quad (28)$$

where  $W$  is the actual groove width and  $W'$  the apparent groove width on micrograph;  $\theta'$  is the sample tilt angle and  $\phi'$  the angle between the grain boundary and tilt axis; and  $M$  is the magnification.

Comparisons of the thermal groove widths of specific boundaries as determined by both the SEM technique and two-beam interferometry were made in order to test the reliability of these measurements. These results are included in Appendix III. The agreement was generally within a few percent.

A calibration check of the AMR 1000 A scanning electron microscope was accomplished with 1.09  $\mu\text{m}$  latex spheres\* coated by the evaporation technique. For this size sphere, the actual error in calibration depends on the thickness of the coating. The error is at most 5%, but probably  $\leq 2\%$ . The ranges of observed groove widths on the same sample in both SEM microscopes gave nearly identical results.

Surface chemistry was documented for a few specimens with Scanning Auger Spectroscopy.\*\* Semiquantitative analysis was performed using the procedures recommended in the Physical Electronics Handbook (1976).

The grain boundary groove profiles were investigated using two-beam interferographs. The most convenient method involved making a 35 mm slide and projecting the image onto a flat surface normal to the projection direction. Another 20-40X magnification was gained by tracing interference lines onto paper held against the flat surface. In this manner the

---

\* Ernest Fullam Co.

\*\* Physical Electronics

symmetry of the thermal groove, and the dihedral angle could be investigated.

## V. RESULTS

The use of the scanning electron microscope to quantitatively measure thermal groove widths is not a standard technique. It is of interest to note the resolution capabilities. The absolute minimum width measured in this study was  $0.06 \pm 0.02 \mu\text{m}$ , Figure 11. A more typical "near" minimum thermal groove width is  $0.30 \pm 0.03 \mu\text{m}$ , Figure 12.

The thermal grooving rates and profile shapes are quite variable from boundary to boundary on any given sample and are variable along the length of some individual boundaries. These results are tabulated in Tables IV to VI. The measured dihedral angles were also found to be variable, as shown in Table VII. For all optical measurements and most SEM measurements, the variability in the groove widths is larger than the uncertainty in the measurement of any one thermal groove width. The development of faceting is at least partially responsible for the scatter.

Various degrees and types of faceting develop simultaneously with the thermal grooving process. The types of surface texture include "choppy facet networks", linear faceting, and "smooth" surfaces i.e., those with no detectable facets using magnifications up to 20,000X in the SEM. Pure alumina samples always developed facets for the experimental conditions used in this study, while Lucalox specimens exhibited the entire range of surface features. The development of facets was not as severe on the Lucalox surfaces where MgO had been added to the embedding powder; however, a degree of faceting still evolves on most specimens. Generally, the degree of faceting depends on both the temperature and the sample impurity levels.

Various impurities were found to be inhomogeneously distributed on all four alumina materials using Auger spectroscopy, see Table VIII.



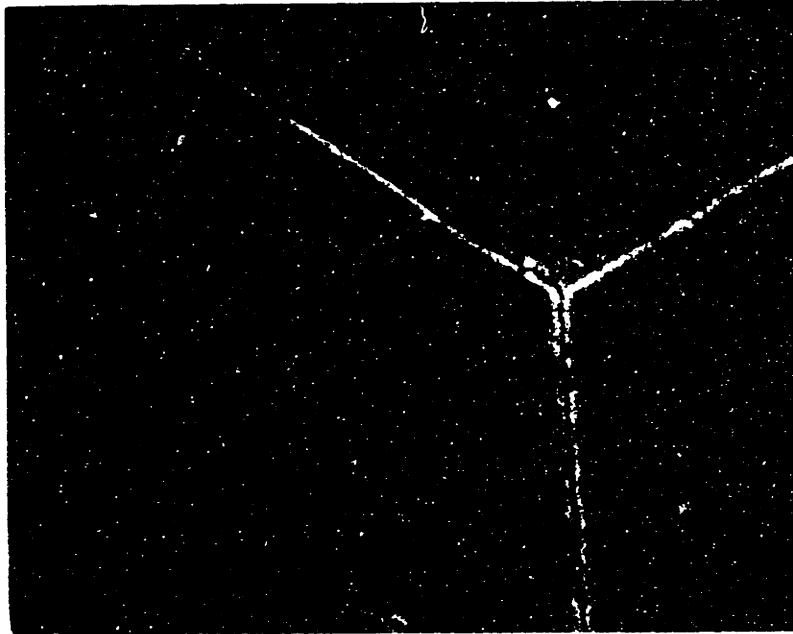


Figure 11 - The limit of resolution using the SEM for measurement of thermal groove widths (GBG9, LTVA, 905°C, 232 hours, 30° tilt) bar = 0.2  $\mu\text{m}$ .



Figure 12 - Near the limit of resolution using the SEM for measurement of groove widths (GBG18C, LTAR, 950°C, 229 days, 60° tilt) bar = 0.3  $\mu\text{m}$ .

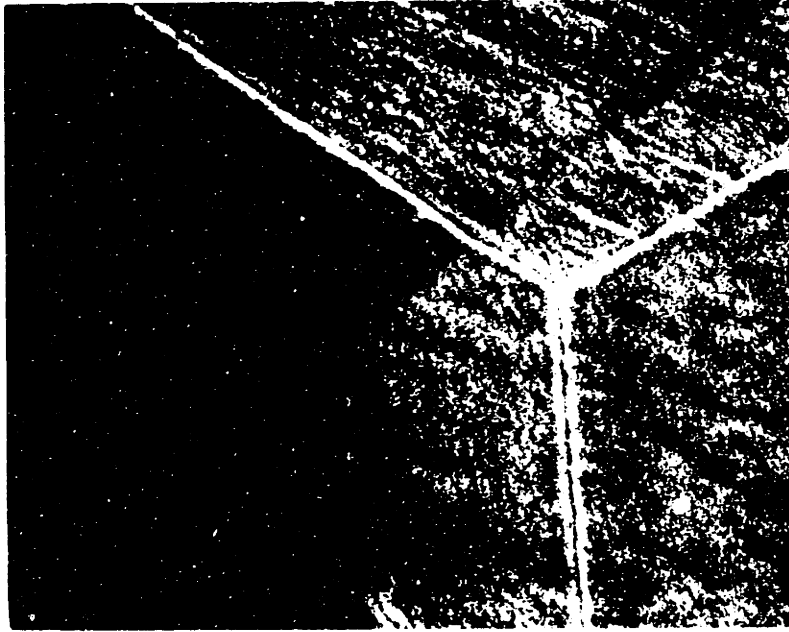


Figure 11 - The limit of resolution using the SEM for measurement of thermal groove widths (GBG9, LTVA, 905°C, 232 hours, 30° tilt) bar = 0.2  $\mu\text{m}$ .

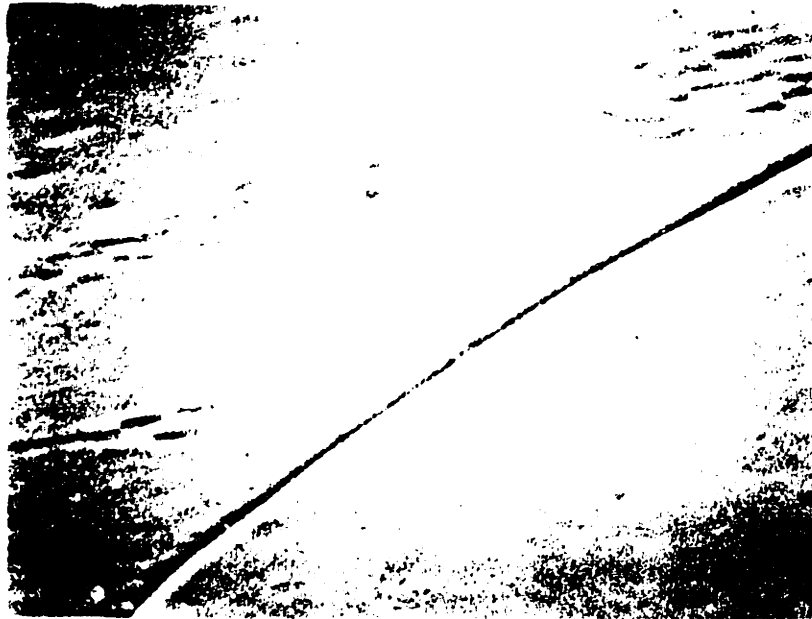


Figure 12 - Near the limit of resolution using the SEM for measurement of groove widths (GBG18C, LTAR, 950°C, 229 days, 60° tilt) bar = 0.3  $\mu\text{m}$ .

Surface segregation and second phase particles are indicated. Variable amounts of second phase are also seen in the SEM for the different types of alumina. The thermal grooving profiles and kinetics are different for samples with different impurity levels.

The following section presents a detailed evaluation of the groove formation kinetics and surface characteristics to indicate the sources of variability and to determine the best estimate of the surface diffusivity.

TABLE IV. Thermal Groove Width for Individual Boundaries as a Function of Time for the LD material, GBC27

Area Boundary	Groove Width in Microns at Times:					
	A (3 hrs)	B (10 hrs)	C (30 hrs)	D (62 hrs)	E (103 hrs)	F (291 hrs)
2-1	1.60-1.80	2.38-2.86	3.33-3.65(GBM)	3.49-3.81(GBM)	4.76-5.08(GBM)	GBM
2-3	1.43	1.91-2.22	2.54-2.86	3.18	3.18-3.49	4.76-5.08
2-5	1.30-1.50	1.60-2.0 (GBM)	1.91-2.06(GBM)	1.91-2.38	3.18-3.33	GBM
2-9	-	2.80-3.20	3.49-3.75	3.81-4.45	5.08-5.20	6.67-7.14
31-1	-	1.87-2.28	2.87-2.95	3.11-3.56	3.75-3.96	5.42-5.83
31-2	-	1.59-1.91	2.11-2.53	3.10-3.30*	3.10-3.30*	4.8 (GBM)*
31-3	-	2.49-2.69	3.08-3.49	4.15-4.35	4.70-4.92	6.74-7.10
31-4	-	<1.00	1.20-1.60	1.40-1.80	2.00-2.40	3.60-4.00
31-5	-	1.50-1.70	2.22-2.44	2.74-2.85	3.13-3.54	5.0 -5.21
31-6	-	2.30-2.50	3.33-3.67	4.10-4.30	4.38-4.58*	6.25-6.40*
31-7	-	2.10-2.32	3.22-3.33*	3.73-3.95*	3.96-4.17*	6.04-6.25*
31-8	-	1.66-2.08	3.00-3.28	3.56-3.73	3:75-4.17	6.25-6.88
31-9	-	2.38-2.54	2.95-3.16	3.54-3.75	3.96-4.17	6.10-6.25
31-10	-	2.95-3.39*	3.89-4.11*	4.90-5.04*	5.00-5.21*	7.08-7.29*

TABLE IV (Cont'd.)

Area Boundary	Groove Width in Microns at Times:					
	A (3 hrs)	B (10 hrs)	C (30 hrs)	D (62 hrs)	E (103 hrs)	F (291 hrs)
3-1	1.75-2.06	2.50-2.71	3.20-3.33	3.54-3.96	4.17-4.58	6.25-6.46
3-2	1.60-1.91	2.08-2.50	2.92-3.54	3.97-4.17	4.38-4.79	GBM
4-1	1.43-1.59	2.29-2.71	3.54-3.75	4.58-5.00	5.21-5.42	8.33-8.54
4-2	-	2.08-2.50	2.71-2.92	3.33-3.75	3.75-3.96	5.83-6.04
4-3	-	1.60-2.00	2.08-2.50	2.86-3.00	2.98-3.17	4.58-4.79
44-1	-	2.00-2.10	2.40-2.60	3.0 -3.20	3.40-3.60	5.0 -5.20

GBM = Grain Boundary Migration

\* = Height difference between adjacent grains

TABLE V. Thermal Groove Width of Individual Boundaries as a function of Time for ADL, GBC29

Area* Boundary	Groove Width in Microns at Times:					
	A (3 hrs)	B (11 hrs)	C (32 hrs)	D (65 hrs)	E (95 hrs)	F (283 hrs)
1a	1.40-1.80	1.60-1.80	1.80-2.0	1.80-2.0	2.0-2.20	2.0-2.40
1b	1.20-1.40	1.60-1.80	1.70-1.90	1.80-2.0	2.0-2.40	2.40-3.0
2a	1.0-1.40	1.40-1.60	1.60-1.80	1.60-1.80	1.90-2.10	2.20-2.40
2b	1.20-1.40	1.40-1.60	1.80-2.00	1.80-2.0	2.0 -2.20	2.20-2.60
2c	0.80-1.20	1.60-1.80	1.60-1.80	2.00-2.20	2.40-2.80	2.40-2.80
2d	-	-	1.90-2.10	2.00-2.20	2.20-2.40	2.60-2.80
3	1.40-1.60	1.80-2.0	1.80-2.0	1.80-2.00	-	2.80-3.20
5	1.60-1.80	1.60-1.80	1.80-2.0	1.90-2.10	2.0 -2.20	2.0 -2.40

\*Small letter denotes location along specific boundary

Table VI. Summary of Grain Boundary Grooving Results

GBG #	Sample	T(°C)	t (hrs)	No of Grooves	Range of Width ( $\mu\text{m}$ )*	log WD <sub>S</sub>	log D <sub>L</sub>	Comments
W2	RLC	1195	40	-	-	-	-	
1	LTVA	1195	17	-	-	-	-	Data judged unreliable due to quality of polish and/or impurities
2	LTVA	1170	11.2	-	-	-	-	
3	LTVA	1080	36.8	-	-	-	-	
4	LTVA	1328	10	7	0.35	-17.96	-12.96	hillocks, range of facets types, second phase(?) <sup>+</sup>
5	LTVA	1086	105	9	0.10	-21.23	-15.68	near limit of resolution
6	LTVA	1250	33.3	22	0.25	-19.10	-13.94	hillocks, range of facets types
7	RHP	1130	21.6	13	0.11	-20.37	-14.86	small grain size, rolling hills surface (developing facets?)
8	LTVA	970	90	12	0.06	-22.10	-16.32	near limit of resolution
9	LTVA	905	232	16	0.13	-20.89	-15.42	near limit of resolution
10	RHP	970	231	29	0.08	-23.23	-17.28	some near limit of resolution, rolling hills surface (developing facets)
					0.20	-21.19	-15.75	
					0.08	-22.01	-16.35	
					0.20	-20.41	-15.16	

Table VI. (Cont'd.)

GBC #	Sample	T(°C)	t (hrs)	No of Grooves	Range of Width (μm)*	log WD <sub>s</sub>	log D <sub>L</sub>	Comments
11	LTVA	1296	300	34	0.30 1.50 (+opt.)	-19.72 -16.93	-14.64 -12.55	large range, faceted surface, last expt. w/o MgO-doped powder
12	LTVA	1306	111	18	0.28 1.13 (+opt.)	-19.41 -16.98	-14.30 -12.48	plus MgO-doped powder, "smoother" appearance, typical surface <sup>++</sup> , large range.
13	LTVA	1296	32.5	18	0.19 0.47	-19.55 -17.98	-14.27 -13.09	typical surface <sup>++</sup>
14	LTVA	1032	403	26	0.26 0.70	-20.18 -18.46	-15.04 -13.75	rough surface on occasional grain, otherwise typical <sup>++</sup>
15	RHP	1247	394	16	0.20 0.80	-20.56 -18.15	-15.30 -14.08	most grains are faceted, large range
16	LTVA	1485	87	30	0.60 2.8 (+opt.)	-17.93 -15.25	-13.15 -11.15	many moving boundaries one sample, large grain size other, some faceted areas, otherwise typical <sup>++</sup>
17	LTAR	1456	286	35+	1.0 3.2 (+opt.)	-17.57 -15.55	-13.60 -11.49	boundary migration in areas, typical appearance <sup>++</sup>



Table VI. (Cont'd.)

GBC #	Sample	T(°C)	t (hrs)	No of Grooves	Range of Width (μm) <sup>#</sup>	log WD <sub>S</sub>	log D <sub>L</sub>	Comments
18A	LTAR	950	2280	5	0.11	-22.45	-16.94	near limit of resolution in
					0.20	-21.41	-16.16	A, second phases at some
18B	LTAR		3216	5	0.24	-21.25	-16.07	grain boundaries in B, some
					0.35	-20.59	-15.58	poorly polished areas, some
18C	LTAR		5496	15	0.30	-21.09	-16.02	typical areas <sup>++</sup>
					0.70	-19.62	-14.91	
19	LTAR	1394	2667	23	2.0	-17.35	-13.10	smaller grain size, a few
					3.5 <sup>(+opt.)</sup>	-16.38	-12.37	boundaries migrated, typical surface <sup>++</sup>
20	LTAR	-	-	-	-	-	-	drifting T; second phases
								along many grain boundaries
21	LTAR	-	-	-	-	-	-	thermocouple failure
22	LTAR	1192	480	5	0.14	-21.28	-15.87	second phase along many grain
					0.35	-19.69	-14.68	boundaries, most grooves
								asymmetric, some faceting
23	LD	-	-	-	-	-	-	furnace failure
24	LD	1092	1163	7	0.18	-21.26	-15.96	second phases (Ca, Mg, Si, Al)
					0.45	-19.67	-14.77	along many grain boundaries, <sup>∞</sup>
								no faceting noted.

Table VI. (Cont'd.)

GBG #	Sample	T(°C)	t (hrs)	No of Grooves	Range of Width (μm)*	log WD <sub>S</sub>	log D <sub>L</sub>	Comments
25	LD	1842	0.65	26	0.91	-15.00	-10.40	free evaporation; some raised grain boundaries; many migrating grain boundaries; smooth or linear facets only
					3.0 (+opt.)	-12.93	- 8.85	
26	LD	1842	0.65	10	3.2	-12.82	- 8.77	partial WO <sub>x</sub> contamination; smooth or linear facets only
					5.1 (+opt.)	-12.01	- 8.16	
27A-F	LD	1602	10	(20)	1.6	-15.26	-	max./min. for boundaries: W <sub>wt</sub> <sup>1/n</sup> where 3 < n < 4, smooth or linear facets only, second phase grains (Ca, Si, Al, Mg) typical appearance <sup>++</sup>
					2.7	-	-10.23	
					3.2	-14.05	-	
					1.6	-	-10.91	
28	BK1	1602	1.0	19	0.55	-16.11	-11.3	
					1.24			
BK15				5	0.60			
					1.0			
BK30				16	0.60			
					1.28	-14.65	-10.20	

TABLE VI (Cont'd.)

GBG #	Sample	T (°C)	t (hrs)	No of Grooves	Range of Width* (μm)	log WD <sub>s</sub>	log D <sub>L</sub>	Comments
29A-F	ADL	1603	3	(8)	0.8	-15.94	-11.29	min./max. at short time
			3		1.8(opt.)	-14.53	-10.24	only; severely faceted surface and groove profile**
30	ADL	1840	6	6	3.6(opt.)	-13.56	-9.57	faceted surface and groove profile**
					4.4	-13.22	-9.31	
31	BK15	1840	6	6	3.2(opt.)	-13.77	-9.72	considerable grain growth, many linear facets
					4.8	=13.06	-9.19	faceted groove profile**
32	ADL+MgO	1594	171	5	1.8			
					3.2			
33	LD(GBG27)	1594	1	8	0.8			similar to GBG27, ~1/2 μm removed on repolish
			171	8	3.6			
					6.8			

\* widths determined from SEM micrographs unless otherwise noted, opt. = optical microscopy.

† not verified by EDAX

†† typical surface - mixture of smooth surfaces, linear facets, and faceted grains.

\*\* these facets are readily observed in SEM, but barely detected at 250-400X using optical microscopy.

TABLE VII. Measured and Calculated Dihedral Angles

#*	Material	W ( $\mu\text{m}$ )	d ( $\mu\text{m}$ )	$\theta$ -calc.	$\theta$ -meas.
27-31-1C	LD	3.06	0.192, 0.241	147°, 139°	144°
27-31-1D	LD	3.44	0.251, 0.289	142°, 137°	155°
27-31-3C	LD	3.49	0.270, 0.349	140°, 129°	138°, 123°
27-31-5C	LD	2.44	0.242	130°	132°
27-31-8C	LD	3.11	0.364	122°	114°
27-3-1C	LD	3.33	0.434	117°	118°
27-3-1E	LD	4.22	0.390	133°	150°
27-4-1C	LD	3.89	0.330	136°	137°
27-4-2C	LD	3.04	0.203	145°	122°, 133°
27-4-2C	LD	2.89	0.214	141°	141°, 136°
27-4-2E	LD	3.67	0.377	128°	130°
27-4-3C	LD	2.50	0.234, 0.281	132°, 124°	129°
27-4-3E	LD	3.17	0.304	131°	139°
27-44-1C	LD	2.56	0.186	142°	148°
25-	LD	2.33	0.130	150°	156°
17-	LTAR	2.76	0.154	150°	153°
29-2a-E	ADL	2.00	0.133	145°	149°
29-2a-E	ADL	2.22	0.149	145°	117°
29-3-D	ADL	1.78	0.338, 0.380	96.1°, 89.4°	150°
29-3-D	ADL	2.33	0.219	132°	137°

\* First number is thermal groove experiment number  
 Second number is area of sample  
 Third number is the boundary number, if necessary  
 Letter corresponds to the time as noted in Table IV-4  
 and Table V.

TABLE VIII. Auger Results

Sample	Location	Elements* (normalized w.r.t. the Al-peak at 1378 eV)
GBG11 (LTVA)	5 $\mu\text{m}$ spot	5.2% Ca, 4.0% Si, 2.3% Mg
	115 $\mu\text{m}$ square	5.4% Ca, 3.8% Si, 2.6% Na, 2.5% Mg, 1.5% Fe
	5 $\mu\text{m}$ spot at triple point A	5.8% Ca, 2.8% Mg, 1.5% Si
	5 $\mu\text{m}$ spot at triple point B	6.5% Ca, 3.6% Si
	5 $\mu\text{m}$ spot at "surface bump"	8.2% Ca, 3.6% Mg, 2.9% Si
GBG16 (LTVA)	5 $\mu\text{m}$ spot	100% Mg, 30.3 %K, 21.2% Na, 21.2% Fe, 12.1% Ca, 5.5% Si
	115 $\mu\text{m}$ square	15.5% Ca, 2.9% Si, 0.7% Mg
GBG10 (RHP)	115 $\mu\text{m}$ square	11.0% Sn, 8.8% Sb, 1.1% Na
	115 $\mu\text{m}$ square	13.0% Na, 11.1% Fe, 9.3% Sn, 7.4% Sb
	5 $\mu\text{m}$ spot	7.8% Sn, 5.5% Sb
GBG 15 (RHP)	115 $\mu\text{m}$ square	6.8% Si
	115 $\mu\text{m}$ square	4.6% Si, 1.7% Na
	5 $\mu\text{m}$ spot	3.8% Si
GBG 31 (BK-CR15)	5 $\mu\text{m}$ spot	3.2% Si
	3-1 $\mu\text{m}$ spots, 2-115 $\mu\text{m}$ squares	5-10% W, 2-5% Ca, $\leq$ 1% Si
GBG 31 (BK-CR 30)	3-1 $\mu\text{m}$ spot, 2-115 $\mu\text{m}$ squares	1-2% W, 1-2% Ca, $\leq$ 1% Si, occasional trace (<1%) Fe, Ni, Mg
	2-1 $\mu\text{m}$ spots	1% W, 1% Si, <1% Co(?), <1% Ca

\* -All spectra at 5 keV, except the first on GBG11 at 3 keV.

## VI. ANALYSIS OF RESULTS

### A. Microstructure Characterization

#### 1. Composition

##### (a) Auger Electron Spectroscopy Results

Scanning Auger electron spectroscopy (SAS) was used to characterize the level of surface impurities on a limited number of locations on the as-annealed surfaces of LTVA, RHP, BK and RHP samples. These data are reported as peak height ratios, normalized with respect to the characteristic Al-peak at 1378 eV, Table VIII. The actual surface concentrations probably vary considerably from the values listed since elemental sensitivity factors were omitted from these calculations, and because carbon, although <10% of the oxygen level, may be present as CO or CO<sub>2</sub>. Sensitivity factors are neglected because the values reported [Phi Handbook (1976)] are not for an oxide matrix. Determination of these factors requires fracture surfaces formed under conditions of high vacuum in order to avoid problems created by preferential loss of one of the elements while sputter-cleaning. Spectra have been recorded under such conditions for MgAl<sub>2</sub>O<sub>4</sub> by Johnson and Stein (1975), and for CaAl<sub>2</sub>O<sub>4</sub> by Johnson and Coble (1978). The results suggest that the concentrations for Mg would be moderately increased and that for Ca significantly decreased by including sensitivity factors in the scaling of results. However, similar spectra for the other elements of interest are unavailable.

The SAS results for the LTVA samples show that the primary surface impurities are Mg, Si, and Ca. Occasionally, other elements, such as Na, K and Fe, were detected. The high impurity concentrations noted for

one area of specimen GBG16 presumably results from analyzing a second phase grain. The presence of Mg on the surfaces of these samples, although not uniformly detected, apparently indicates that the two-phase embedding powder is useful for preventing the loss of Mg during the annealings. Although only one 115  $\mu\text{m}$  square area was analyzed on each of the two different samples, a comparison of these results shows that the Mg and Si surface concentrations decrease and that the Ca surface concentration increases with increasing annealing temperature.\* This behavior is consistent with an increasing solubility of Mg and Si with increasing temperature, whereas the solubility of Ca is probably considerably smaller for all temperatures due to its large ionic size. The surface chemistry of the LTAR and LD samples was not analyzed; however, based on the amount of second phase seen in the SEM it is reasonable to expect similar or higher impurity levels on these samples.

The SAS results for the two RHP samples gave different results. The sample annealed at the lower temperature showed an appreciable amount of Sn and Sb on the surface, although this may have been caused by the sample mounting tabs. The surface of the second specimen, annealed at a higher temperature, is characterized by a Si concentration similar to that on the LTVA material. Sodium was also found, but not uniformly distributed on either sample. The source of these surface impurities is uncertain. Additional evidence of inhomogeneously distributed impurities appears in the microstructures of the RHP samples in the form of isolated patches of large, elongated grains rather than the typical, small equiaxed grains. This observation suggests that impurities are inhomogeneously distributed and present in the as-received samples.

---

\*These samples were cooled to room temperature in a few minutes.

The surface compositions of the ADL and BK materials were documented for samples that were vacuum annealed at high temperature. These results are reported as ranges for each material because the low level impurity peaks could not be measured accurately; a more accurate measurement is possible if the scale factor is increased.

The ADL and BK samples have a significant level of tungsten contamination, presumably resulting from vapor transport during annealing; the tungsten source is the gray surface skin formed on the BK material during its previous sintering cycle. Neglecting the tungsten contamination the ADL material is the cleanest, exhibiting small levels of Ca, Si, and possibly Co contamination. The BK materials contain more Ca, approximately the same level of Si, and occasional traces of Fe, Ni, or Mg in localized areas. Both materials appear to be considerably "cleaner" than the LTVA or RHP samples, although this may be related to the much higher temperature and vacuum atmosphere used for these ADL and BK samples.

(b) Second Phases

Second phases are frequently found in the Lucalox material; presumably, most are magnesium aluminum spinel. The LD samples displayed more second phase than any of the lamp tubes; the vacuum annealed lamp tubes (LTVA) contained the least second phase. These observations were used to assign a relative scale of impurity levels for the Lucalox materials, the greater the amount of second phase, the higher the impurity level. An example of the microstructure of an LD specimen is shown in Figure 13. The second phases denoted in this micrograph are primarily composed of Al and Mg, with lesser amounts of Ca and Si, as determined by energy dispersive X-ray (EDX) analysis. The concentration



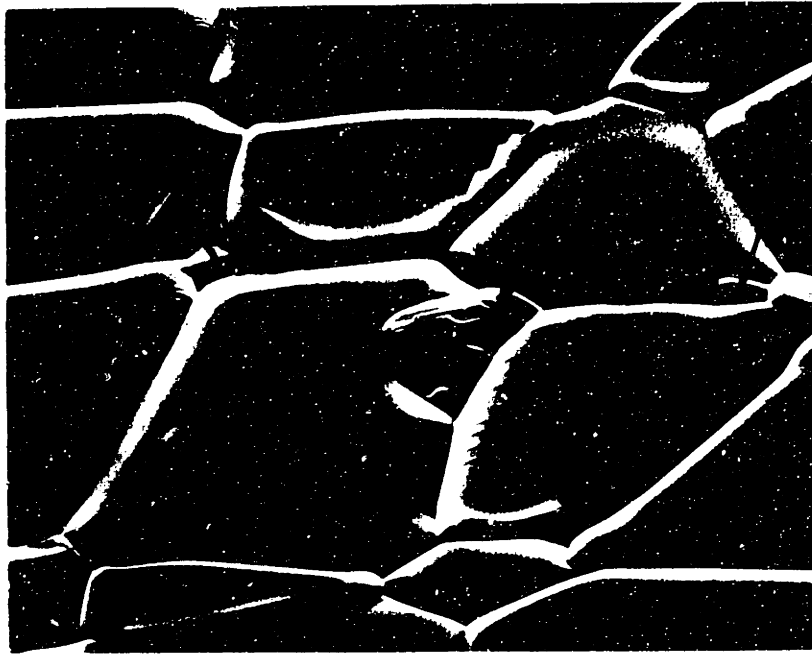


Figure 13 - Second phase, denoted by arrows, on the surface of LD specimens from which time dependent grooving investigated. (GBG27F, 1602°C, 291 hours, 60° tilt) bar = 10  $\mu\text{m}$ .

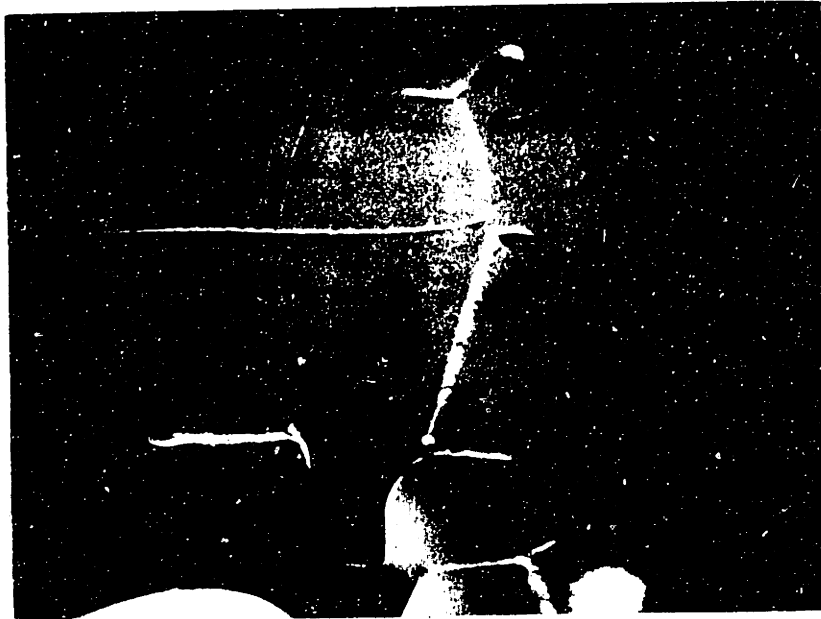


Figure 14 - Second phase exsolved at the free surface along grain boundaries of LD material. Electron beam sensitive area shown by arrow (GBG24, 1092°C, 1163 hrs, 60° tilt) bar = 10  $\mu\text{m}$ .



Figure 13 - Second phase, denoted by arrows, on the surface of ID specimens from which time dependent growth has occurred. (CB24, 1692 C, 291 hours, 60° tilt) bar = 10 μm.



Figure 14 - Second phase evolved at the free surface along grain boundaries of ID material. Electron beam sensitive area shown by arrow (CB24, 1092 C, 1163 hrs, 60° tilt) bar = 10 μm.

of the latter two elements is variable in the second phase grains. These other phases are usually uniformly distributed throughout the sample. Occasionally, a greater concentration of second phase particles is localized within an area several (10-30) grains in diameter. Second phases were not observed on the ADL and BK samples for the experimental conditions used, but there were no long time, low temperature anneals of these.

Second phases, such as shown in Figure 14, were exsolved at the free surfaces along grain boundaries of "as-received" Lucalox material when annealed at lower temperatures; again, this was observed more often for the LD samples, Table VI. This type of precipitation was found in only one region of an RHP specimen (GBG10), and was not seen in the pre-annealed (LTVA) Lucalox samples after comparable low temperature annealings. This does not occur homogeneously throughout the sample, nor is it continuous along all grain boundaries at which the exsolution is proceeding. No quantitative measure was made of the fraction of the sample for which this process occurred. Although it varied from sample to sample, the fraction of boundaries with precipitates was always less than approximately 25%. Thermal groove widths measured in the proximity of these second phases are similar to those from areas in which no precipitation was found. EDX analysis revealed that Al, Ca, Si and Mg are contained in varying ratios in these second phases. Interestingly, this material is sensitive to the electron beam. A small bubble arises, see Figure 14, from the localized area ( $\sim 200 \text{ \AA}^2$  square region) where the beam is rastered.

## 2. Surface Morphology

### (a) Factors Affecting the Measurement and Variability of Thermal Groove Widths

Variability in the thermal groove widths and profile shapes is characteristic of all four materials studied, for both faceted and smooth surfaces. Complex profiles occur from a combination of the faceting and grooving processes. For these geometries, the thermal groove width and profile are usually clearly defined by the positions of the facet peaks in the adjacent thermal groove humps, see Figures 15a and 16a. In another example, the geometry observed in the SEM (Figure 17a) is confirmed by using interferometry (Figure 17b). The interferogram shows that the humps associated with the thermal grooving process are distorted and asymmetric relative to the boundary. These features correspond to the groove profile found on the SEM micrograph, i.e., the facet peaks coincide with the thermal groove maxima. A schematic representation of this profile and Mullins' profile for thermal grooving by surface diffusion with isotropic surface energy is depicted in Figure 17c.

Occasionally the profile shape is such that it is unclear what to assign for the groove width, i.e., the maxima (facet peaks) on one or both of the humps are not obvious or non-existent. For example, a broad range rather than a single value (or narrow range) for the thermal groove width is assigned to the boundary designated in Figure 15a. The minimum groove width in this range underestimates and the maximum overestimates a groove width associated with an ideal profile (based on conservation of volume). This range was compared to all other grooves on this sample; the extremes in the assignable widths were within

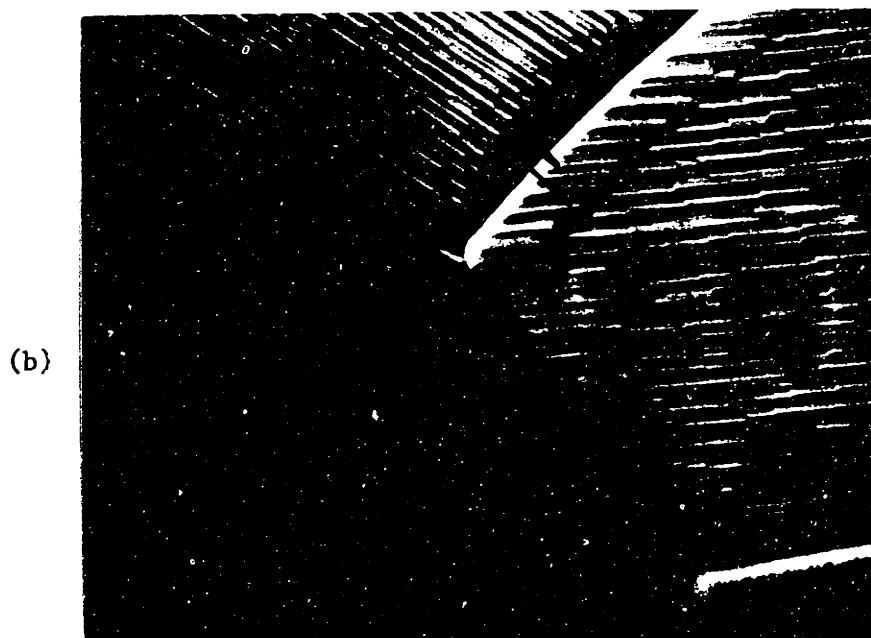
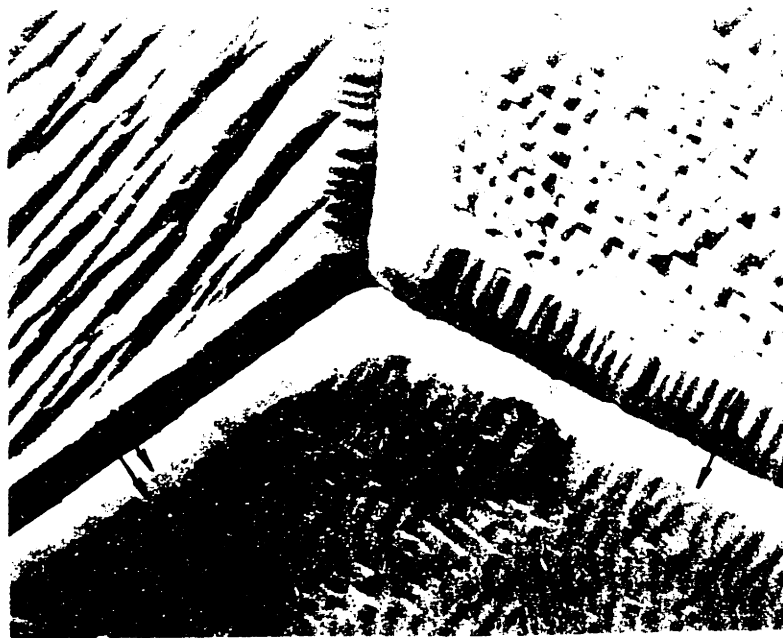
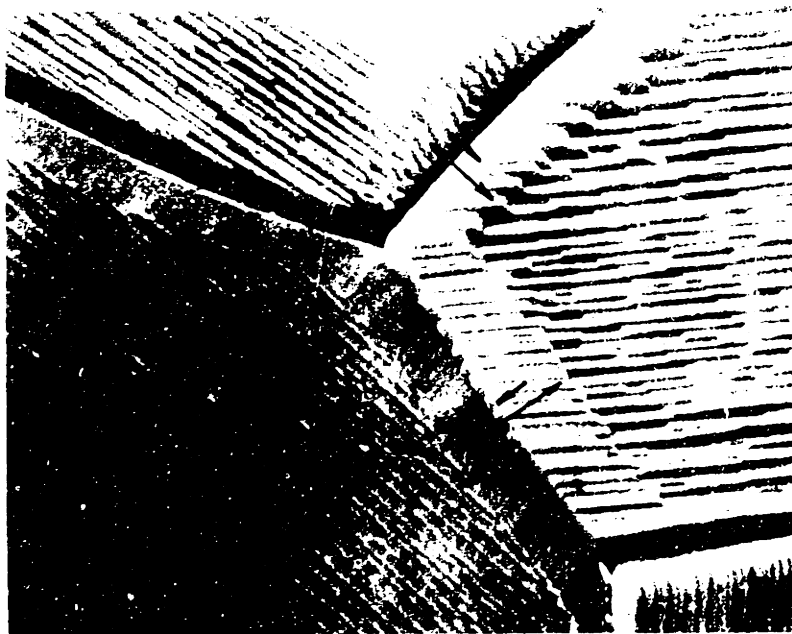


Figure 15 - Typical surfaces of LTVA samples where no MgO was added to the embedding powder. Higher magnification of Figure 26 (GBG11, 1296°C, 300 hours, 30° tilt) bar=1.0 $\mu$ m.



(a)



(b)

Figure 15 - Typical surfaces of EVA samples where no ZnO was added to the embedding powder. Higher magnification of Figure 26 (GB011, 1296°C, 300 hours, 30 - 4110 bar) 1.0 $\mu$ m.

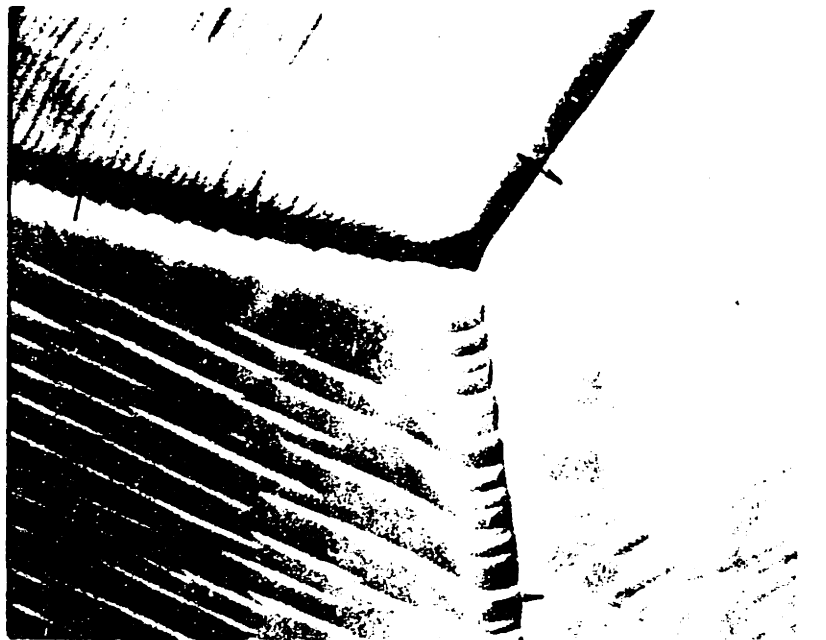


Figure 16 - typical surfaces of LTA samples with MgO added to the embedding powder. Higher magnification of Figure 27 (a) 30° tilt, (b) 60° tilt. bar = 1.0  $\mu$ m.

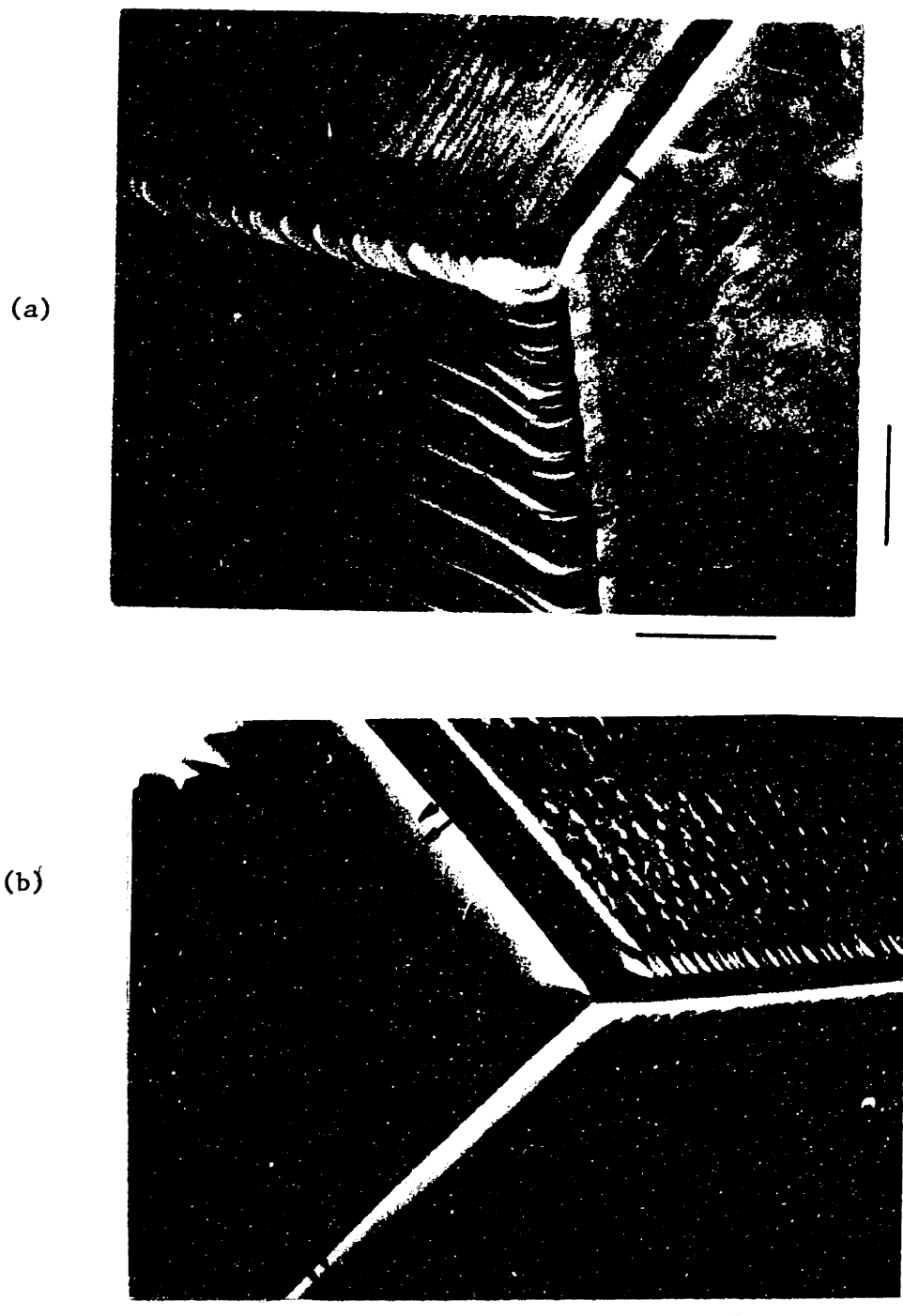


Figure 16 - Typical surfaces of LTVA samples with MgO added to the embedding powder. Higher magnification of Figure 27 (GBG12, 1306°C, 111 hours, (a) 30° tilt, (b) 60° tilt) bar = 1.0  $\mu\text{m}$ .



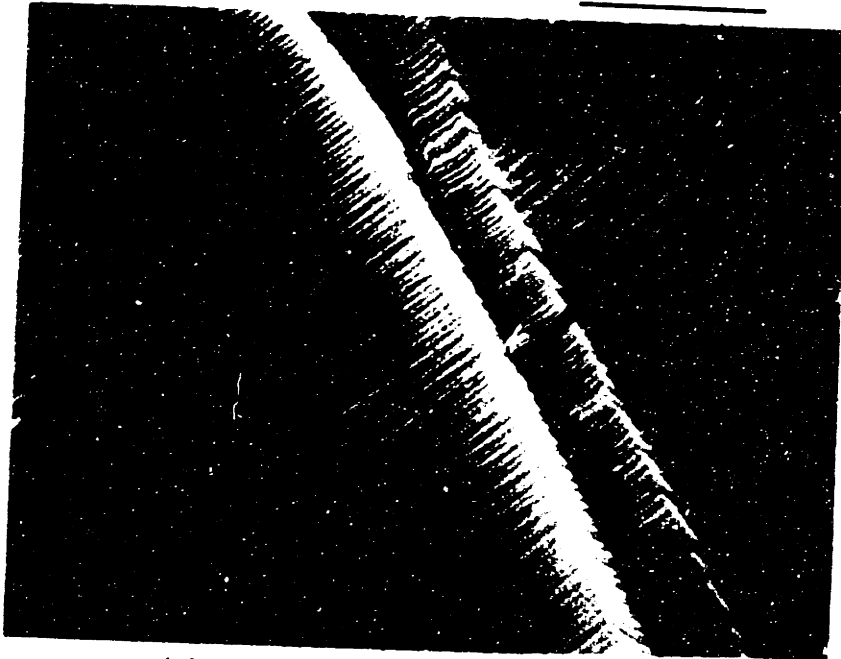


Figure 17(a) - Thermal groove 2C from an ADL sample from which time dependent grooving measured. (GBG29F, 1603°C, 283 hours, 45° tilt) bar = 5.0  $\mu\text{m}$ .

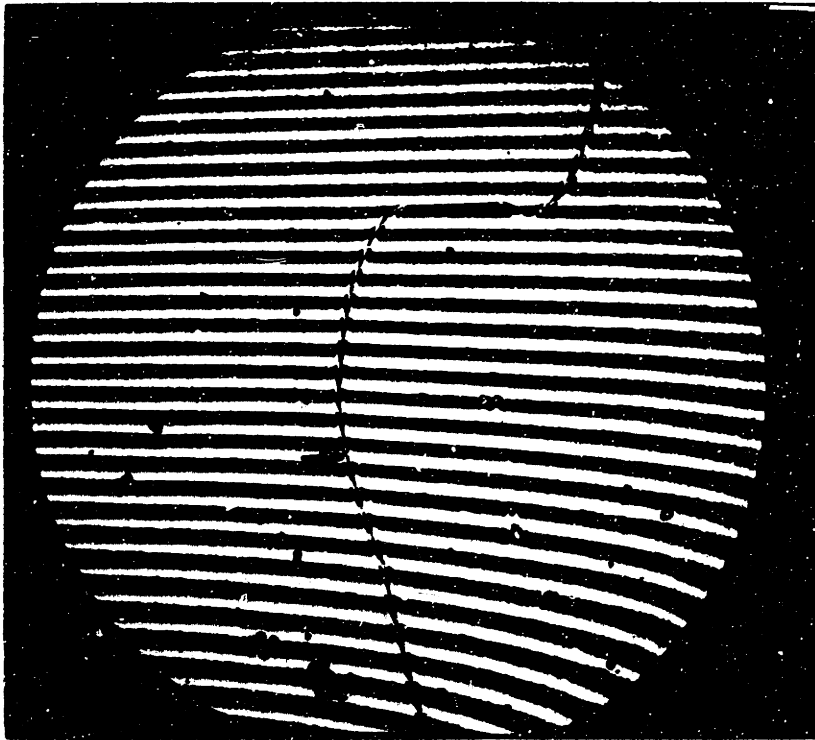


Figure 17(b) - Interferogram of same area in (a), denoted by arrow, bar = 25  $\mu\text{m}$ .

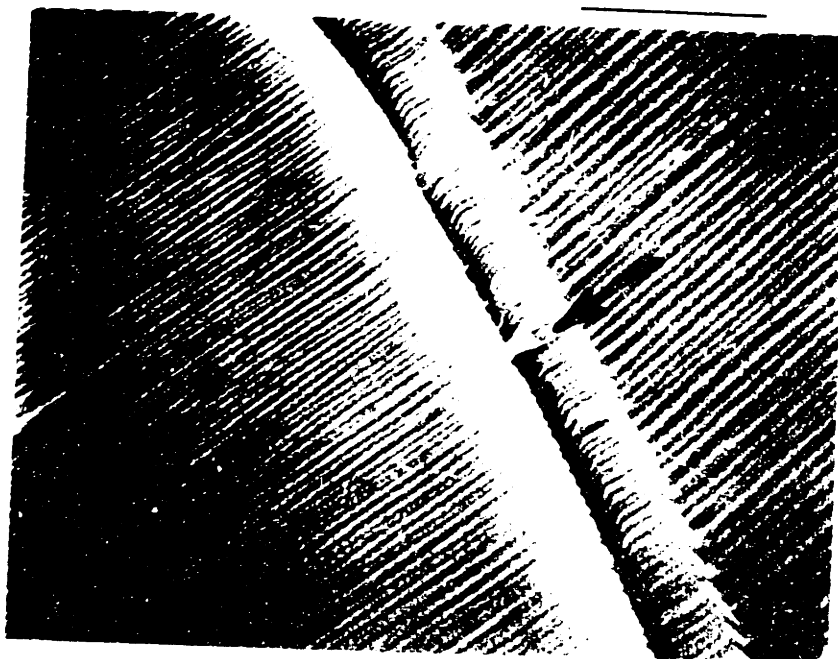


Figure 17(a) - Thermal groove 2C from an ADL sample from which time dependent grooving measured. (GBG29F, 1603°C, 283 hours, 45° tilt) bar = 5.0  $\mu\text{m}$ .

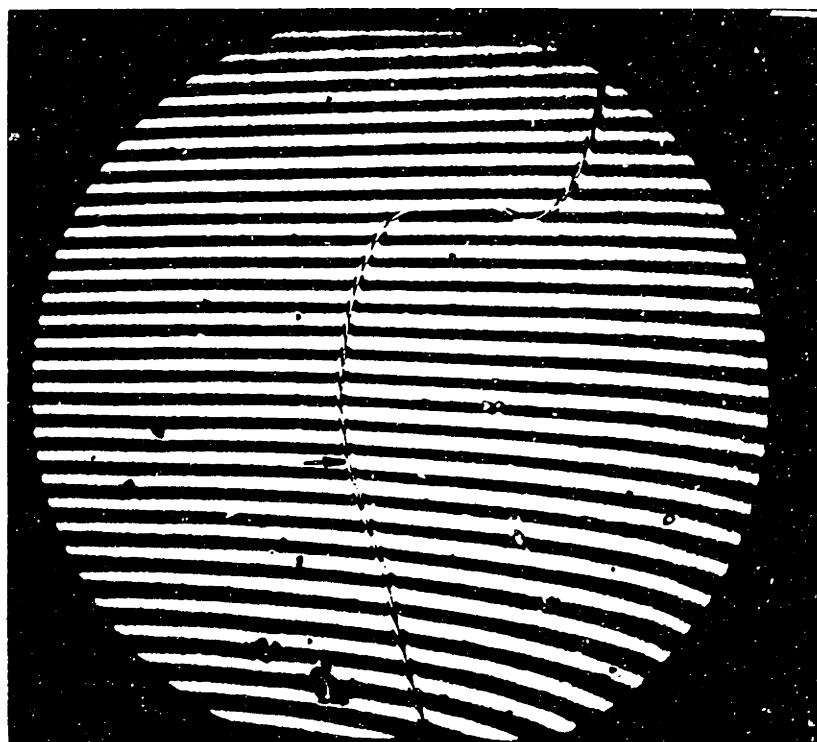


Figure 17(b) - Interferogram of same area in (a), denoted by arrow, bar = 25  $\mu\text{m}$ .

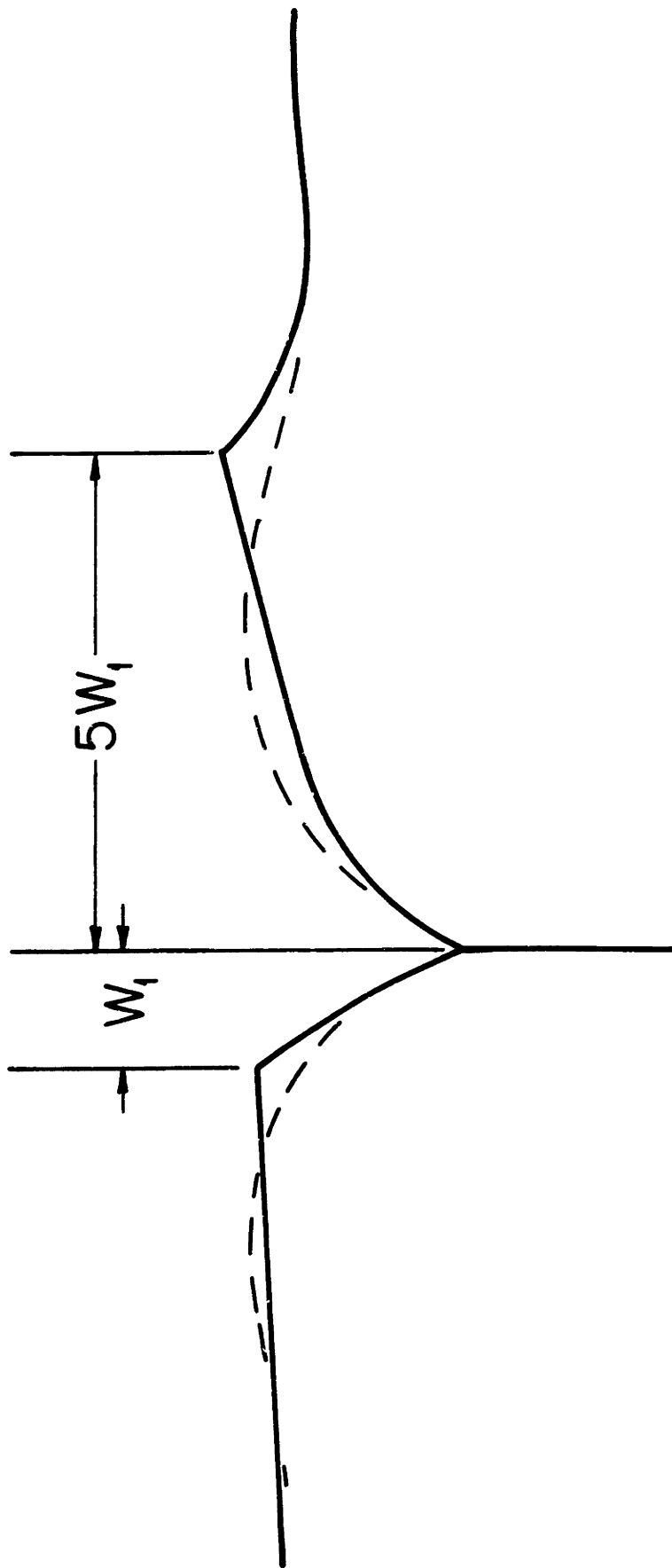


Figure 17(c) Schematic representation of a faceted thermal groove as compared to an isotropic profile.

the range of widths determined from "better defined" profiles.

An example of the extremes in groove width is shown in Figure 18a. The width for boundary 1 is near the limit of resolution, whereas boundary 2, although asymmetric, is much wider. Many boundaries with widths between these extremes are shown in Figure 18b. These examples illustrate the variability in widths which can result from faceting.

Uncertainty in the thermal groove width may also arise from the lack of contrast from smooth surfaces using the SEM, as in Figure 16a. This uncertainty may be reduced by increasing the specimen tilt.\* Unfortunately, these groove widths are below the detection limit for optical microscopy, so a comparison of the techniques cannot be made in these cases.

Changes in the groove width along a curved segment of a boundary are also exhibited in Figure 17a. This feature was commonly found on ADL specimens where the boundaries are characterized by many curves and facets along a length of several hundred microns. The occurrence is less frequently observed on other materials primarily because the grain sizes are smaller. One example on the LTVA material is shown for a segmented boundary, pinned by a pore, in Figure 19. The effects of impurities and changes in the boundary inclination angle with respect to the surface are also important, but could not be documented in detail.

Variable thermal grooving rates and profiles shapes were also found on LD samples which did not develop extensive faceting, e.g., Figure 20a and b. These samples were from the series used for measuring

---

\*

Increasing the specimen tilt in the SEM increases the contrast from nearly smooth surfaces but relocation of the same boundary after such an operation is difficult.

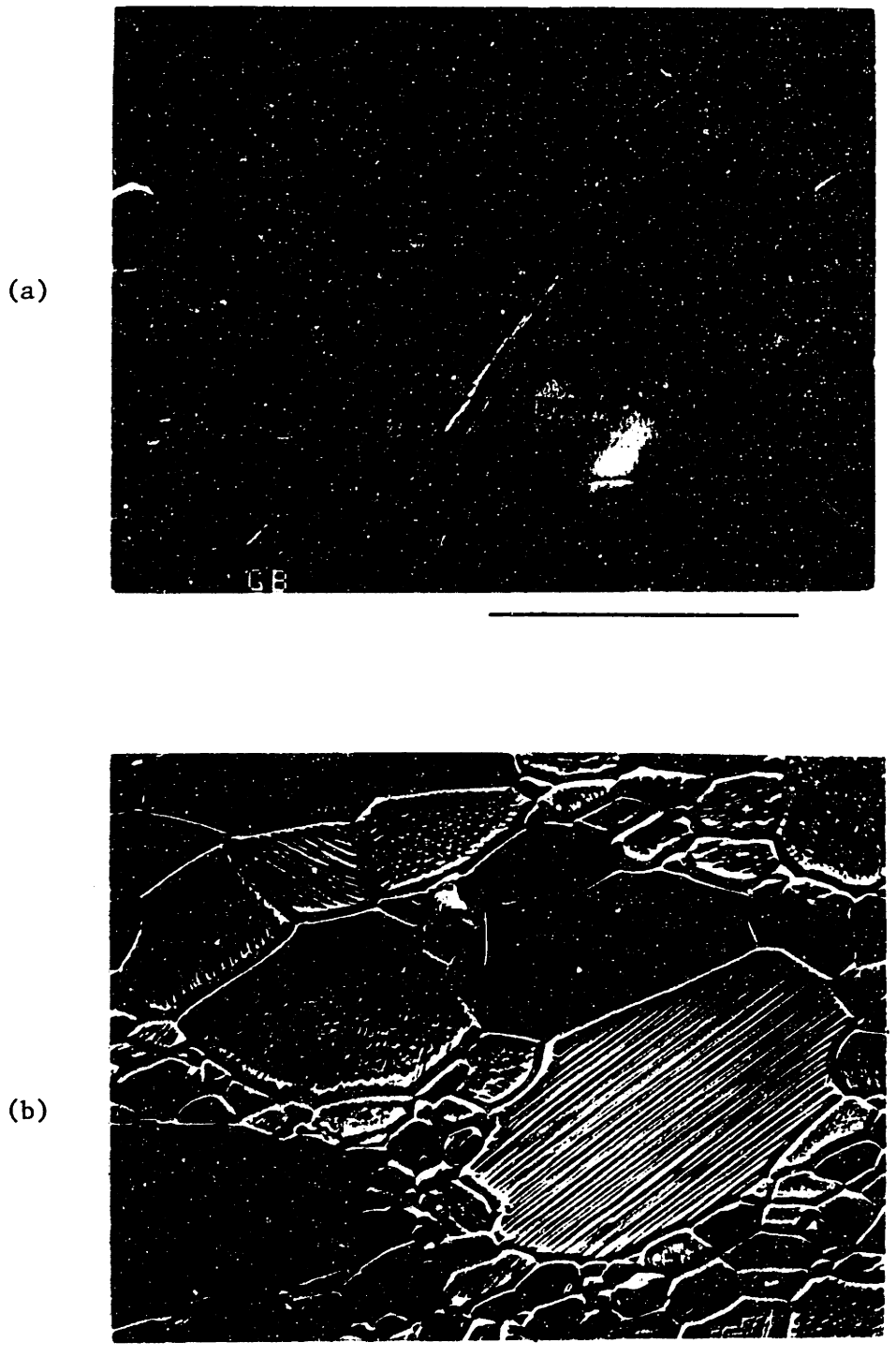


Figure 18 - Thermal grooving on the RHP samples, boundaries 1 and 2 show extremes in observed widths. (GBG15, 1247°C, 394 hours, 60° tilt) bar = 5  $\mu$ m.

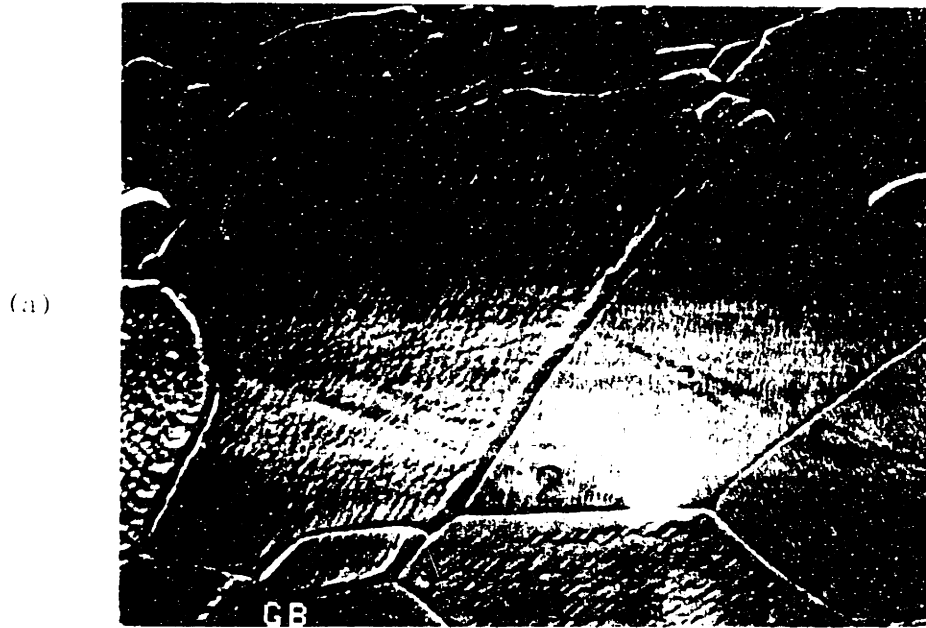


Figure 18 - Thermal grooving on the RHP samples, boundaries 1 and 2 show extremes in observed widths. (GBG15, 1247°C, 394 hours, 60° tilt) bar = 5  $\mu$ m.

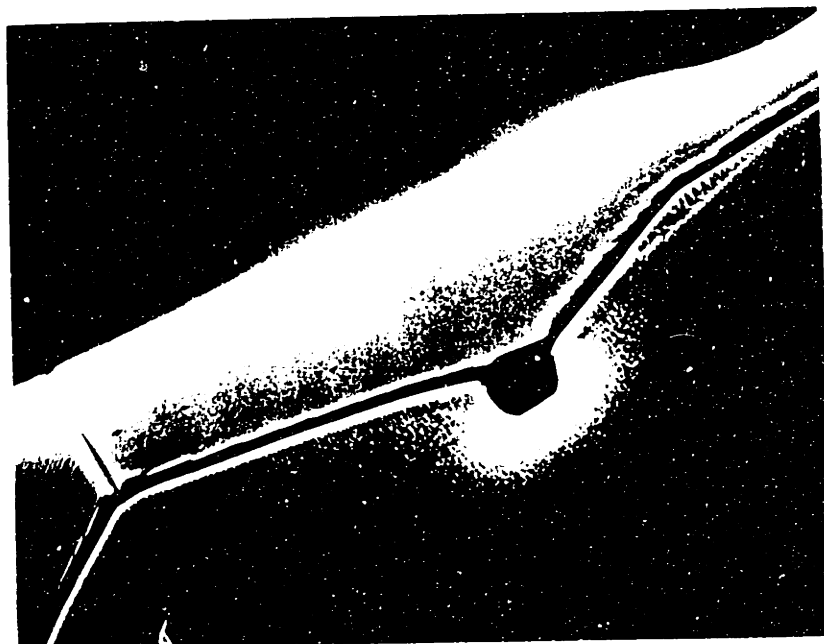


Figure 19 - Surface of an LTA sample with a faceted grain boundary pinned by a pore. (GBG16, 1485°C, 87 hours, 60° tilt) bar = 10 μm.

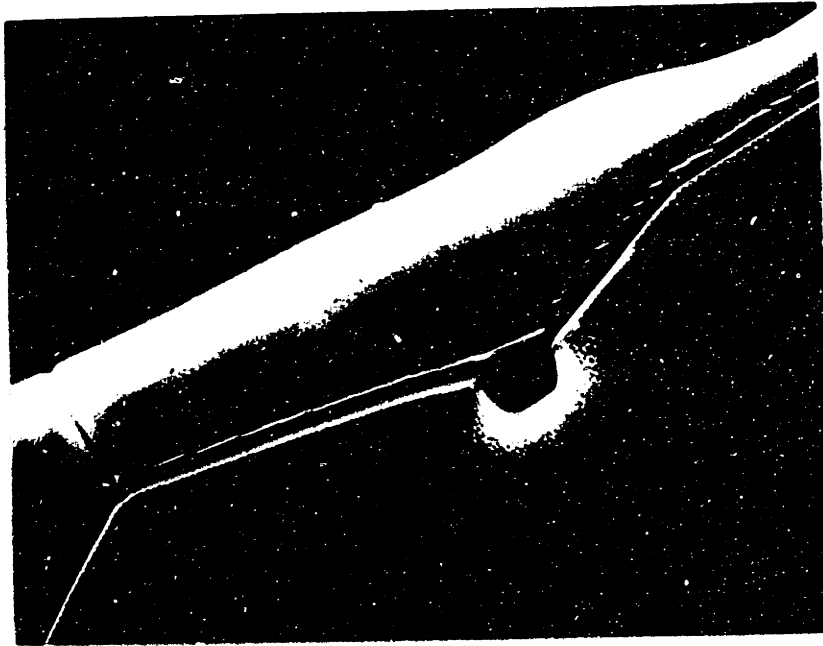


Figure 19 - Surface of an LTVA sample with a faceted grain boundary pinned by a pore. (GBG16, 1485°C, 87 hours, 60° tilt) bar = 10  $\mu\text{m}$ .



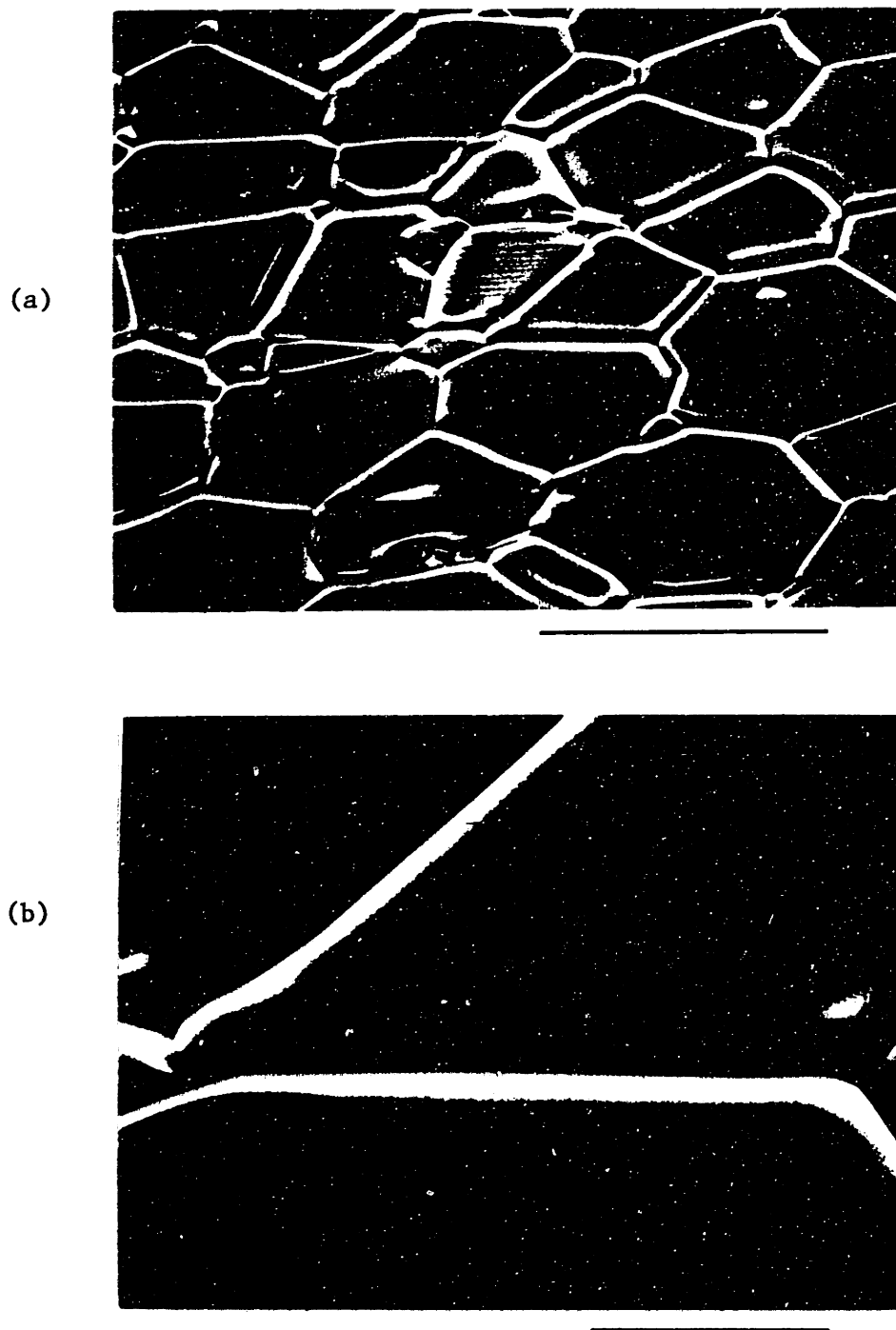


Figure 20 - Representative surface of an LD specimen on which time dependent grooving studied. (GBG27, 1602°C, 291 hours, 60° tilt) (a) bar = 50  $\mu\text{m}$ ; (b) bar = 10  $\mu\text{m}$ .

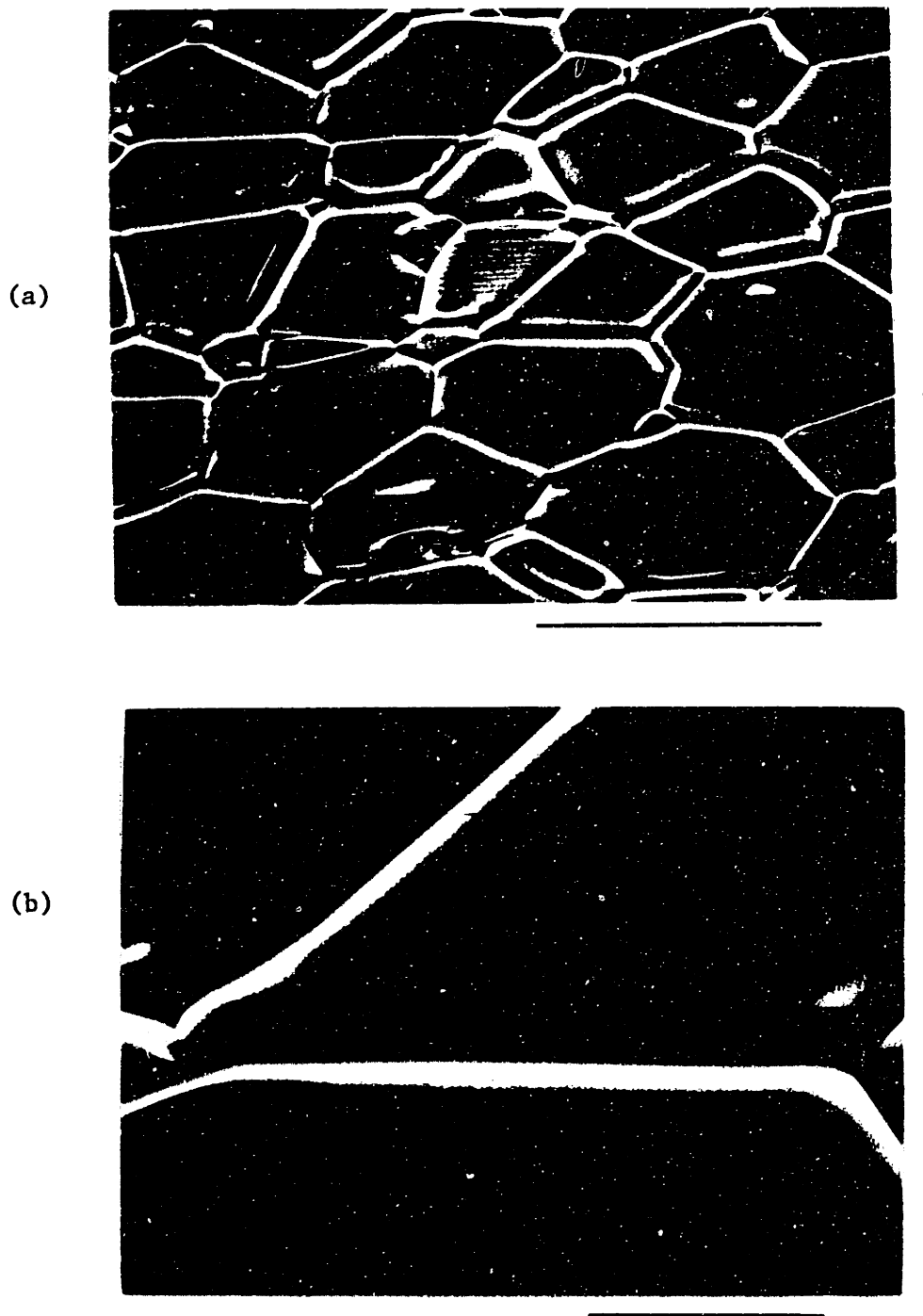


Figure 20 - Representative surface of an LD specimen on which time dependent grooving studied. (GBG27, 1602°C, 291 hours, 60° tilt) (a) bar = 50  $\mu\text{m}$ ; (b) bar = 10  $\mu\text{m}$ .

the time dependence of thermal grooving. A sequence of interference micrographs following the progression of the thermal grooving process of ten specific boundaries is shown in Figure 21. The numbers adjacent to the boundaries are labels which correspond to those in Table IV. These grain boundaries remained stationary during annealing; others have migrated. Unexpected height differences between adjacent grains and some thermal grooves lacking a hump on one side of the boundary have also developed.

The variable grooving rates on the LD specimens are important; they indicate that faceting is not the sole cause of the variability in groove widths, and that the difference in thermal grooving rates is greater than 2x. A notable example of the difference is shown by boundaries numbers 3 and 4 in Figure 21. Both boundaries exist at the first observation time (B in Table IV) and remain stationary throughout the experiment.

#### (b) Observations on Faceting

The development of faceting depends on the temperature of the experiment and on the impurity level in the samples. Faceting was observed in all experiments using the pure materials. For the Lucalox materials, different behaviors were observed, depending on the experimental conditions. These conditions are divided into three classes: (a)  $\text{Al}_2\text{O}_3$  embedding powder with MgO additions, (b) undoped embedding powder, and (c) freely evaporating samples. Pure materials were always embedded in a pure powder. Although different  $\text{Al}_2\text{O}_3$  powders were used for embedding in experiments, apparently the chemical differences among them are small and do not influence the results.

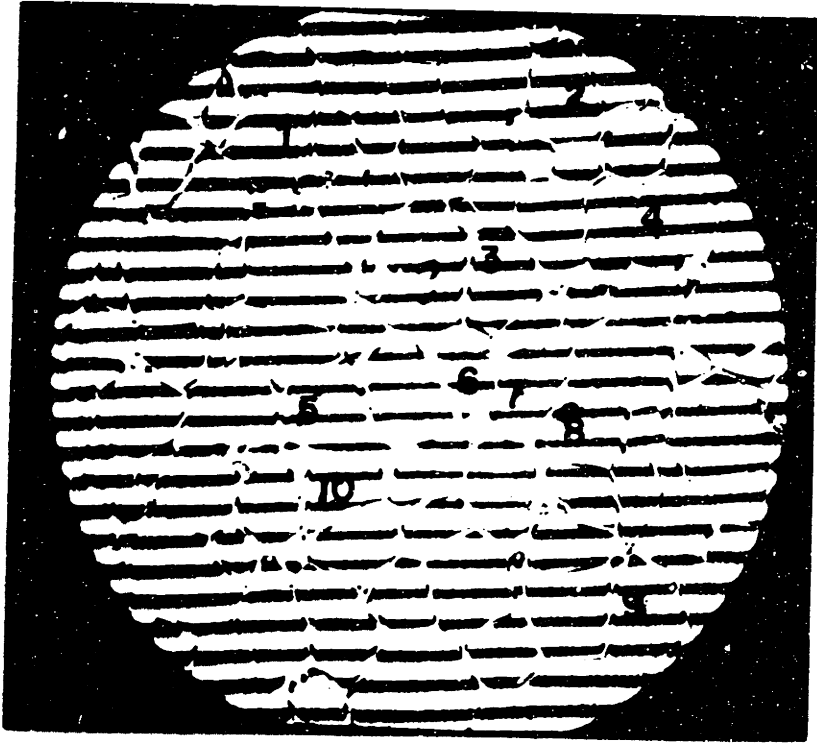
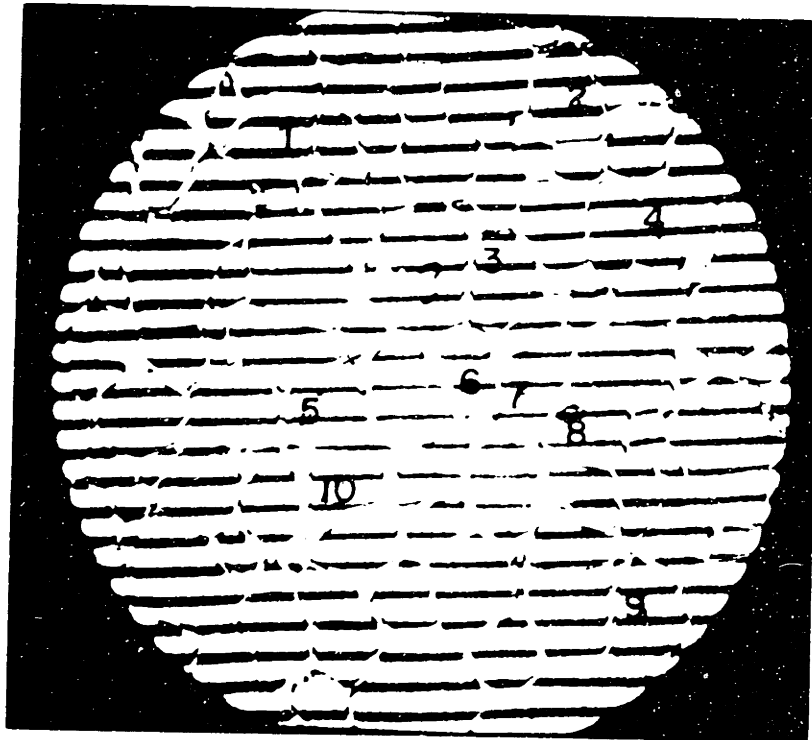


Figure 21(a) Sequence of interferograms on which time dependent grooving measured (GBG27, LD, 1602°C), (a) 10 hours, (b) 30 hours, (c) 62 hours, (d) 103 hours, (e) 291 hours, bar = 25  $\mu\text{m}$ .



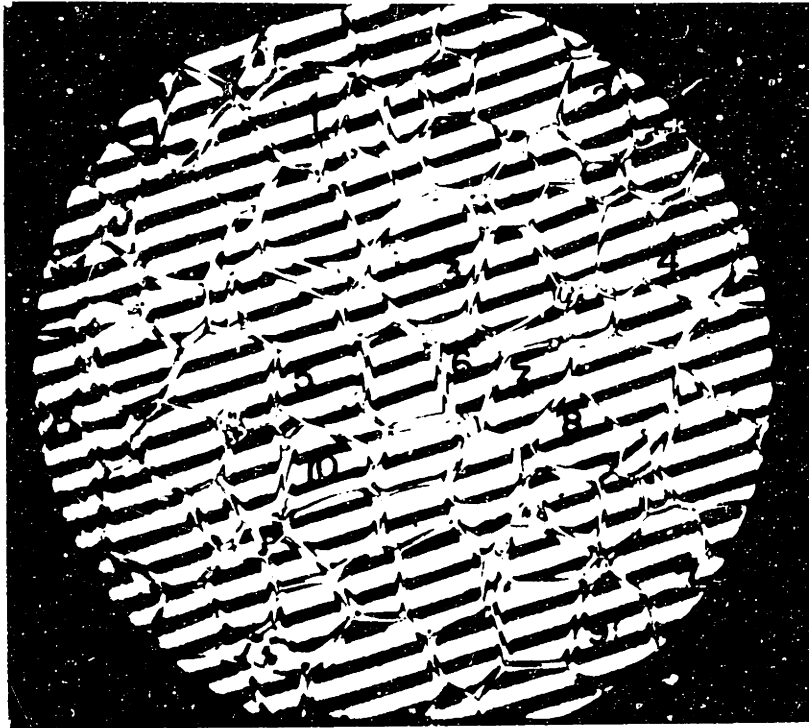


Figure 21(b) - (GBG27, 30 hours), bar = 25  $\mu\text{m}$ .

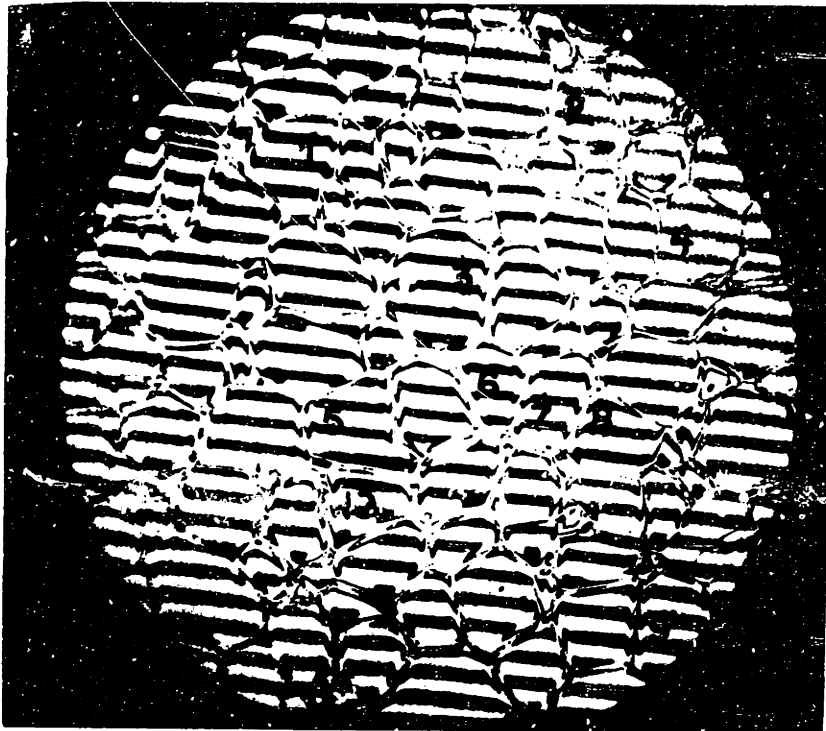


Figure 21(c) - (GB27, 62 hours), bar = 25  $\mu\text{m}$ .

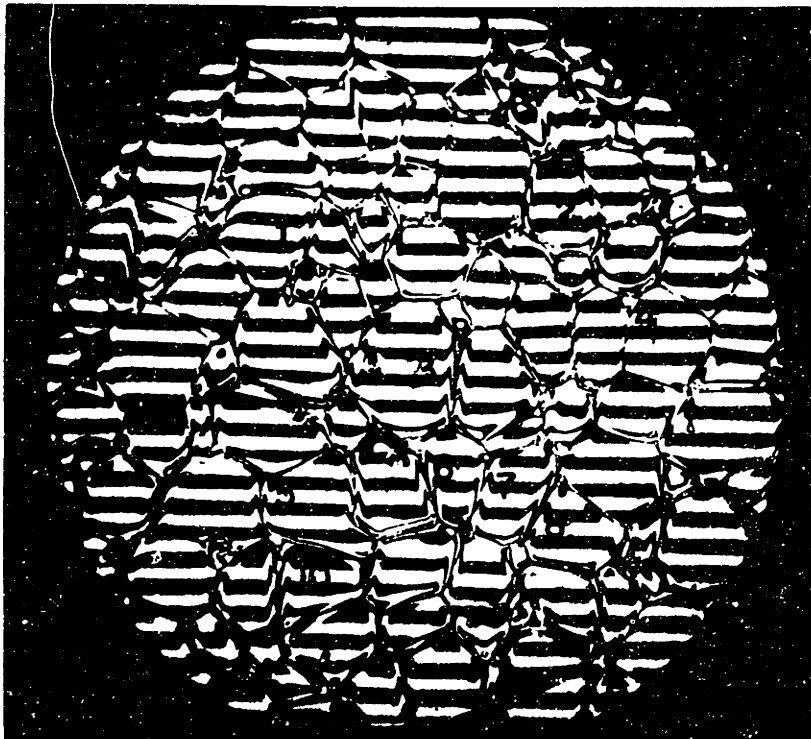


Figure 21(d) - (GBG27, 103 hours), bar = 25  $\mu\text{m}$ .

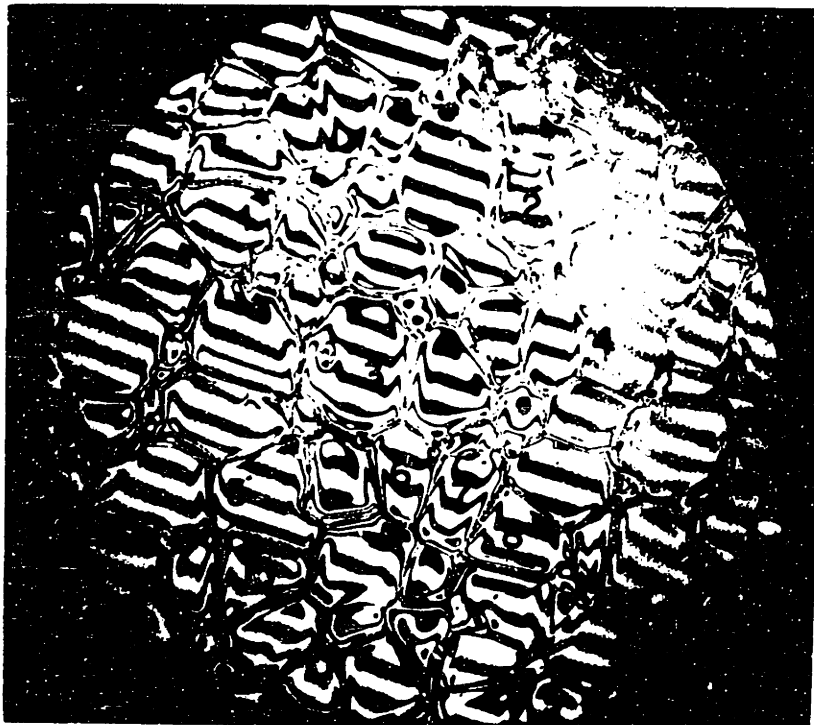


Figure 21(e) - (GBG27, 291 hours), bar 25  $\mu\text{m}$ .

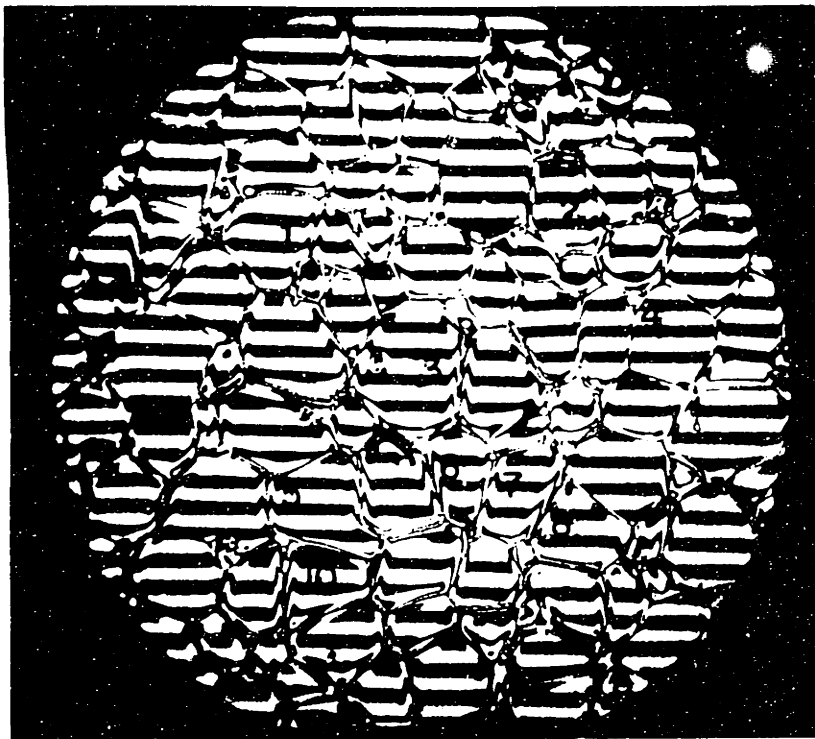


Figure 21(d) - (GBG27, 103 hours), bar = 25  $\mu$ m.

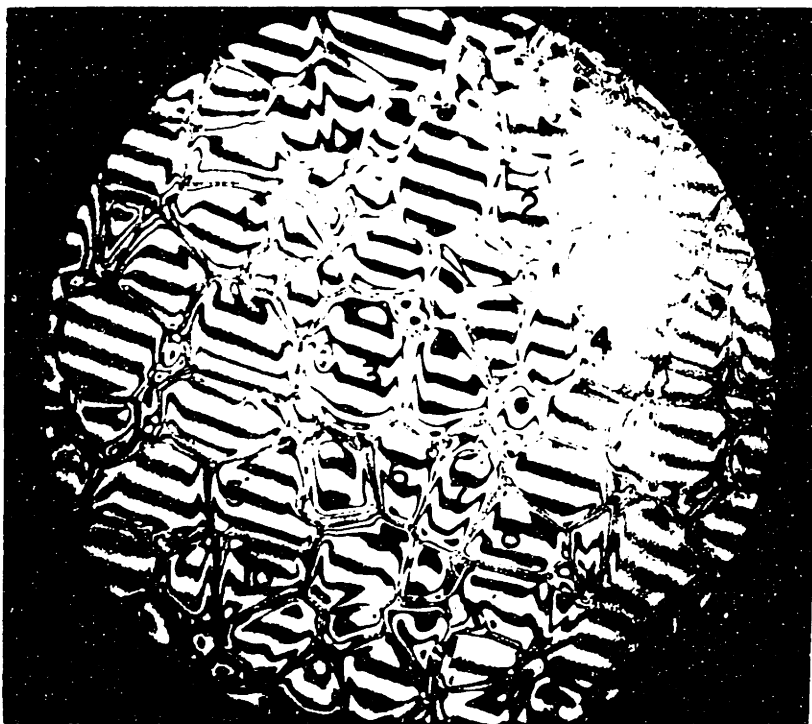


Figure 21(e) - (GBG27, 291 hours), bar = 25  $\mu$ m.



Where MgO has been added to the  $Al_2O_3$  embedding powder, the occurrence and degree of faceting on the Lucalox materials decreases as temperature is increased; however, other impurities remain an important factor in these observations. For the LD material, surfaces were mostly smooth with only a few linear facets on samples annealed at the higher experimental temperatures, 1842°C for 39 minutes (GBG 26) and 1602°C for 291 hours (GBG27), Figure 20. The only other successful experiment involving this material produced samples where second phases were precipitated at the free surfaces, at a relatively low temperature of 1092°C for 1163 hours (GBG24), Figure 14. Surfaces with developing facets and areas with similar second phase precipitates were noted on the other "as-received" Lucalox material, LTAR. These experiments were conducted at relatively low temperatures, 1192°C for 20 days (GBG22) and 950°C for up to 229 days (GBG18). At higher temperatures, 1456°C for 286 hours (GBG17) and 1394°C for 2667 hours (GBG19), the LTAR material exhibited a range of faceting types, see Figure 22. The choppy facets were less frequent on samples treated at the higher of the two temperatures; however, this observation is also consistent with the shorter annealing time and smaller average groove width for these samples. For the cleanest Lucalox material, LTVA, the entire range of facet types and smooth surfaces were found on all samples, with and without MgO-doped embedding powder.

Faceting on the pure samples was more extreme although there are fewer observations with respect to the temperature dependence. For the RHP samples heat-treated at the relatively low temperatures of 1247°C for 394 hours (GBG15) and for ADL samples annealed at 1602°C for 283 hours (GBG29), coarse faceting resulted, Figures 18 and 23, respectively. The

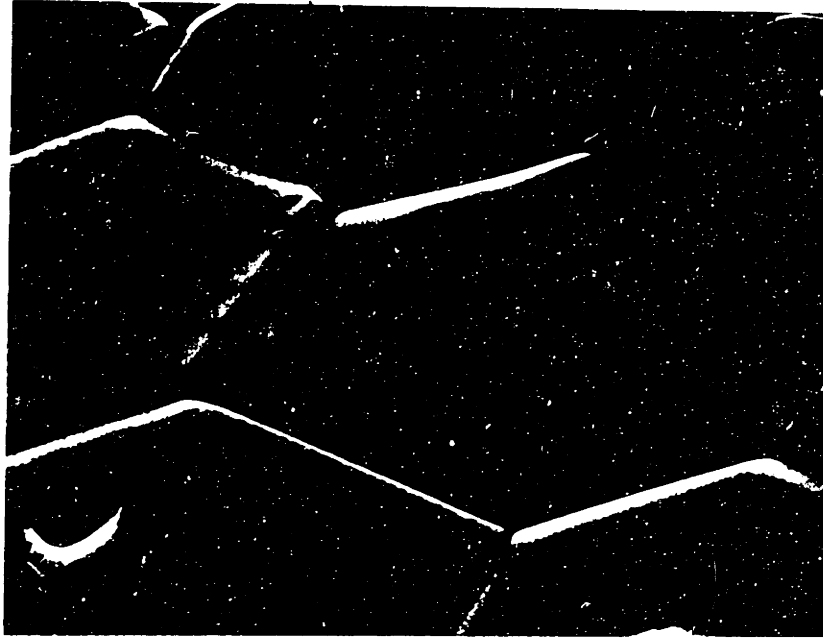


Figure 22 - Thermal grooving on an I. le  
(GBG17, 1456°C, 286 hours, 60° tilt) 5 μm.



Figure 22 - Thermal grooving on an LTAR sample  
(GBG17, 1456°C, 286 hours, 60° tilt) bar = 5  $\mu$ m.

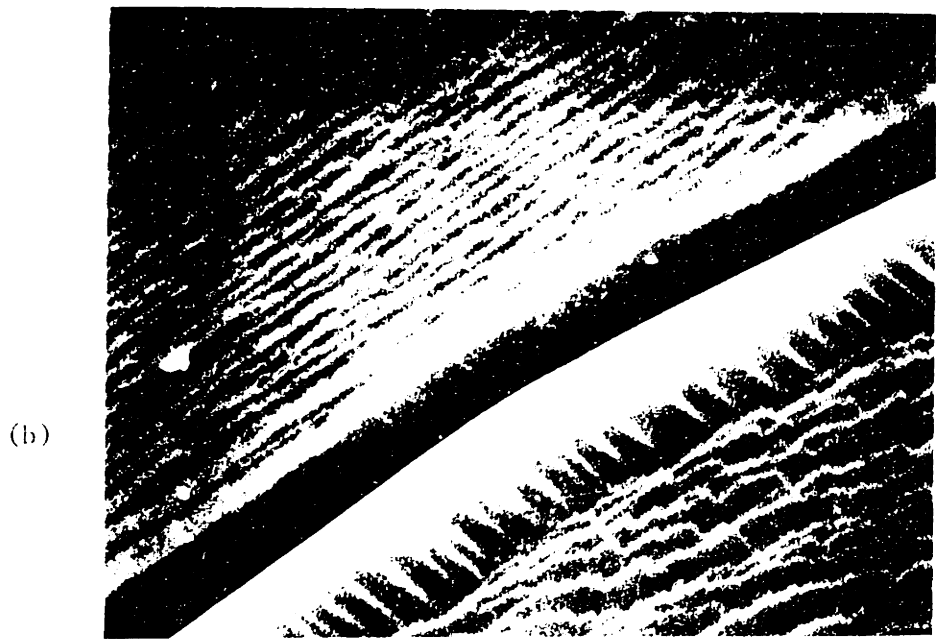
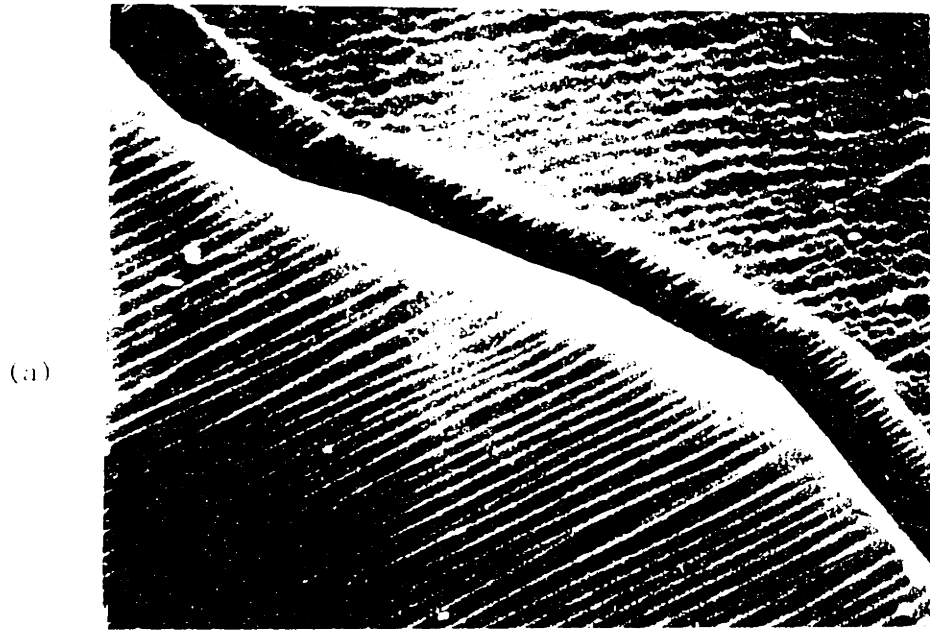


Figure 23 - Thermal grooving on an ADL sample (GBC29, 160°C, 283 hours, 45° tilt) bar = 5  $\mu$ m.

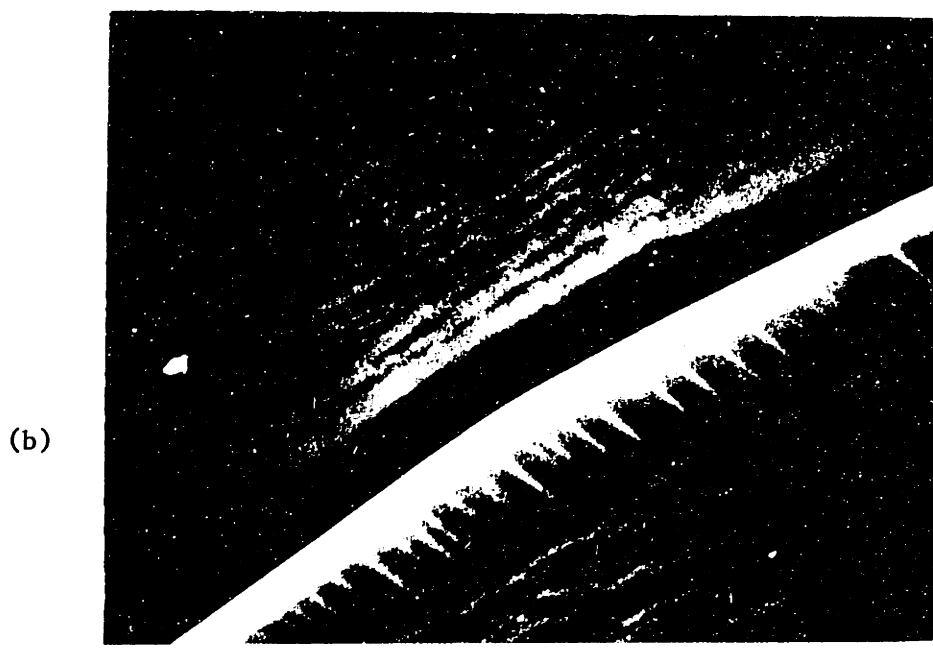
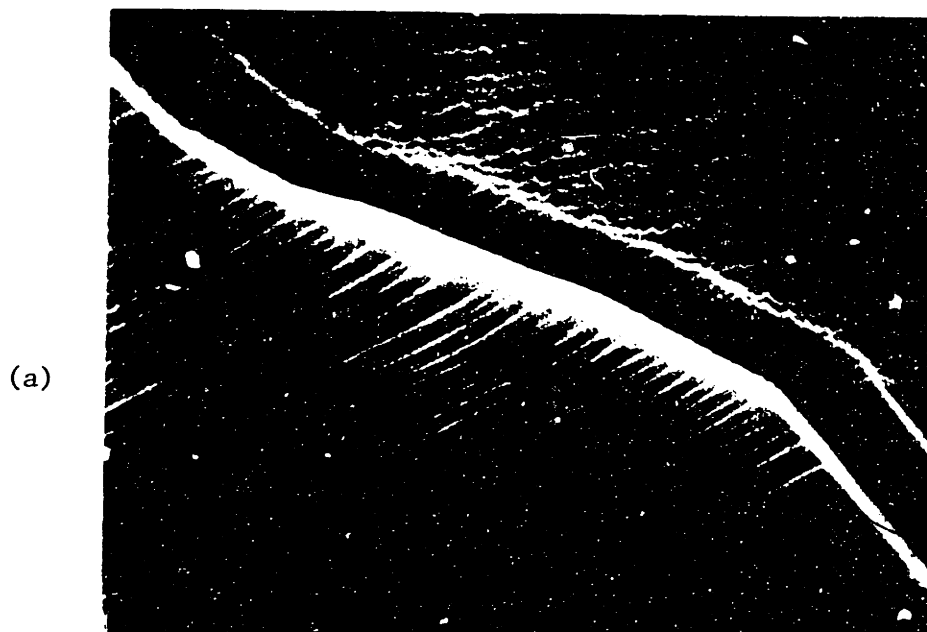


Figure 23 - Thermal grooving on an ADL sample (GBG29, 1603°C, 283 hours, 45° tilt) bar = 5  $\mu$ m.

conditions for the ADL specimens are comparable to a similar experiment on the LD material (GBG27) reported above. By comparison of these two observations, faceting apparently depends either on the level of surface impurities either segregating from pre-existent levels in the bulk or boundary phases of the material or on a specific orientation that the ADL samples exposed. Similar packing powders were used in both experiments, thus vapor transport of impurities from the powders is not the cause. A lesser degree of faceting was observed on BK samples annealed at 1602°C for 1 hour (GBG28) due in part to the shorter heat-treatment, see Figure 24. The BK samples annealed at 1840°C for 6 hours (GBG31) are characterized by the presence of many grains with linear facets and a considerable amount of grain boundary migration and grain growth. The groove profiles and the grain surfaces of the ADL specimens (GBG30), annealed under these same conditions, also developed facets. A detailed comparison of the degree of faceting on this specimen with that of samples annealed at lower temperature (GBG29) could not be made due to the poor resolution of the facets using optical microscopy.

For the MgO-doped ADL samples, the morphology of some grains is different than that of the undoped specimens. It is not known whether this is a result of variable grain structures along the length of the ADL sapphire tubes, due to the prolonged annealing, or caused by an impurity effect such as diffusion induced grain boundary migration. The thermal groove widths were measured on the few boundaries between grains that resembled those found on undoped ADL samples in a similar experiment (GBG29). For these boundaries the groove profiles indicated faceting similar to that in the undoped ADL samples. There were some isolated

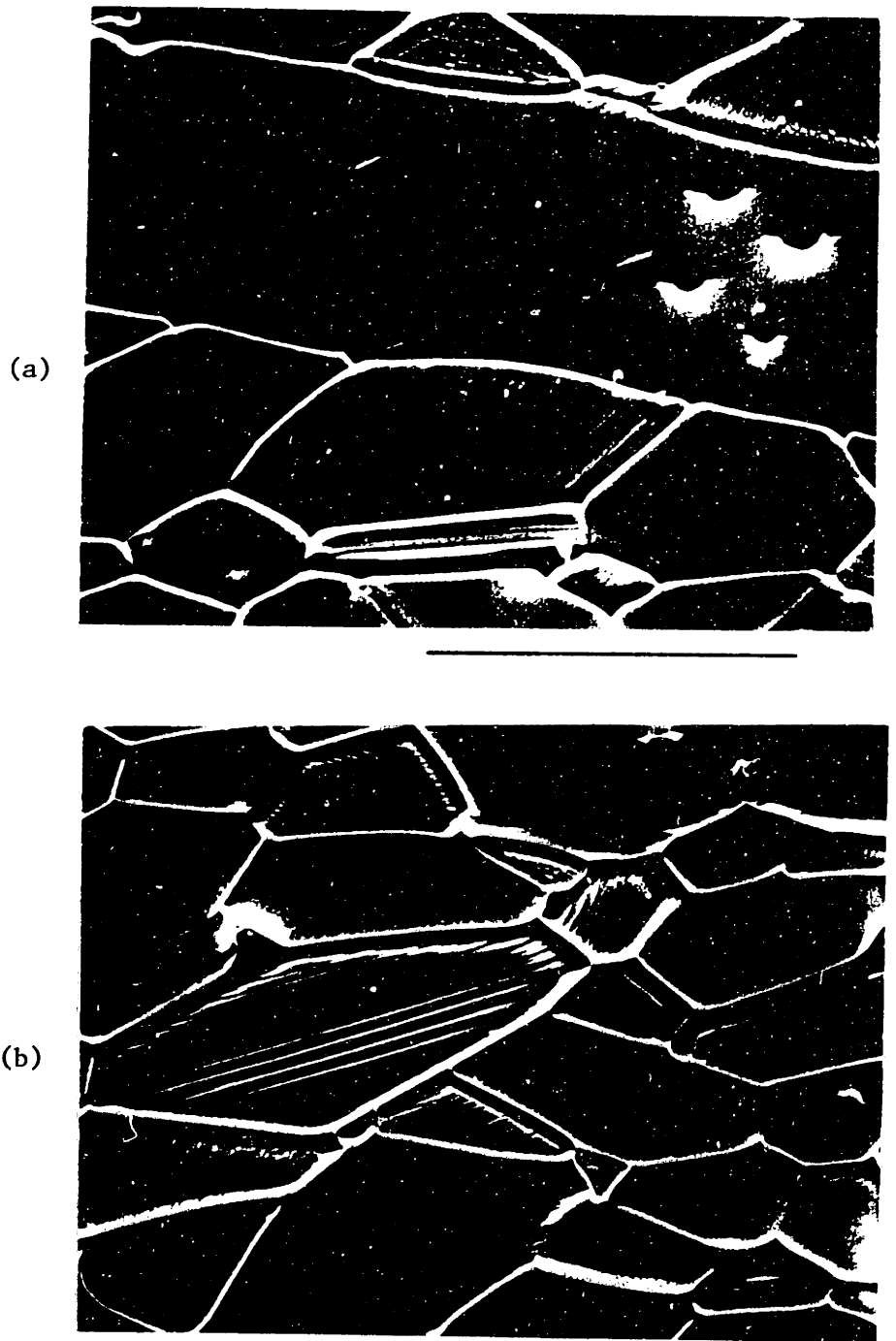


Figure 24 - Typical microstructure of a BK sample (GBG28, CR1, 1602°C, 1 hour, 60° tilt) bar = 10  $\mu$ m.

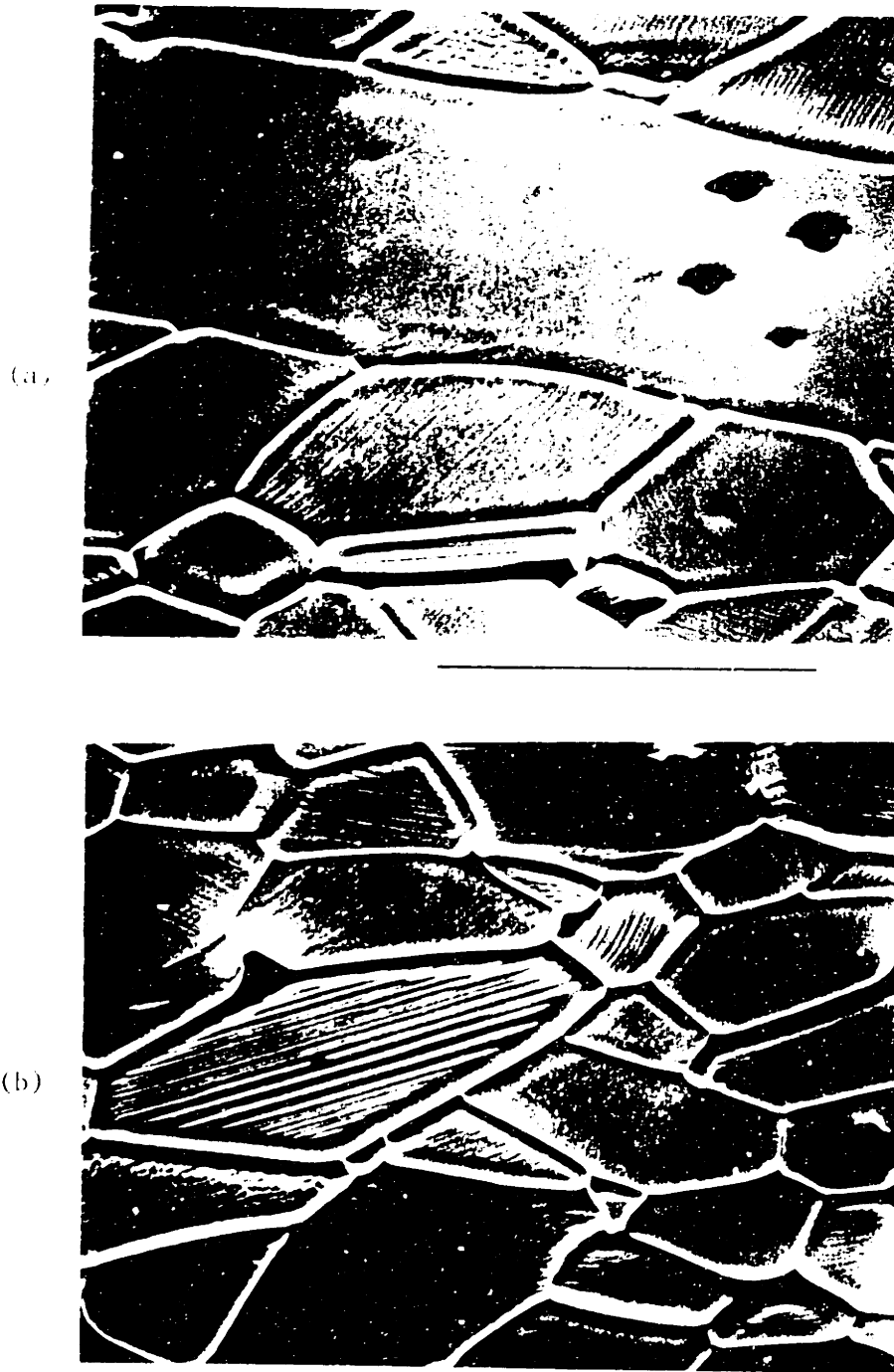


Figure 24 - Typical microstructure of a BK sample (GBG28, CR1, 1602°C, 1 hour, 60° tilt) bar = 10  $\mu$ m.



grains, or fine grain patches for which the boundary grooves had abnormal profiles and small widths, possibly due to migration; these were not analyzed.

The degree to which surface faceting features develop on the LTVA material depends on whether the embedding powders have MgO concentrations above the solubility limit<sup>\*</sup>, pinning the Mg-activity. Hillocks<sup>\*\*</sup>, as in Figure 25, and brightness-darkness contrast from grain-to-grain, as in Figure 26, are characteristic of samples annealed without MgO additions to the powder. The latter characteristic results from the variable orientation of the surface facets with respect to the secondary electron detector in the SEM. In a similar experiment using 0.5 w/o magnesia addition to the powder and shorter annealing time, the grain-to-grain contrast using the SEM is not evident, Figure 27. A comparative set of micrographs of these two experiments at higher magnification is presented in Figure 15 and 16. A "smoother" appearance is found on the sample where the embedding powder contained magnesia addition; likewise, hillocks were not observed on any specimens with magnesia added to the powder. All of these LTVA samples were boiled in aqua regia (wash 2) which dissolves  $\text{MgAl}_2\text{O}_4$ ; therefore, surfaces may be depleted of magnesium

The surface resulting from a thermal grooving experiment with simultaneous free evaporation at  $1842^\circ\text{C}$  is shown in Figure 28. Only a few linear facets and mostly smooth surfaces have evolved. This is surprising because preferential loss of Mg and other impurities is expected.

---

\* The solubility limit is approximately 84 ppm cation fraction at  $1500^\circ\text{C}$  and decreases with decreasing temperature [Roy and Coble (1968)].

\*\* Hillocks refer to the mounds protruding above the faceted grain surfaces.

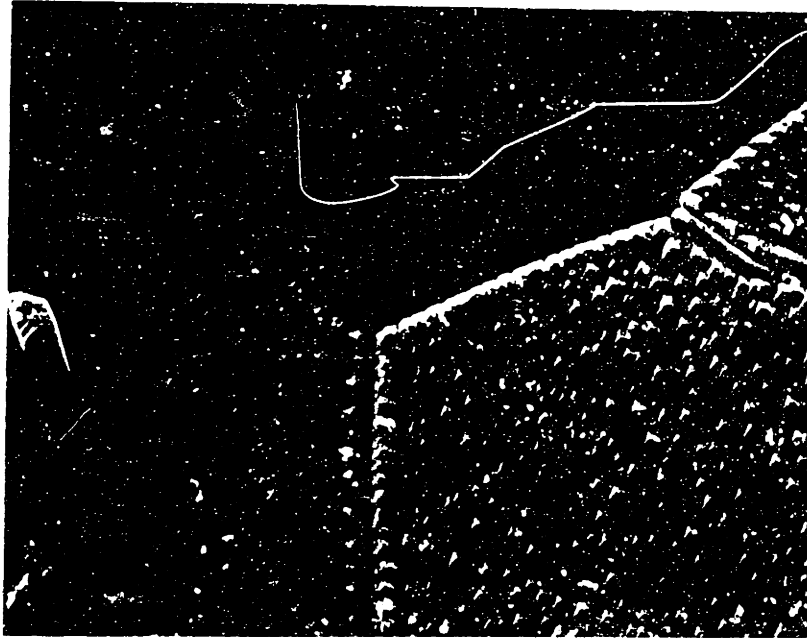


Figure 25 - Hillocks observed on a LTVA sample where no MgO was added to embedding powder (GBG6, 1250°C, 33 hours, 20° tilt) bar = 5  $\mu$ m.

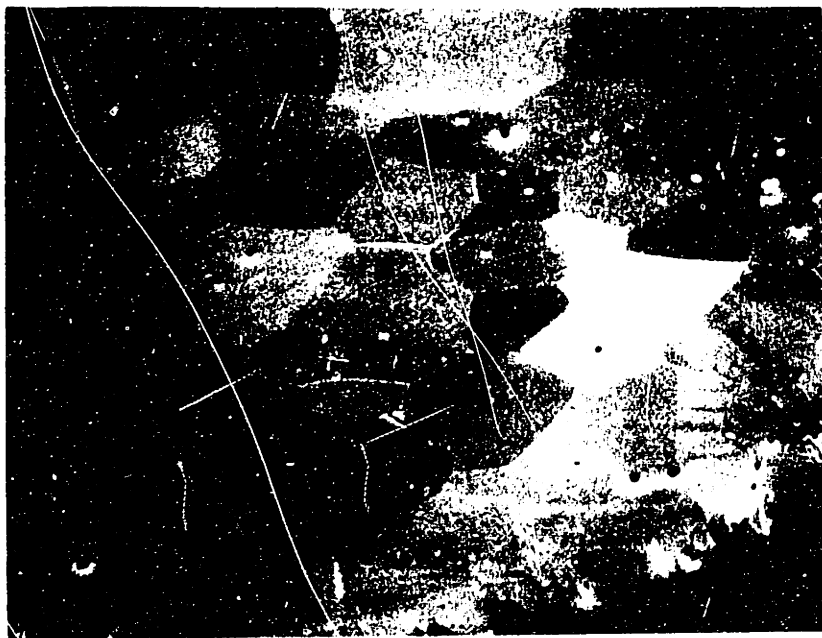


Figure 26 - Grain-to-grain contrast found on a LTVA sample where no MgO was added to the embedding powder (GBG11, 1296°C, 200 hours, 30° tilt) bar = 50  $\mu$ m.

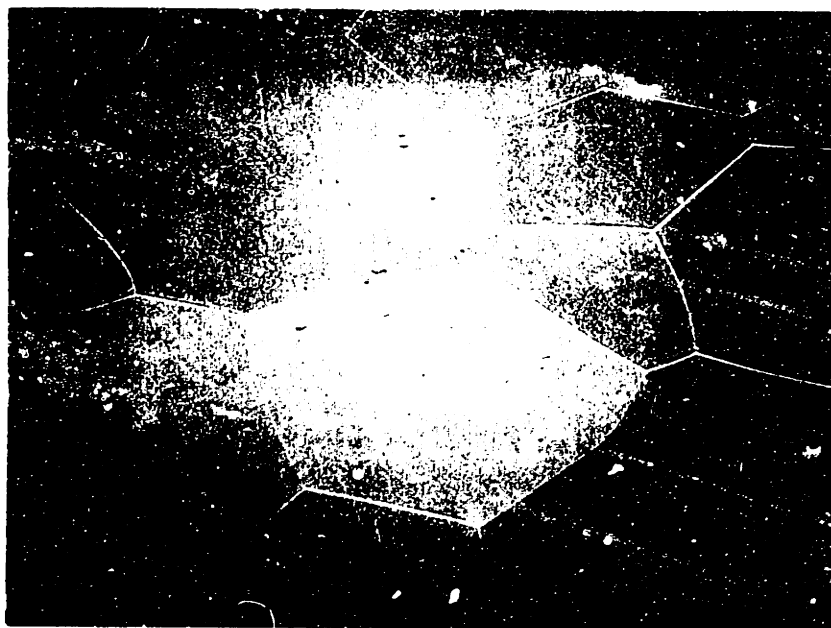


Figure 27 - Relatively smoother surface where MgO added to embedding powder, compare with Figure 26. (GBG12, 1306°C, 111 hours, 30° tilt) bar = 50  $\mu$ m.

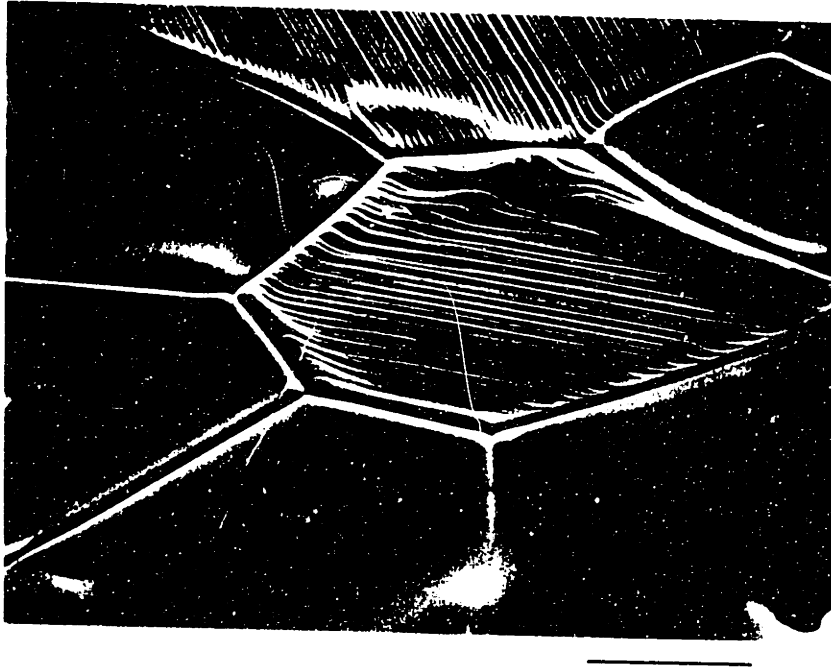


Figure 28(a) - Typical surface of a freely evaporating sample (GBG25, 1842°C, 40 min, 60° tilt) bar = 10  $\mu\text{m}$ .

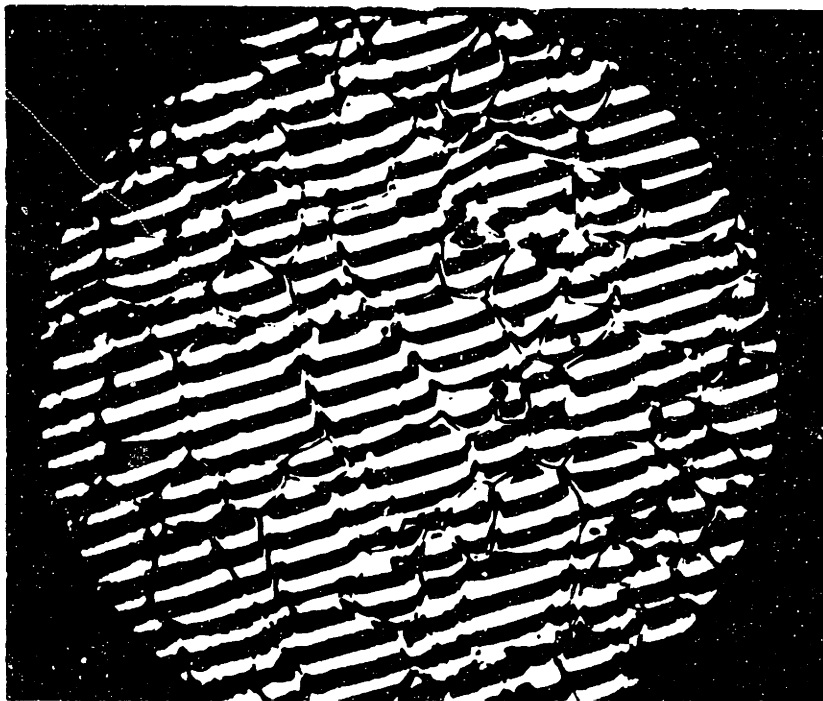


Figure 28(b) - Interferogram of the same sample as in (a). bar = 25  $\mu\text{m}$ .

(c) Simultaneous Free Evaporation

The thermal groove profiles for samples on which simultaneous free evaporation occurred are characterized by more mass in the humps than was transported in the "digging" of the groove, as shown in the interferograph in Figure 28b for sample GBG25. In some cases the groove root is above the plane of the grain faces<sup>\*</sup> on either side of the boundary, i.e., "raised" grain boundary grooves. Differential loss of material from the grain faces has apparently occurred resulting in height differences between adjacent grains. Considerable grain boundary migration has also occurred as indicated by the remnant boundary grooves. However, a comparative observation from a similar experiment without free evaporation (GBG26) could not be made since most of the surface was covered with a "tungsten oxide" contaminant. The widths on the few exposed thermal grooves on sample GBG26 are significantly larger than those characteristic of the freely evaporating sample. The appearance of raised thermal grooves is consistent with a simple evaporation process or a surface or lattice diffusion controlled process. This profile may denote a lowering of the evaporation rate by impurities that were transported to the free surfaces by boundary diffusion. Alternatively, increased concentrations of impurities near the grain boundary may affect the diffusion mechanisms.

B. Time Dependence

The variability in the thermal grooving process from boundary to boundary is so large that the time dependence of the groove formation cannot be determined by comparing measurements for different boundaries

---

\* An estimated loss of  $\sim 0.1 \mu\text{m}$  in thickness occurs by free evaporation.

annealed for different lengths of time. This point is illustrated in Figures 29 and 30 where the groove width ranges are plotted against time for samples annealed at approximately 950 and 1300°C, respectively.\* No characteristic time dependence can be assigned due to the large range in widths. Thus meaningful time dependencies can only be obtained by monitoring the groove formation for individual boundaries over a range of times.

Interference optical microscopy was used to determine the time dependence of groove formation on specific boundaries.\*\* This method requires larger thermal groove widths. Therefore, experiments were conducted at a higher temperature, 1600°C, yielding measurable thermal groove widths in realistic times.

The thermal groove widths are tabulated as a function of time for the LD and ADL specimens in Table IV and V, and plotted Figures 31 and 32 respectively. The widths are reported as a range which typically represents the uncertainty in the positions of the groove hump maxima, approximately 0.2  $\mu\text{m}$ . Larger differences indicate that the groove width is variable along the boundary or reflect occasional situations where the resolution at that boundary was poor. As plotted, the symbols

---

\* The widths for samples annealed near 950°C are adjusted to compensate the the different temperature assuming surface diffusion with  $\Delta H=100$  kcal/mole.

\*\* Repeated annealings and measurements could be performed at lower temperatures only if the groove widths were measured using SEM. This would require repeated coatings followed by acid etchings to remove the coatings. Furthermore, it may not provide sufficient accuracy due to the ambiguity in the groove width caused by severe faceting, or the uncertainty in position for smooth samples.

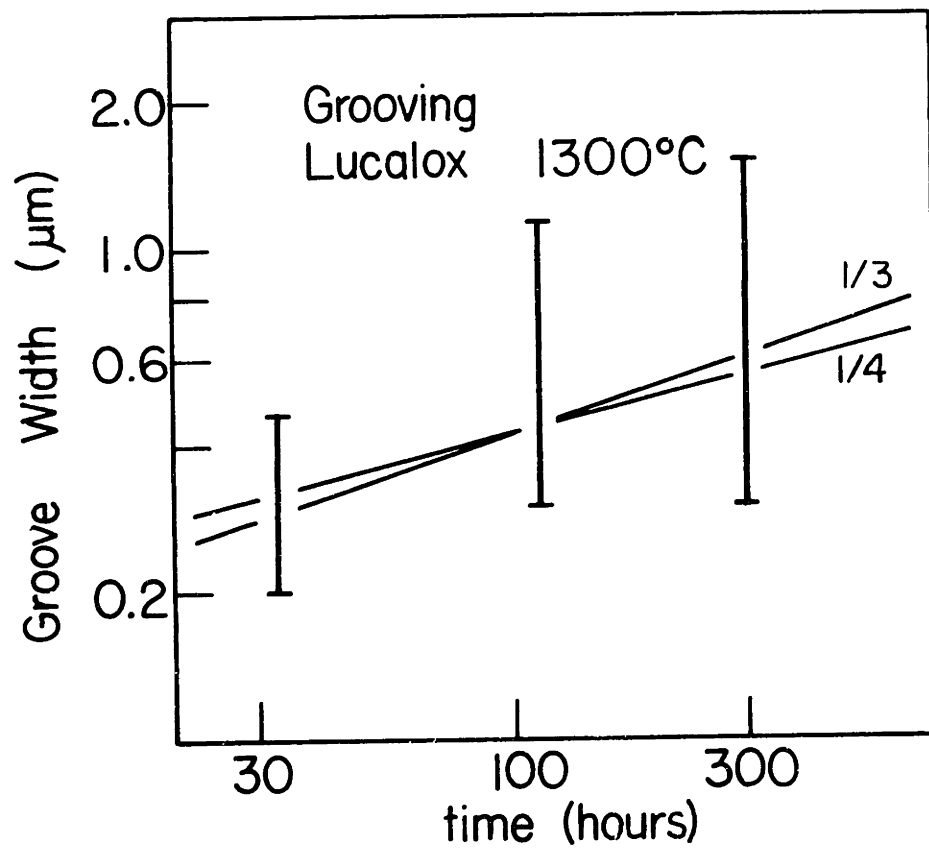


Figure 29 The groove width versus time for LTVA samples at 1300°C

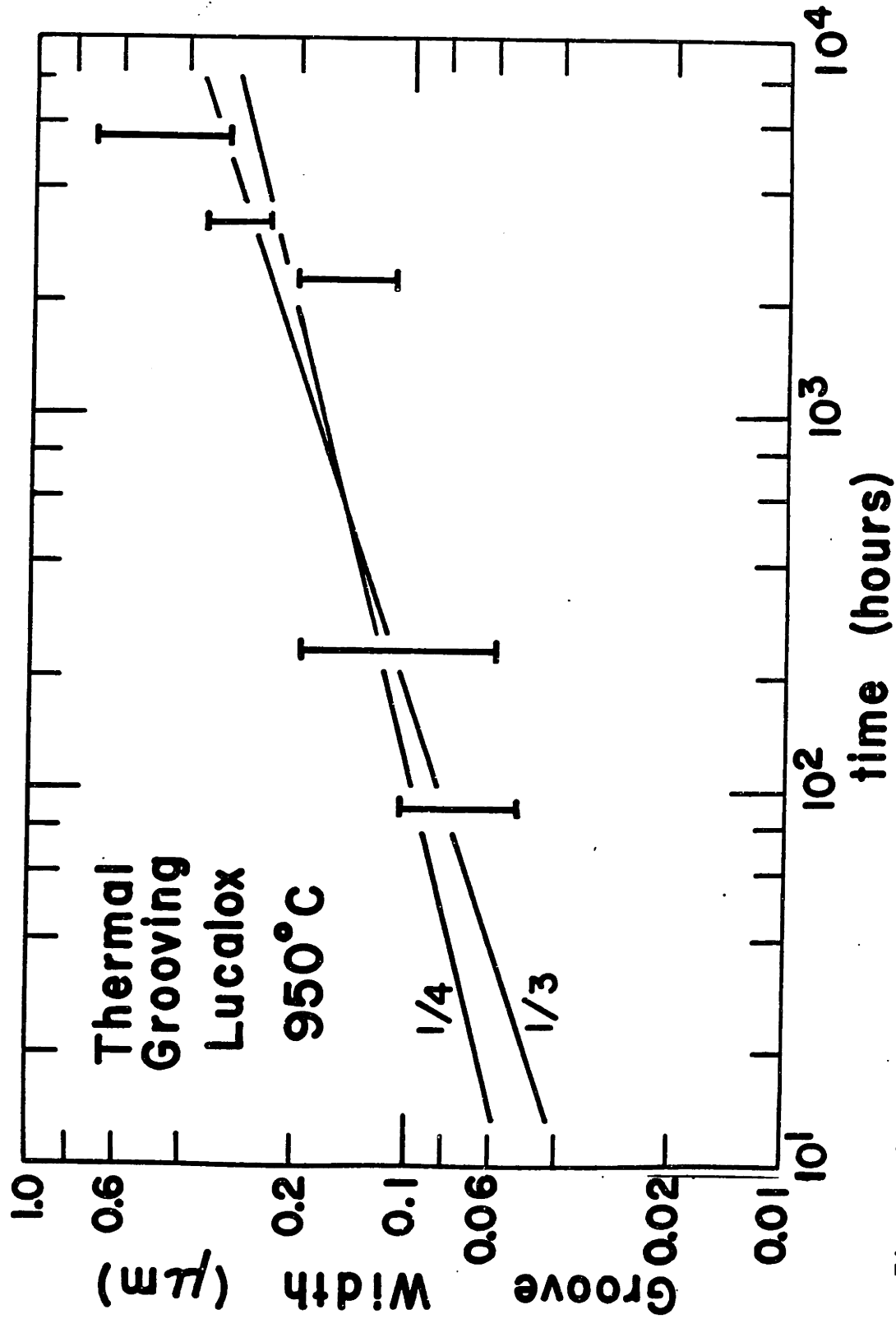


Figure 30 Groove width versus time for Lucalox samples annealed at  $950^\circ\text{C}$



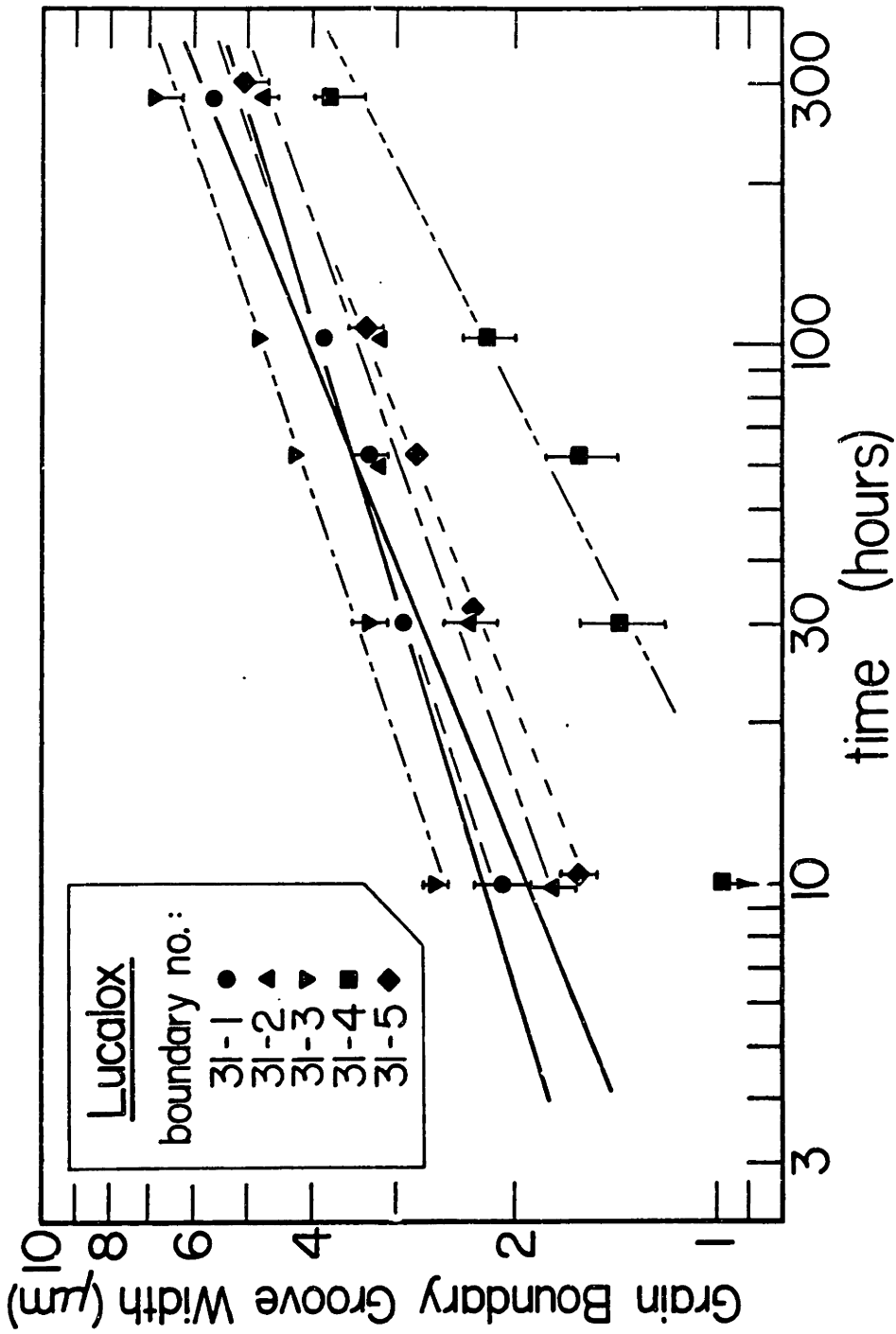


Figure 31(a) Log groove width versus log time, for LD samples, GBG27.

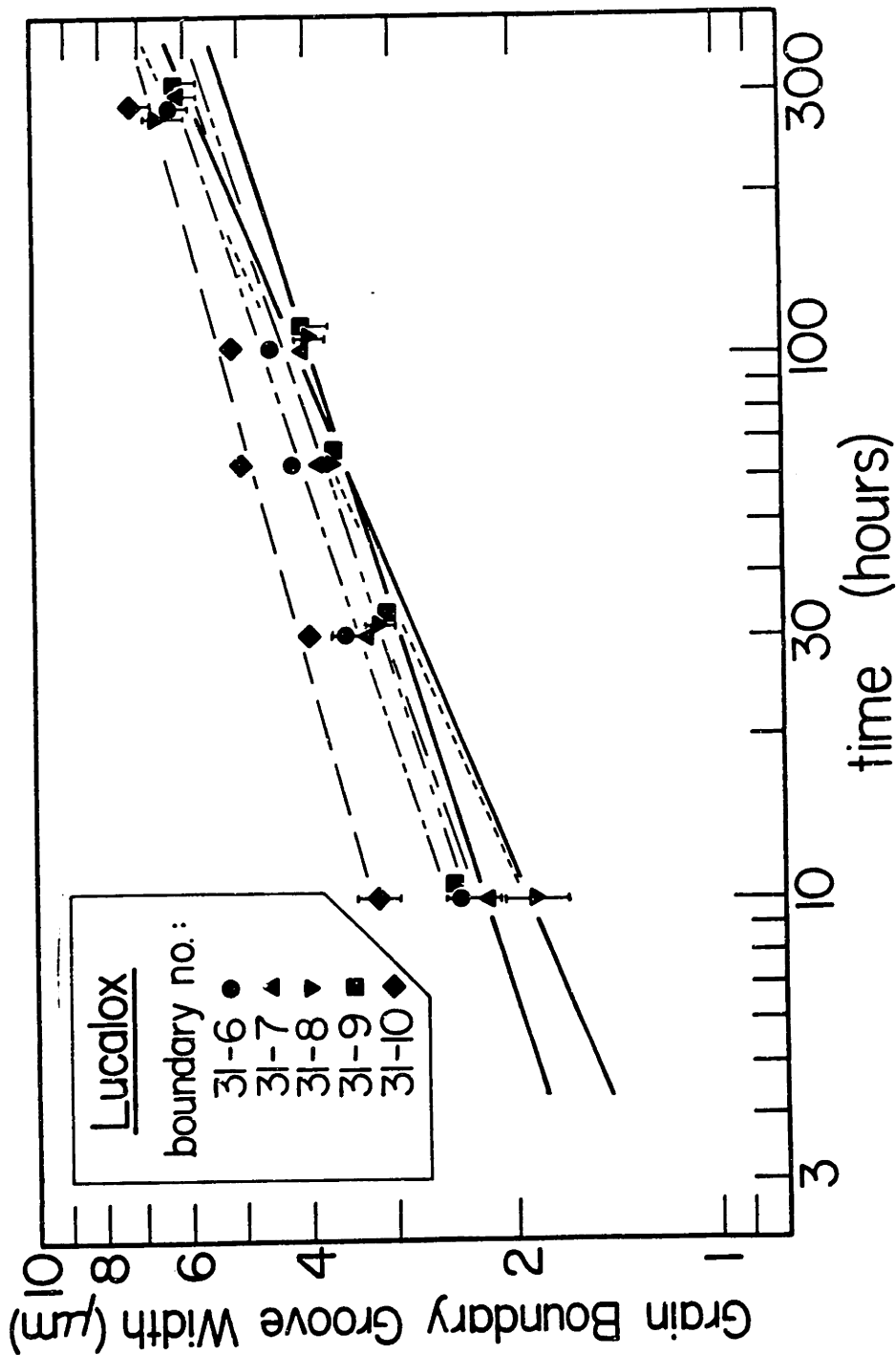


Figure 31(b)

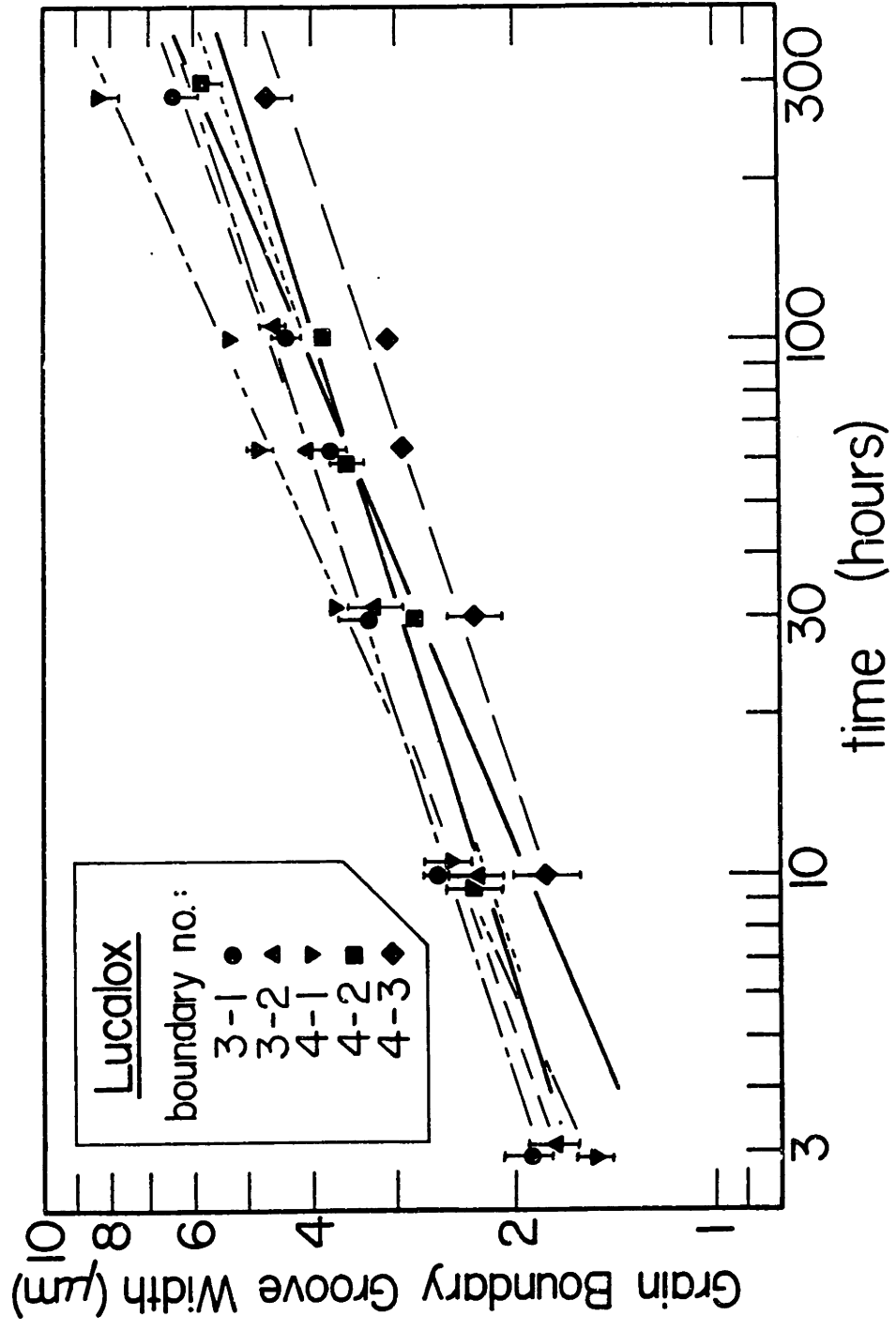


Figure 31(c)

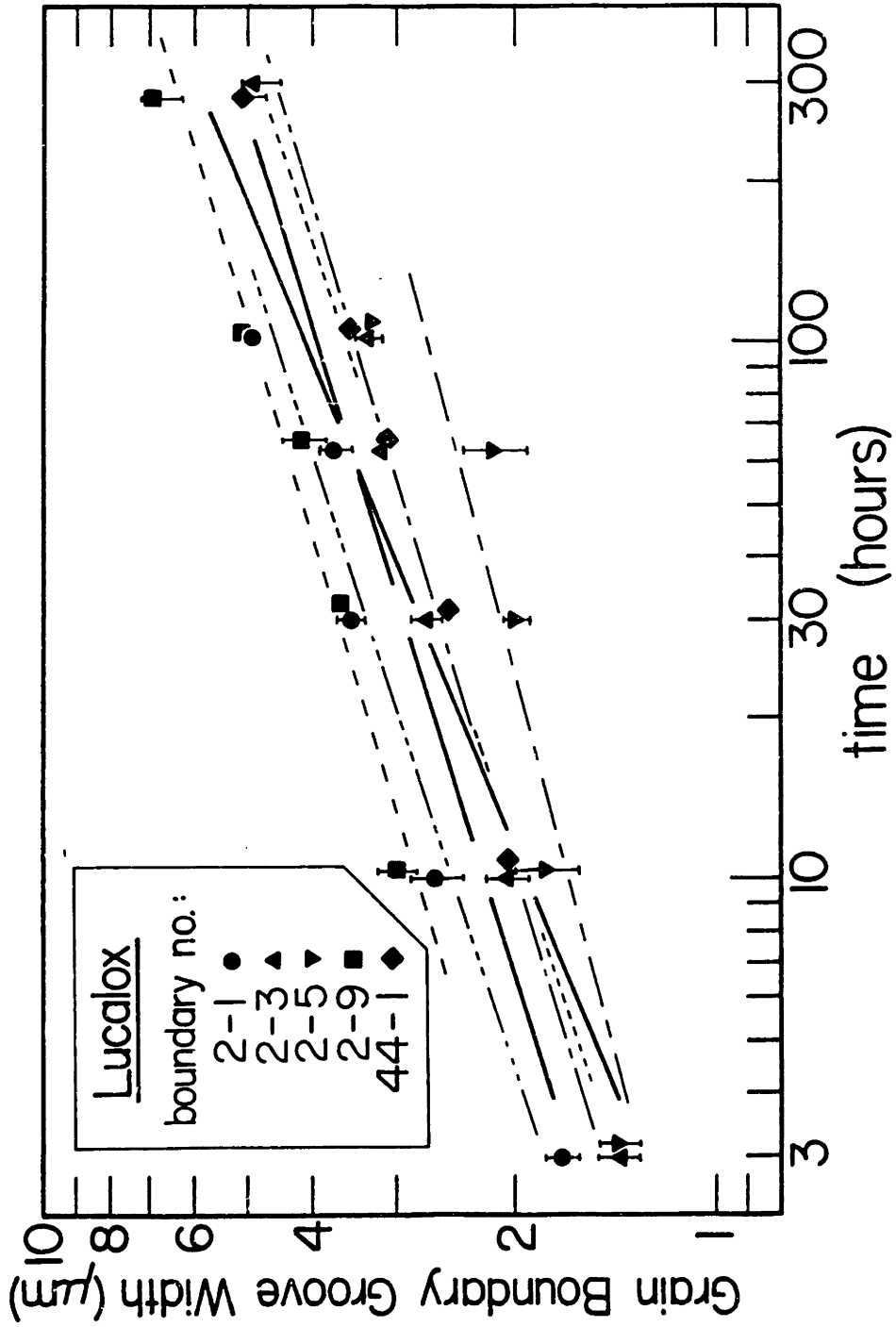


Figure 31(d)

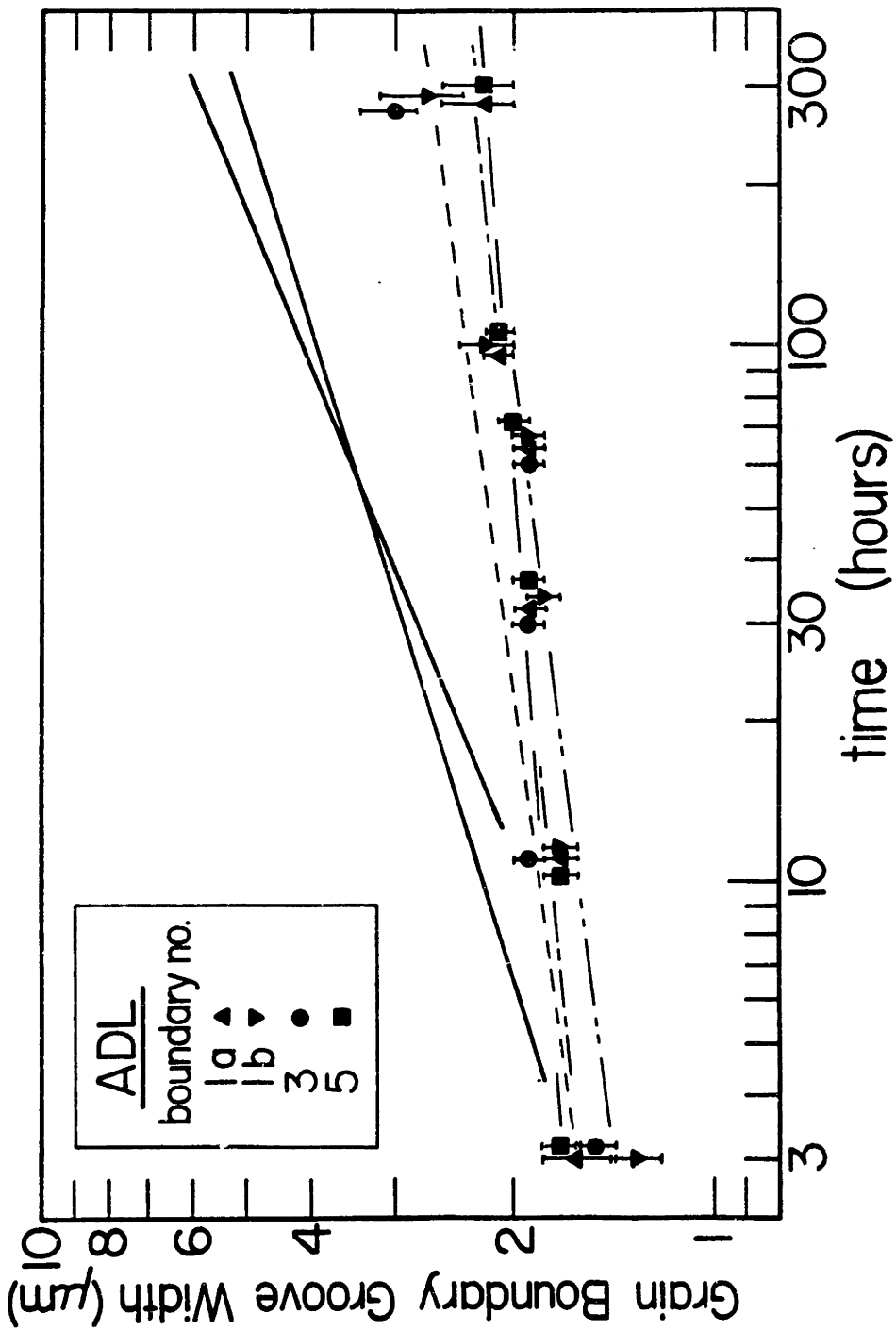


Figure 32(a) Log groove width versus log time, for ADL samples (GBG29)

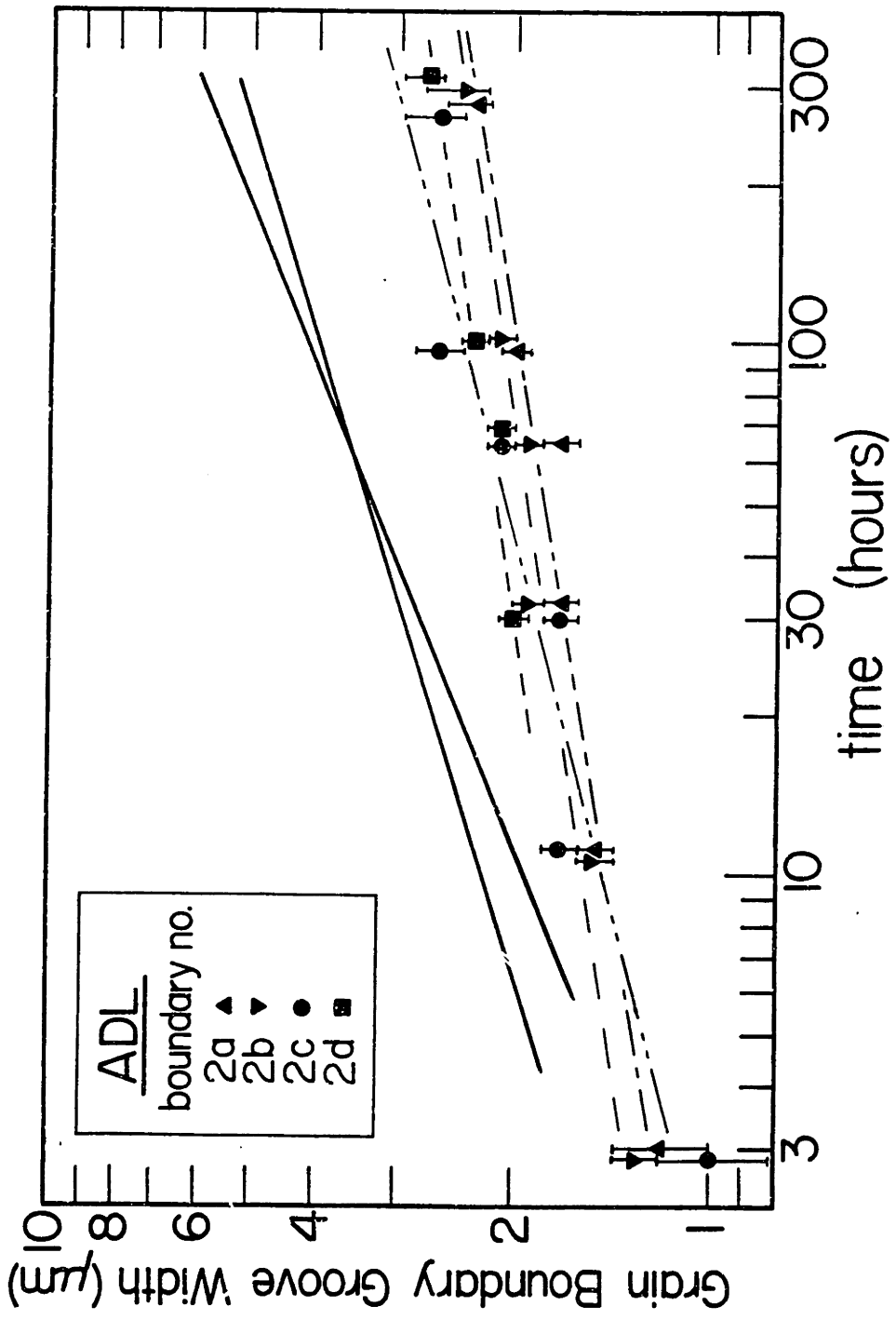


Figure 32(b)

are usually large enough to encompass the uncertainty; otherwise the width ranges are denoted by error bars. The error bars for the annealings where the temperature drifted, at the longest times, are extended by 7% compensating for the deviation. (This estimated correction is rationalized in Appendix IV.) Solid lines with slopes of  $1/3$  and  $1/4$  are included in the same position in each figure, and serve as reference markers. The broken lines in these figures represent straight line approximations for each data set. The LD samples in which height differences developed or boundary migration occurred are specifically noted in Table IV.

During the annealings, limited grain growth and rearrangement proceeded in the LD samples. This is evidenced by the disappearance of small grains followed by migration of previously stationary boundaries. Most of the thermal grooving data are from boundaries which did not migrate, as judged by the straightness of any specific boundary and by checking its position relative to other boundaries and reference markings, such as pores and scratches. Migration was detected in only two of the boundaries being monitored prior to the last time segment; in the final anneal, migration occurred in 4 of the 20 boundaries investigated.

The results show that the proportional differences in groove widths among the individual boundaries remained approximately constant throughout the experiments, Figure 31. For 18 of the 20 boundaries the difference in groove widths is at most a factor of 2X; for all 20 boundaries, the difference is a factor of 3X. For most boundaries, a specific straight line adequately represents the data, i.e., within the error bars. The data are poorly fit by a straight line in only one case; this boundary,

2-5, migrated at short and long times. Scatter greater than the average was found for five other boundaries (2-1, 31-2, 31-7, 31-8, 31-9). Migration occurred during most of the experiment for boundary 2-1. Variable groove widths along the boundary and poor resolution on some micrographs also contribute to the scatter. The boundary with the slowest rate of groove formation was present during the entire experiment, and therefore, not the result of a late start due to migration. The groove formation rates for the four boundaries which migrated during the final annealing did not vary systematically. In fact, the groove widths for these boundaries nearly spanned the range from the largest to the smallest rate. The repolishing and reannealing experiment (GBG33) showed the same variability in widths and similar asymmetric profiles.

The results indicate that most of the grooves in the 2 to 3x band develop in a well behaved manner. The surfaces of these LD specimens remained relatively smooth, only a few linear facets developed (Figures 13, 20, and 21). Many of the groove profiles are reasonably symmetric and resemble those expected for an isotropic material. The profile shapes of most grooves, including asymmetric ones, is preserved; only the scale changes. From these facts, the quantitative use of the surface grooving models is justified.

Values of  $d \log W/d \log t$  for the 20 boundaries on the LD samples range from 0.21 to 0.46. For 17 boundaries the range is 0.25 to 0.33 which is consistent with a mixture of surface and lattice diffusion processes; most of this latter set are characterized by a value closer to 0.25 than to 0.33. No systematic correlation between the values of  $d \log W/d \log t$  and the relative magnitudes of the groove widths is



apparent. The fit of individual lines to the data would be slightly better for 60% of the boundaries if the line had a slight upward curvature. This is consistent with a transition from surface to lattice diffusion controlled grooving, as shown previously in Figure 8b; variable diffusivities are implied. Of the 3 boundaries with  $d \log W/d \log t$  values outside the range of 0.25 to 0.33, boundary 31-10 has the fastest rate of groove formation, boundary 31-4 has the slowest rate of groove formation, and boundary 2-5 has the lowest value of  $d \log W/d \log t$  and is characterized by migration during the last time period of this experiment; break away and reformation could account for the smaller widths and the low value of  $d \log W/d \log t$  in this case.

The data for the ADL samples are also from stationary boundaries as deduced from the straightness of particular boundary segments and the orientation of various segments with respect to each other. Even boundaries with considerable curvature did not migrate.

The proportional differences among the groove widths for individual boundaries on the ADL samples varied throughout the experiment, Figure 32. Presumably, some of the scatter in this data is the result of variable widths along the boundaries, as repeated measurements on the exact location are improbable. For short times, the uncertainty in the measurement is primarily responsible for the larger variability; the scatter in the data for the long times is not understood. A band approximately 1.5x in groove width encompasses all but a few short time data points. This band lies at smaller widths than that noted for the LD samples. The individual data sets are better represented by specific

straight lines than by any average line. Many intersections of these individual lines occur during the annealing time.

Thermal grooves on the ADL samples do not develop in a self-similar manner. The grain surfaces and the groove profiles are extensively faceted, as shown in Figures 17 and 23. Detailed characterization of the faceting as a function of time cannot be made from the interferograms. Consequently, the stages of evolution for the profile shape are unknown.

Values of  $d \log W/d \log t$  on specific boundaries vary from 0.054 to 0.19. For the entire band of data,  $d \log W/d \log t$  ranges from 0.10 to 0.16. These values are not characteristic of either a surface or lattice diffusion controlled process.

### C. Dihedral Angle Determinations

Dihedral angles were calculated assuming the profile shapes predicted by Mullins' models and compared to those determined from interference profiles. From interferometry, the dihedral angle is [after Amelinckx (1953)], for discussion, see also Gjostein and Rhines (1959):

$$\theta = 2 \tan^{-1} \left( \frac{2L}{\lambda M} \tan \frac{\eta}{2} \right) \quad (29)$$

where  $L$  is the interference line spacing;  $\lambda$  is the wavelength of the light source,  $5.4 \times 10^{-7}$  m;  $M$  is the magnification; and  $\eta$  is the groove root angle measured on the interferogram.

For Mullins' model for thermal grooving by surface diffusion, the dihedral angle is:

$$\theta \approx 180^\circ - 2 \tan^{-1} \left( \frac{d}{0.211 W} \right) \quad (30)$$

where  $d$  is the depth of the thermal groove and  $W$  the thermal groove width. This equation is approximate in that the numerical coefficient is mildly dependent on  $\theta$ , as discussed previously.

In general, the dihedral angle is not constant for either the Lucalox or ADL materials, as determined by either method, see Table VII. The measured values for the Lucalox materials vary from  $114^\circ$  to  $156^\circ$ ; for the ADL samples, the range is  $117^\circ$  to  $150^\circ$ . Neglecting torque terms, this variability in the dihedral angle corresponds to ranges in  $\gamma_b/\gamma_s$  of 0.42-1.09 and 0.52-1.04, respectively. Asymmetries in some dihedral angles were noted for both materials. For those specific boundaries where  $\theta$  was measured at two different annealing times, a larger value was often determined for the observation at longer time. This may result from a decreasing resolution of the groove root on the interference micrograph as the groove depth increases. Note that the values of  $\eta$  range only from  $4^\circ$  to  $13^\circ$ . Accurate measurement of  $\eta$  is most important at the smaller angles,<sup>\*</sup> where the difficulty in measurement is greatest. Some variability in the dihedral angle was noted along specific boundaries; for example, see the results of the ADL samples or for the LD material, boundaries 27-31-3c and 27-4-2c.

For the Lucalox samples, the agreement between the calculated and the measured dihedral angles is reasonably good for approximately 70% of the values<sup>\*\*</sup> listed in Table VII. This includes some cases where faceting, an altered groove profile (freely evaporating sample, GBG25), or variable groove depth has developed. These results apparently indicate that the assumptions in the geometry are approximately met on many of the grooves examined.

---

\* A typical example is: if  $\eta$  is  $11.^\circ \pm 0.5^\circ$ , then  $\theta$  is  $152^\circ \pm 1^\circ$ ; if  $\eta$  is  $6.^\circ \pm 0.5^\circ$ , then  $\theta$  is  $131^\circ \pm 4^\circ$ .

\*\* Use of the corrected form of Eqn. (30) would lower  $\theta$  by 1 to  $4^\circ$ , as discussed previously.

Although the data are limited, the agreement appears to be much poorer for the ADL samples. These results suggest that when faceting is severe the ratio of the peak widths to the groove depth is often significantly different than that expected from thermal grooving of an isotropic surface.

#### D. Diffusion Coefficients

In this section, the thermal grooving results are presented and compared in terms of diffusion coefficients calculated using Eqs. (7) and (9). Both diffusion mechanisms are considered because the time dependence for the LD material suggests this, although surface diffusion is favored.

For each of the samples annealed at other temperatures, the thermal groove widths were measured within a range of uncertainty for a large number of boundaries. All measurements for each experiment were compared and an overall range assigned based on the minimum and maximum widths. The extremes are usually supported by several observations; in a few cases where a single width was significantly different from all others, it was neglected. Table VI summarizes the width ranges and other pertinent information including the number of measurements and comments on microstructural features. Except where the time dependence was measured, the implied surface and lattice diffusivities were calculated by attributing all the grooving to that specific diffusion process. For the LD samples (GBG27), surface diffusivities were determined for the maximum and minimum grooving rate where  $d \log W/d \log t$  was approximately equal to  $1/4$ . An analogous procedure was carried out for lattice diffusivities when  $d \log W/d \log t$  was approximately  $1/3$ . For the ADL samples (GBG29), only the short time data are used even though the time dependence does not indicate lattice

or surface diffusion kinetics. This assumes that thermal grooving develops in a manner prescribed by Mullins' models. However, results are easily compared in this form.

The ranges of implied surface and lattice diffusivities are plotted for comparison with reported values in Figures 33 and 34, respectively;  $\omega D_s$  values are from grooving and MSS experiments only. These comparisons suggest that both surface and lattice diffusion could contribute to the thermal grooving at temperatures above 1200°C; only surface diffusion is important below 1200°C for the smaller groove widths. Generally the implied diffusivity ranges are larger for the lower temperatures. At 1600°C, for the LD material spans the band of  $\omega D_s$  values defined by Lines 7 and 9, Figures 1 and 33. The average\* surface diffusivity value, denoted in Figure 33, is slightly smaller than that reported for a similar Lucalox material [Robertson and Ekstrom (1969)]. The magnitude of the ranges of  $\omega D_s$  for the pure materials at 1600°C, GBG28 and 29, falls at smaller values. The high part of these ranges are similar to the  $\omega D_s$  values reported for most other undoped material [Shackelford and Scott (1968), Huang et al. (1975), and Robertson and Ekstrom (1969)]. Interestingly, inclusion of a  $\omega D_s$  value for the slowly developing boundary (GBG27-31-4) would bring the band for the LD material down almost to the bottom of that for the pure samples. However, if the long time values for the ADL specimens were used, the apparent diffusivity range for the pure materials would be decreased by another factor of approximately 3X. However, neither of these latter examples is obviously diffusion controlled. At 1840°C, the  $\omega D_s$  values for the LD material (GBG26) are considerably larger than those for the pure materials (GBG30 and 31).

\*The average was calculated for 16 of the 20 boundaries for GBG27 where  $n \approx 4$  for  $1/n = d \log W/d \log t$ .

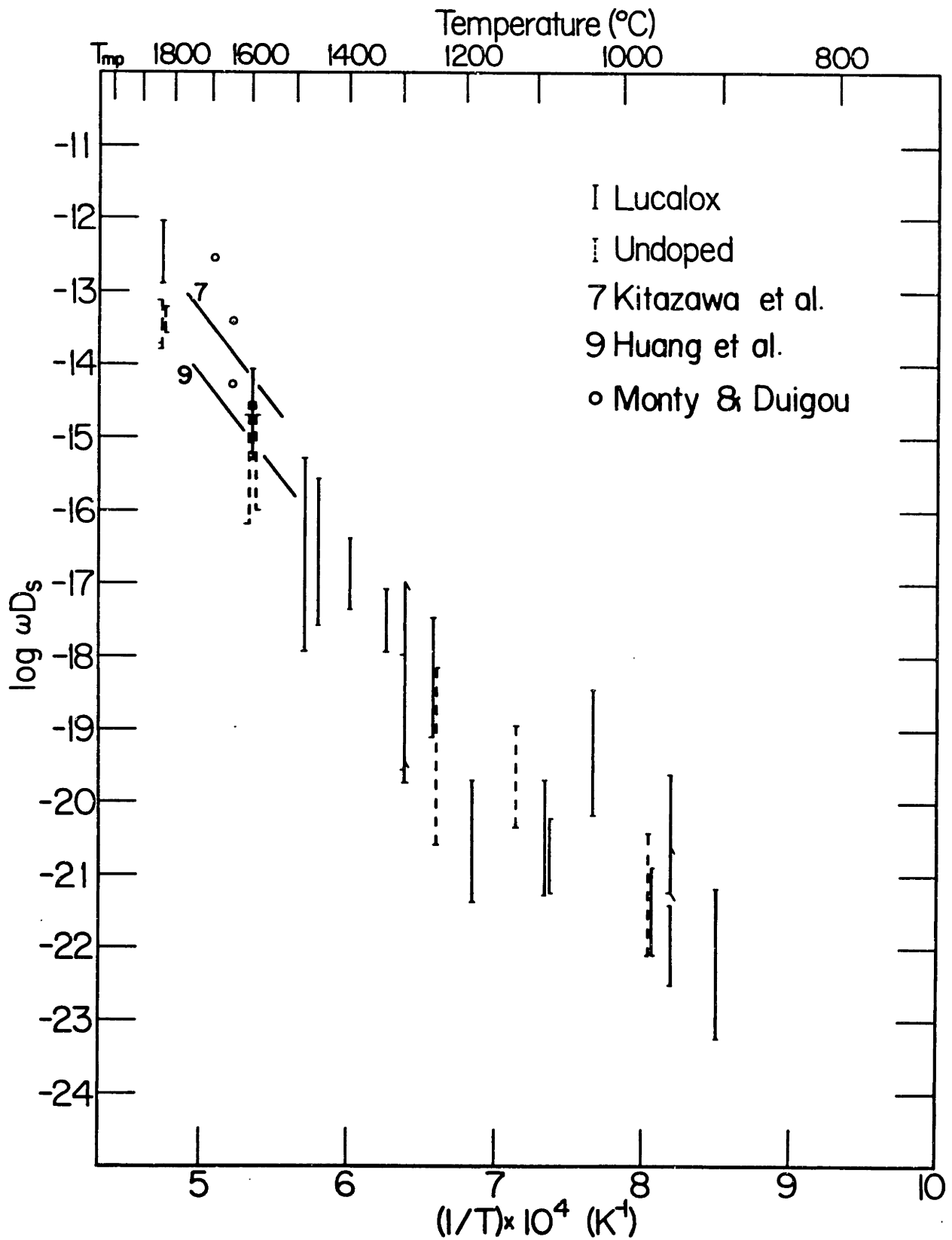
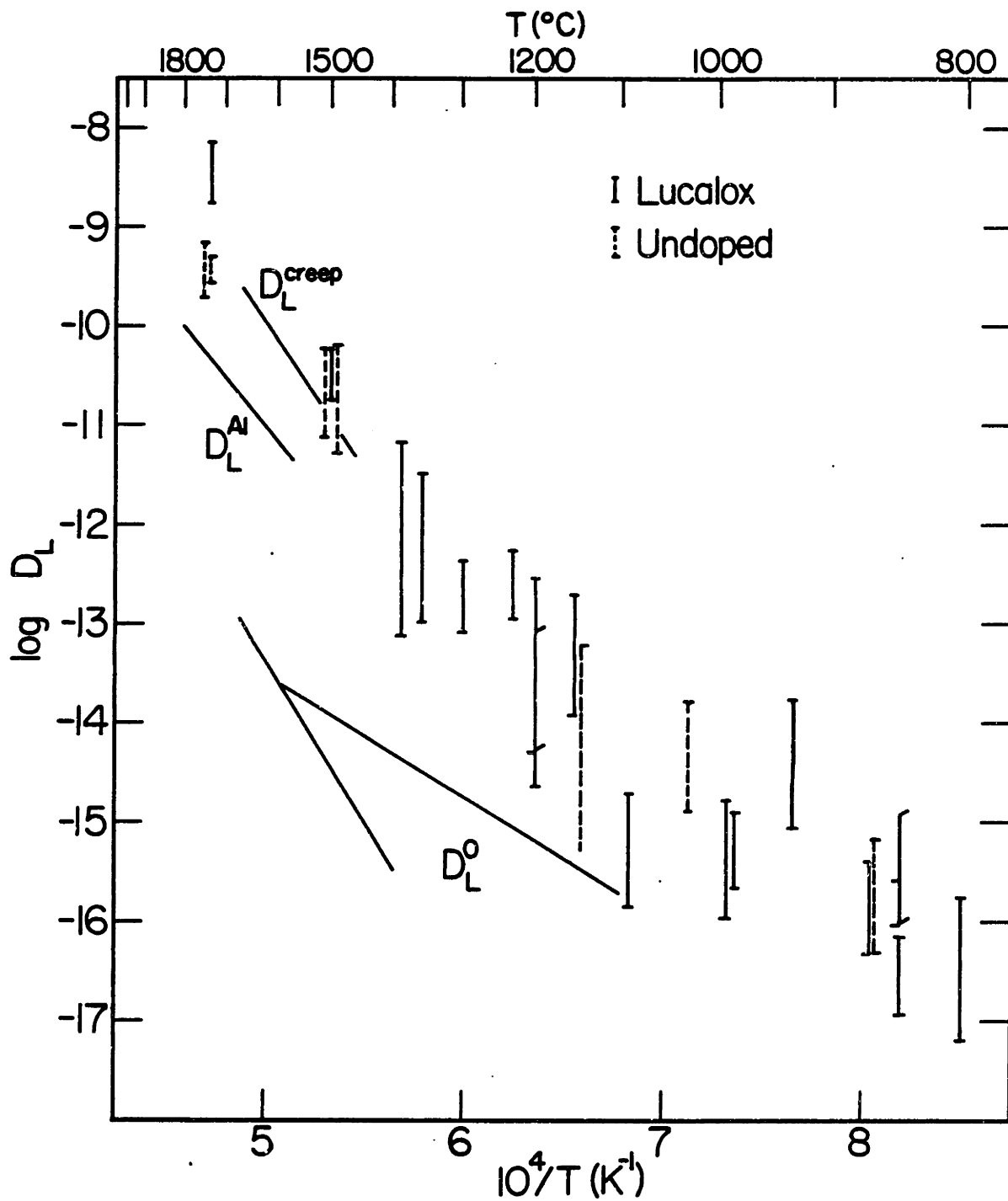


Figure 33  $\log \omega D_s$  versus  $1/T$ .

Figure 34 - Log  $D_L$  versus  $1/T$

Except at 1840°C, the ranges in calculated lattice diffusivities for the three materials have similar magnitudes which seems unreasonable at these temperatures. Further, the magnitudes of  $D_L$  in these ranges are larger than expected, especially for the pure materials, suggesting that lattice diffusion does not make the dominant contribution to groove formation.

At low temperature, the results for the Lucalox samples are quite different from sample to sample but do not vary systematically with the anticipated differences in impurity levels. For example, at  $\sim 1090^\circ\text{C}$  the results from the relatively purer LTVA samples (GBG5) are equivalent to the results from LD samples (GBG24) where second phase precipitation along the free surface was found. In an experiment on similar LTVA samples (GBG14) at a slightly lower temperature ( $\sim 1030^\circ\text{C}$ ) the band of surface diffusivities is shifted up by a factor of 10X and has an even greater range in values. Overall, relatively similar values are found for the ranges of implied diffusivities for the pure and Lucalox samples below 1250°C.

Another interesting aspect of the  $\omega D_s$  values at low temperatures is the consistently lower ranges of  $\omega D_s$  for widths determined from grooves approaching the resolution limit using the SEM. This is shown for the results of GBG18, plotted as  $\log W$  versus  $\log t$  in Figure 30, or in the implied diffusivities in Figures 33 and 34. These results suggest that  $d \log W / d \log t > 1/4$  or  $1/3$ . Alternatively interpretations are: that the very smallest groove widths cannot be measured accurately, that impurities are being exsolved and increase  $\omega D_s$  as time progresses, or that faceting develops later and broadens the range in groove widths, or provides surface



features which assist in the measurements from the SEM micrographs, i.e., more contrast results from faceted rather than smoothly contoured surfaces.

## VII. DISCUSSION

### A. Variability in the Thermal Groove Widths

There is significant variability in the grain boundary groove widths which is much more than the experimental errors in measuring the widths. These translate into several orders of magnitude variability in the diffusivities calculated using Mullins' models for isotropic materials because  $W^n \propto D$ . Factors which could contribute to the variability in the thermal grooving process can be categorized as; (1) grain boundary migration, (2) the existence of an initial thermal groove width on some boundaries, (3) faceting or profile distortion due to anisotropy in  $\gamma$ , (4) anisotropy in  $D_s$ , and (5) impurity effects on  $\gamma$ ,  $D_s$ , and  $D_L$ .

#### 1. Groove Width Variability Due to Grain Boundary Migration

Some measurements were made on boundaries that migrated during the time dependence experiments, GBC27. The grooving rates are not categorically high or low as compared to stationary boundaries. However, the implied rate was barely positive between sequential measurements in a few cases. This could indicate that breakaway, migration and groove reformation occurred; recall that the "recovery" groove width is nearly equal to the width for a nonmigrating boundary in  $3 t_0$ , Figure 8d (As  $3x$  increases in time were used in these experiments, it is likely that for an occasional breakaway the width for the recovery boundary would be larger than the previously observed groove.). However, such breakaway boundaries could not go undetected, as the remnant or "ghost" would still be evident.

For a limited number of boundaries that migrated during experiments, the grooves were checked to compare the profiles and observed rates of migration with those expected for migration limited by groove drag (after

Mullins (1958)). In general, the profiles were quite variable. Examples range from profiles as predicted by Mullins, i.e., an enlarged hump on the grain that the boundary is migrating towards and absence of a hump on the backside grain, to cases where the hump is on the wrong side of the migrating boundary. The migration rates were often too slow to be limited by groove drag; consistent with the slower migration rate, most of these groove profiles were characterized by humps on both sides of the boundary. In only a few cases did the boundary break away from its groove without being subsequently annihilated. No attempt was made to document the subsequent thermal grooving behavior as a function of time. It is of interest to note that apparently stationary boundaries occasionally exhibited profiles indicative of boundary migration limited by groove drag. These facts support the contention that boundary migration is not the primary cause of the variable grooving rates.

For other samples annealed only once, measurements were avoided on curved boundaries, profiles indicative of boundary migration, and for boundaries near ghost grooves. Therefore, the previous assessment is applicable for these experiments, i.e., boundary migration is not a significant cause of the variable grooving rates at any of the temperatures.

## 2. Groove Width Variability Due to an Initial Thermal Groove

The existence of an initial groove width ( $W_0$ ) on some boundaries can, in principle, cause a variability in the observed thermal grooving rates. There are, however, several reasons why this is not important here. Firstly, for  $W_0$  to be important it must be approximately half the first groove width observed. This width would be of the order  $1/2 \mu\text{m}$  in the time-dependence experiments, a value which could not go undetected

using either optical microscopy or the SEM. If there were variable  $W_0$  values for the different boundaries (and samples) studied, the band of groove width values would converge with time. This behavior is not shown by the data. Finally, no indication of an initial width was found on the as-polished, acid-washed surfaces.

### 3. Effect of Faceting on the Thermal Grooving Process

#### (a) Altered Geometry Considering Volume Conservation in 2-d.

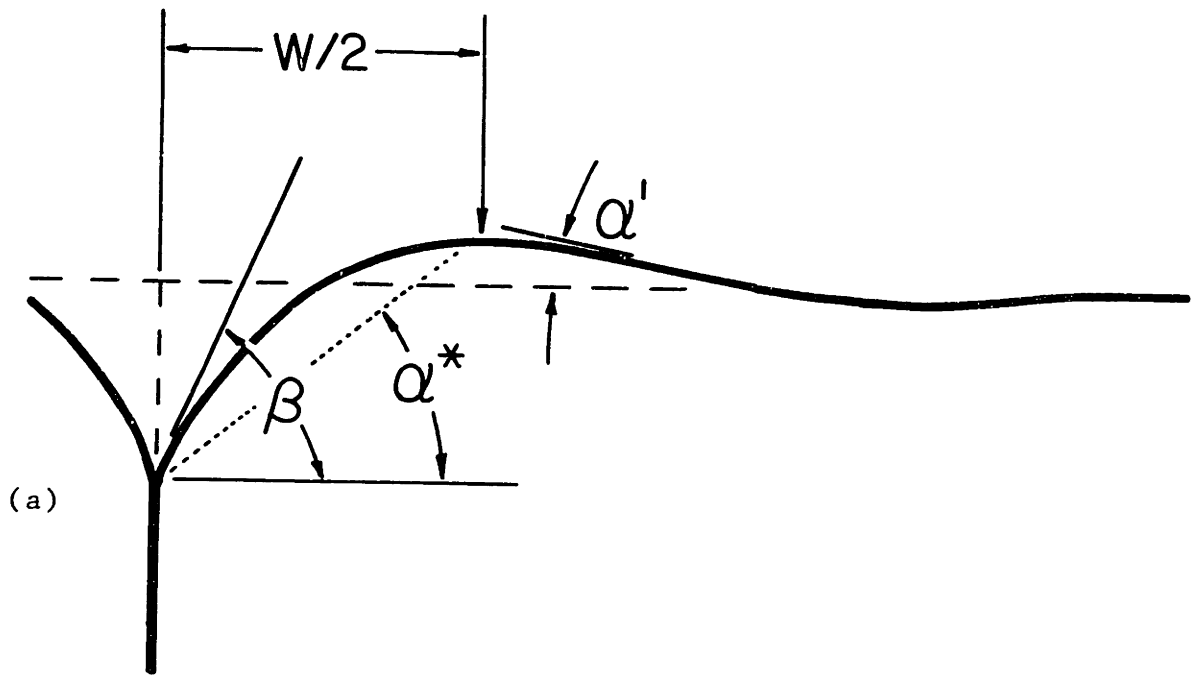
In this section the variability in the thermal groove width, as defined by the facet peaks, is considered from the standpoint of volume conservation. All matter that is transported from the digging of the thermal groove must appear in the humps adjacent to the boundary. However, if faceting is important, the thermal groove profile is segmented. The shape and position of the peak depends in part on the orientation of the facet planes. For an equivalent amount of volume transported, the width could be larger or smaller than that for an isotropic surface. For the example displayed in Figure 17c, the thermal groove width defined by the two facet peaks is approximately equal to the width associated with isotropic surface energy. However, significantly different widths would result for symmetric groove profiles like either of the two faceted cases shown. For example, there is a factor of approximately 5X between the half-groove widths shown in Figure 17c, where the groove width for an isotropic surface tension lies between these extremes. Obviously, no single characteristic geometry exists.

However, the range of orientations for which facet formation is certain is limited to those exposed by the thermal groove profile. A schematic showing the form of the relation between the relative groove "half-width", as defined by the facet peaks, and the facet orientation is shown in

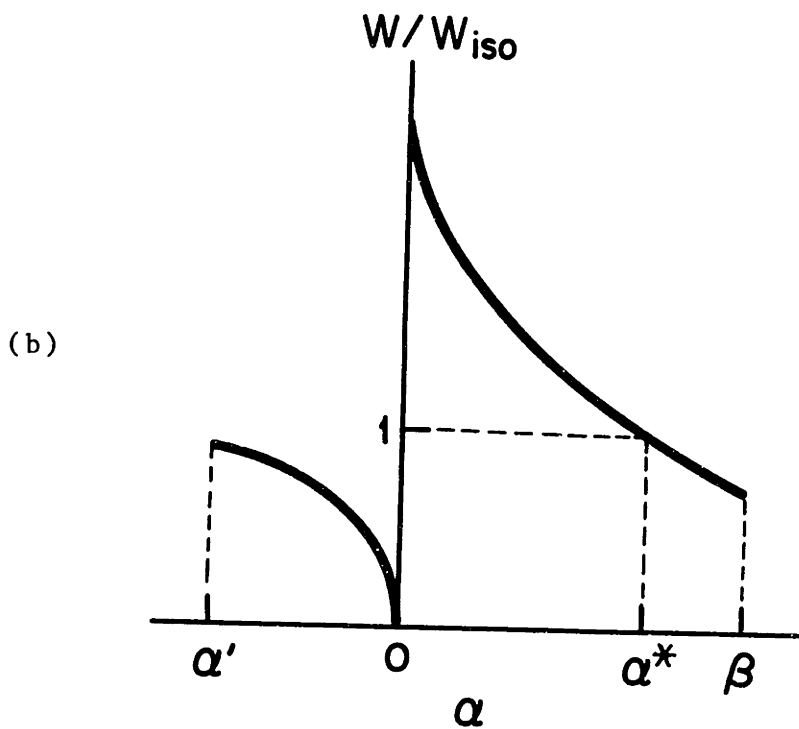
Figure 35, where  $\beta$  is the groove root angle;  $\alpha$  is the facet angle, and  $\alpha'$ , the angle of the tangent at the inflection point of the groove profile; all angles are taken with respect to the sample surface; and  $\alpha^* \equiv \tan^{-1} \frac{2d}{W_{iso}}$ , where  $d$  and  $W_{iso}$  are the groove depth and width for isotropic surface energy and diffusivity. This figure clearly shows that a broad range of thermal groove widths is expected if any faceting is present. The use of models developed assuming isotropic surfaces would therefore appear to be inappropriate for interpreting such complex processes. Further, the effects of faceting on the driving forces and diffusion along the surface must also be considered.

(b) Effect of Faceting on Mass Transport in Two-Dimensions

Many of the considerations of the effects of faceting on mass transport during thermal grooving stem from the treatment of the growth of an existent, isolated linear facet by Mullins (1961), described earlier. The problem is more complex when the facet is part of a grain boundary groove than either of the separate problems. This results because (1) diffusion must occur across the facet(s) for the groove to deepen and/or, (2) either the facet plane, the boundary-surface intersection, or both must move parallel to the surface. Which of these processes occurs depends on the orientation of the facet(s) with respect to the surface and on the relative surface diffusivity on the facet plane,  $\lambda$ . If there are no additional facets, a faceted groove profile may grow by surface diffusion through a series of self-similar shapes with the width proportional to  $t^{1/4}$ . However, there are conditions that may cause significant enhancement or reduction in the thermal grooving kinetics, and sometimes different time dependencies.



(a)



(b)

Figure 35(a) Schematic half-groove profile defining the angles  
 (b) Ratio of the apparent width to the isotropic groove width versus the facet angle

For the case where  $\alpha' < \alpha < \beta$ , the facets will be present initially. The growth rate depends on an effective B-value which reflects an integrated product of  $D_C(\gamma+\gamma'')$  and  $D_F(\gamma+\gamma'')$  over the exposed surface. Generally,  $B_{eff}$  will not be equal on both sides of the boundary. Thus, the expression for W is the sum of two half groove widths:

$$W = A_1(B_{eff}^{(1)} t)^{1/4} + A_2(B_{eff}^{(2)} t)^{1/4} \quad (31)$$

where A is a numerical coefficient which depends on  $B_{eff}$  and the orientation of the facet plane; it is expected that  $A_i$  may vary by approximately 5x, as discussed previously.

Five simple cases illustrate most of the different types of behavior which could be anticipated:

- (1) a single facet on each side of a symmetric groove profile, with rapid diffusion on the facet; the half-groove is shown in Figure 36;
- (2) as in Case 1, only with slow diffusion on the facet;
- (3) where facet dissolution or translation (adding atom layers to or subtracting layers from the facet is slow, or the boundary is relative immobile;
- (4) as in Case 1, only the originally flat grain surface consists of a series of periodic linear facets as shown in Figure 37, with fast diffusion on the facets;
- (5) as in Case 4, only slow diffusion on the facets.

These examples are not treated rigorously; they give insight into the expected kinetics and causes of variability in grooving experiments.

For the geometry depicted in Case 1,  $0 < \alpha < \alpha^*$ , rapid diffusion on the facet plane ( $\Lambda = \infty$ ) results in  $\partial\mu/\partial x = 0$  between points P' and Q'. Consequently, the  $\partial\mu/\partial x$  across region 1 and/or region 3 are increased relative to that for

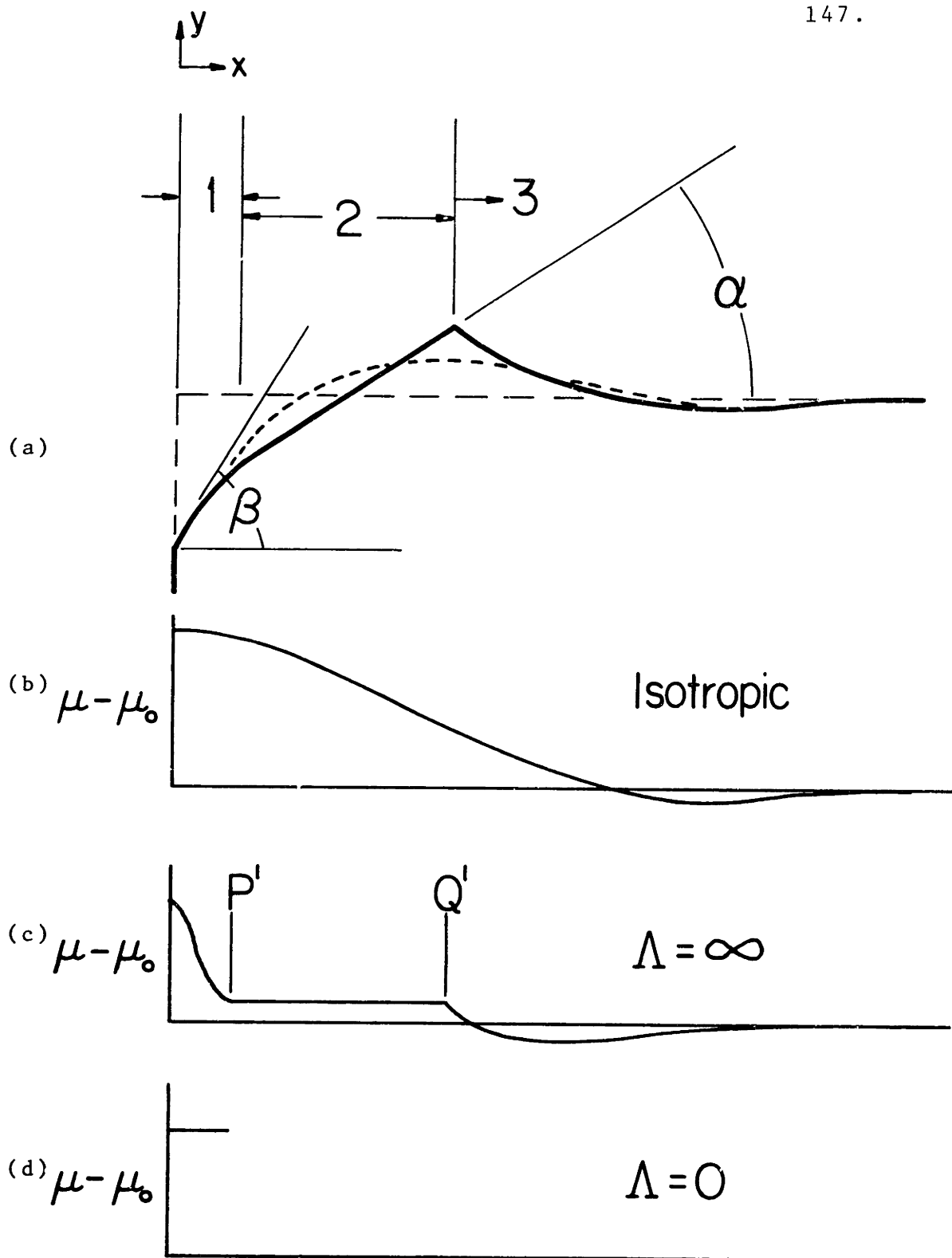


Figure 36 - A thermal groove profile with a facet:  
 (a) schematic, and the variation of the chemical potential for an (b) isotropic surface, (c) fast diffusion on the facet, and (d) slow diffusion on the facet.



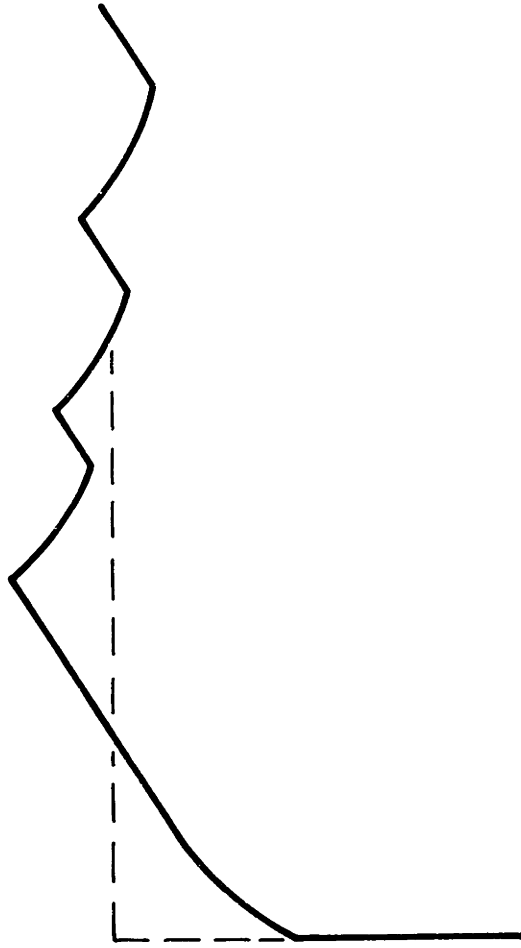


Figure 37 Schematic of faceted surface and faceted thermal groove profile.

an isotropic profile after a comparable amount of mass transport, as shown in Figure 36. The grooving rate is increased by this facet with fast diffusivity assuming that translation (dissolution) of the facet plane is not rate-controlling. For  $\alpha^* < \alpha \leq \beta$ ,  $A$  is small and the grooving rate may be increased or decreased depending on the  $\Lambda$ -value (or  $B_{\text{eff}}$ ). Similarly, for  $\alpha' < \alpha < 0$   $A$  will be small but rapid grooving may be possible, if facet translation occurs by adding layers to the facet plane.

If the facet and groove develop simultaneously, then  $d \log W / d \log t = 1/4$  where  $B_{\text{eff}} > B_{\text{iso}}$  but the grooving rates depend on the geometric term  $A$ . For  $\alpha < \alpha'$ , or  $\alpha > \beta$ , a change in  $d \log W / d \log t$  results from nucleation of a facet on an existing groove profile; if  $\Lambda$  is large then accelerated grooving,  $d \log W / d \log t > 1/4$ , may be possible during a transient period.

In Case 2, there is no mass flow across point  $P'$  when  $\Lambda=0$ . The gradient in  $\mu$  across region 1 is reduced to zero by this resulting in a surface with constant curvature; a flat plane connecting the groove root with point  $P'$  may result only if torque terms are large or if by chance  $\beta=\alpha$ . Since mass is no longer flowing across point  $Q'$ , the shape of the facet profile in region 3 and the corresponding  $\mu$ -curve take the form of the linear faceting process to the left of point  $P$  in Figure 6; the rate of facet growth is then described by Mullins' model for  $\Lambda=0$ . Hence, the thermal groove width may increase by surface diffusion even when mass is not transported from the groove root. However, the boundary groove profile will have much more mass in the groove humps than was transported from the groove root area and there will be significant undercutting outside the peak. The groove width develops with  $d \log W / d \log t = 1/4$  for all values of  $\alpha$  with  $B_{\text{eff}} < B_{\text{iso}}$  when the facet is present from zero time. The groove root depth relative

to the free surface,  $d'$ , will in fact increase proportional to  $(\Lambda D_c t)^{1/4}$  due to leakage over the facet. For the nucleation of a facet with  $\Lambda=0$  at any  $t>0$ , reduction in  $d \log W/d \log t$  will occur.

For elaboration of Case 3, consider an asymmetric groove profile where the right half is like that depicted in Figure 36 ( $0 < \alpha < \beta$ ), and the left half is a profile with isotropic surface energy. When the facet will not dissolve or translate, the grooving process proceeds until  $\partial\mu/\partial x \neq 0$  across region 1 (as in Case 2). However, the non-zero gradient in  $\mu$  on the left side of the boundary causes continued mass transport from the groove root. This upsets the balance at the groove root resulting in a net force on the grain boundary and also a net flux across the grain boundary. Consequently, it is the mobility of the boundary (or facet translation rate) that determines the profile shape and the kinetics of the thermal grooving. If the boundary has a high mobility, a self-similar shape will prevail and the width will develop in proportion to  $t^{1/4}$ . If the boundary is immobile, the self-similar shape is not preserved and slower grooving rates with  $d \log W/d \log t \neq 1/4$  are therefore expected. The right half groove width grows by undercutting with  $t^{1/4}$  kinetics but the kinetics for the left half of the groove will be slow, possibly continually decaying. Finally, it should be noted that an analogous asymmetric profile development occurs under  $\Lambda=0$  for  $-\pi/2 < \alpha < \pi/2$ .

In case 4, the geometry displayed in Figure 37 is considered for the situation where removal of atoms from the facet planes is a relatively easy process, and  $\Lambda=\infty$ . It is expected that thermal grooving will develop with  $d \log W/d \log t = 1/4$ , as in Case 1, until the facets interact with one another. The grooving rate is reduced upon facet interaction, and since the shape is not self-similar (facets will coarsen),  $d \log W/d$

In Case 5, slow diffusion on the facets in Figure 37 results in a reduction of the thermal grooving rate; for  $\Lambda=0$ , the process may nearly stop. Obviously, facet nucleation requires time in which thermal grooving proceeds in a normal fashion. It is therefore expected that at short experimental time, the grooving rates (small  $\Lambda$ ) are unaffected by faceting on the far surface. This rate is reduced upon the onset of interaction between the thermal groove and the evolving surface facets.

In summary, when a facet exists on the thermal groove profile, the numerical coefficient in Equation (7) becomes a variable which depends on the orientation of the facet with respect to the sample surface and on the ratio  $\Lambda$ . If the motion of the profile is surface diffusion controlled,  $d \log W/d \log t = 1/4$ ; however, the groove depth will not increase for  $\Lambda=0$  and width growth occurs by undercutting of the adjacent flat surface. For  $\alpha' < \alpha < \beta$ , it is expected that facets will be present on the groove profile from  $t=0$ ; whereas, nucleation of facets with other values of  $\alpha$  or of surface facets occurs at  $t>0$ . Therefore, a smooth or faceted groove profiles will grow with  $t^{1/4}$  kinetics until they interact with surface facets or until other facets nucleate on the groove; a reduced grooving rate and possibly a different time dependence are then expected. Finally, if  $\gamma$  is the anisotropic but the minima in the  $\gamma$ -orientation plots are not cusps, then distorted profiles evolve with effects similar to those discussed for  $\alpha' < \alpha < \beta$ .

#### 4. Variability in the Groove Width Due Only to Anisotropy in $D_s$

In the previous sections it was shown that rather substantial changes in the thermal grooving rate and profile shape could occur upon faceting due to anisotropy in  $\gamma$ , depending also on the relative diffusion coefficient on the facet plane. Even if anisotropy were present only in the surface

diffusivity (isotropic  $\gamma$ ), variable grooving rates and distorted profiles also result. As an example, consider the groove profile for isotropic surface energy shown in Figure 36a. If  $D_s = \infty$  over region 2, then  $\partial\mu/\partial x = 0$  and the curvature over this segment of the surface is constant yielding a constant, positive value of  $(\mu - \mu_0)$ . Since  $(\mu - \mu_0)$  is fixed at the groove root and the flat grain surface, the  $\partial\mu/\partial x$  over regions 1 and 3 is increased. Therefore, an increased rate of thermal grooving and a distorted, but not faceted, profile result. If  $D_s \approx 0$  over region 2, a small amount of mass is transported across point Q' and the gradient in curvature across region 1 relaxes. The value of  $(\mu - \mu_0)$  is positive, approximately constant, as in region 1 in Figure 36d. The gradient in curvature across region 3 also relaxes by transport of matter in a positive x-direction. This results in a large change in the radius of curvature between points Q' and P', i.e.,  $\nabla_s K$  is large over region 2. Consequently, the amount of surface, where  $D_s = 0$ , is small and the net effect on the grooving rate is small. However, the groove profile will appear distorted, as noted above.

Anisotropy in the direction of surface diffusion on clean Ni (110) surfaces has been reported by Bonzel and Latta (1978). The experiments consisted of measuring the decay of periodic profiles in situ by a laser diffraction technique using LEED and Auger electron spectroscopy to monitor the surface structure and composition, respectively. At temperatures of  $0.68 T_{mp}$ , diffusion in the [001] and  $[1\bar{1}0]$  directions have the same activation energy and magnitude. At temperatures below this, diffusion in the  $[1\bar{1}0]$  direction becomes relatively larger in magnitude with a lower activation energy as compared to that in the [001] direction. Surface diffusion in [001] direction is characterized by a single activation energy value over

the entire temperature range,  $0.58-0.91 T_{mp}$ ; at  $0.58 T_{mp}$  a factor of 10X difference in the diffusivities is found. The extent to which similar features exist on other planes and complex surfaces is not known.

##### 5. Impurity Effects on the Surface Tension and Diffusivities

For a pure crystalline material, low surface energy orientations exist which are related to its crystallography. These low energy planes are commonly represented as cusps on polar plots of surface energy versus orientation, where a cusp is characterized by  $\partial^2 \gamma / \partial \phi^2 = \infty$  and the ratio of the surface energy of orientations with high surface energy to those with low energy reflects the degree of anisotropy. Upon the addition of impurities, it is anticipated that the high energy orientations are decreased proportionally more than the low energy planes, and that  $\partial^2 \gamma / \partial \phi^2$  becomes finite, although it retains a "cusp-like" character. At high impurity concentrations,  $\partial^2 \gamma / \partial \phi^2$  may be decreased to an insignificant level (termed blunting of the cusp) and the net anisotropy is also further reduced. Although the effects of impurities on  $\gamma$  for oxide systems have not been documented, similar behavior is expected with a maximum reduction in  $\gamma$  of the order of 2-3X. [For further general discussion of this matter, see Winterbottom (1973) and Bonzel (1973)].

For metals, the segregation to or adsorption of impurities on the free surface has been found to both increase and decrease the surface diffusion coefficient depending on the interaction of the impurity with the surface atoms [Bonzel (1973)]. Reports of an enhancement or depression of  $\omega D_s$  by as much as a factor of 100X have been cited for  $T < 0.75 T_{mp}$ . At larger relative temperatures, Gjostein (1967) has shown that many fcc metals are characterized by a sharp increase in the activation energy at approximately  $0.75 T_{mp}$  on plots of the surface diffusion coefficient against

$T_{mp}/T$ . A surface diffusivity of approximately  $10^{-7} \text{ m}^2/\text{sec}$  ( $10^{-3} \text{ cm}^2/\text{sec}$ ) is typical at the melting point. Recent data on clean surfaces of some of these fcc metals, as reported in a review by Rhead (1975), show only the higher activation energy branch of  $\omega D_s$  versus  $1/T$  curves suggesting that impurities are linked to lower activation energy, relatively enhanced surface diffusion in the low temperature regime. However, Bonzel and Latta have reported a temperature dependent anisotropy in the surface diffusion coefficient based solely on the direction of diffusion on clean Ni (110) surfaces, as noted above. It is difficult, therefore, to use the existing data base on metals for even a qualitative understanding of the relative importance of small concentrations of impurities versus anisotropy on the surface diffusivities, although these are likely to be coupled.

For nonmetallic materials, the data base is limited. Coblenz (1981) has found that boron additions to silicon decrease the surface diffusion coefficient by several orders of magnitude. For aluminum oxide, Robertson and Ekstrom (1969) reported that additions of both CaO and SiO<sub>2</sub> to the surface increased the thermal grooving rates on some boundaries but not all; additions of Na<sub>2</sub>O and/or SiO<sub>2</sub> has no effect on the rate. Henrichsen (1973) found Ca, Si, and Ta surface impurities on all thermal grooving samples; larger grooving rates were noted where the concentrations were higher, but exact amounts were not stated. However, the implied  $\omega D_s$  values from their uncontaminated MSS experiments are 4X lower than those deduced from the GBG experiments. Monty and Duigou (1981) have reported that MgO decreases the rate of scratch decay at 1650°C and therefore, the surface diffusivity; at 1700°C, no effect was noted. These results, however, are open to alternative interpretations based on complications due to faceting, and the fact that surfaces may have been contaminated from the

furnace.

Exactly how impurities affect the surface diffusivity is not known, but they may modify  $\omega D_s$  by: attachment to kinks and ledges allowing adatoms to avoid these trapping locations, or alternatively, poisoning sources and sinks of defects, by enhancing surface disorder, and by altering the defect chemistry on the surface by forming complexes or by fixing the concentration of particle defects.

The effect of impurities on the lattice diffusion coefficient may be considerable for only a small addition to the  $Al_2O_3$  lattice, as discussed in Appendix I.

#### B. Dihedral Angles

It is interesting to note that the range of measured dihedral angles is approximately the same on both the ADL and Lucalox materials. This agreement implies that impurities affect both the boundary and surface tensions and the torque terms in proportions that keep the dihedral angles nearly unchanged. Furthermore, the presence of asymmetric dihedral angles on both materials indicates that anisotropy in the surface energies and therefore torque terms are present; the distorted profiles for both the ADL and the LD materials suggest that these effects are rather large.

#### C. Interpretation of High Temperature Grooving Behavior ( $T > 1500^\circ C$ )

The results of the experiments on ADL samples at  $1600^\circ C$  (GBG29) show that: (a) groove widths are less than on LD samples for times greater than 10 hours, (b) the grooving rates are variable from boundary to boundary, (c) straight line representations of the individual data sets intersect, (d)  $d \log W/d \log t \ll 1/4$ , (e) the groove profile shapes and grain surfaces are extensively faceted, and (f) there is poor agreement between the measured and calculated dihedral angles. The slow grooving rate and low time



dependence may be explained by late facet development with either slow diffusion on the facet ( $\Lambda \neq 0$ ) or slow facet translation.

The smaller spread in the observed thermal groove widths, compared to experiment GBG27, implies that the grooving process is more uniform on these samples. Such behavior may be indicative of a small range of exposed surface orientations. Recall that these samples are sapphire tubes with only a few grains per sample. Almost all boundaries between adjacent grains extend from the inner to the outer surface; therefore, the length of these grain boundaries are several hundred microns across the wall thickness of the tube. Since the thermal expansion of aluminum oxide is anisotropic, small grain misorientations are necessary to prevent fracture. A small set of grain misorientations then results in a limited set of surface orientations.

The results of experiments on Lucalox at 1600°C (GBG27) show that: (a) grooving rates are variable from boundary to boundary, (b) straight lines adequately represent most individual data sets with  $d \log W/d \log t$  within the range of 1/4 to 1/3, Figure 31, (c) few of these lines cross during the time of the experiments, (d) many profile shapes are distorted, (e) surfaces remained relatively free from faceting, (f) dihedral angles are variable, and (g) second phases are inhomogeneous in composition and distribution. These results indicate that thermal grooving is anisotropic on these samples and that as a result the profile shapes are distorted but remained reasonably self similar with time. They suggest that both surface and lattice diffusion are contributing to the process.

For lattice diffusion kinetics to be observed in the upper portion of the band of groove widths in Figure 31, the surface diffusivity must be characteristic of the thermal grooving rate found in the lower portion of

the band, where  $d \log W/d \log t = 1/4$ . Lattice diffusion kinetics for grooving in the lower portion of the band require that the surface diffusivity be less than that implied by any measured grooving rates; were this the case, the band of calculated  $\omega D_s$  values would extend to even lower values. However, changes in the grooving rate (and therefore  $d \log W/d \log t$ ) could be caused by the evolution of a profile shape change; this could result from segregating impurities. Additionally, the magnitudes of the implied  $D_L$  values for  $T > 1500^\circ\text{C}$  are at least 2X larger than those deduced from creep studies on similar materials [Cannon and Coble (1975)]. Large lattice diffusivities could be present if a significant amount of impurity with a valence of  $2^+$  or  $4^+$  were present [Hollenberg and Gordon (1973) and Lessing and Gordon (1977)]. In addition, large increases in the steady state creep rate have been measured for alumina co-doped ( $> 500$  ppm) with both  $2^+$  and  $4^+$  ions [Lessing and Gordon (1977)]. However, it is unlikely that impurities would be so localized along specific boundaries; enhanced grooving rates should be observed in regions several grains in diameter. Also, the results of McAllister and Cutler (1972) show that a significant level of doping was necessary before lattice diffusion contributed to grooving. It is therefore concluded that for the Lucalox materials lattice diffusion does not provide a significant contribution to thermal grooving for most boundaries at the groove sizes investigated; surface diffusion is the primary mass transport mechanism. For the pure materials, the implied lattice diffusivities are also too large; evidently, lattice diffusion is unimportant.

The variability in  $\gamma \omega D_s$  calculated from the observed grooving rates is not surprising in light of the nonuniform concentration of surface impurities and the anisotropies in this material as indicated by the distorted profiles. The variability is consistent with other reported thermal grooving data; considerable scatter in the plots of the average groove width

versus time was found for the studies resulting in lines 3, 4, 5 and 14 in Figure 1. The extent to which faceting is important on these studies is unknown but the groove profiles were commonly asymmetric indicating anisotropy in the  $\gamma\omega D_s$  product.

A difference of 2X in the minimum and maximum grooving rates where  $d \log W/d \log t = 1/4$  corresponds to a 16X variability in the  $\gamma\omega D_s$  product. The variability in the  $\gamma\omega D_s$  product is less than 16X because the coefficients  $A_i$  in Eq. (31) vary due to the distorted groove profiles. This can have a significant effect since the calculated  $\gamma\omega D_s$  is proportional to  $A_i^{-4}$ . However, the profile would not be distorted unless  $\gamma$  varied with orientation. It seems unlikely that  $\omega D_s$  would be constant when  $\gamma$  is variable.

At 1600°C and 1840°C, the thermal grooving rates for the LD material are greater than those of the BK and ADL materials. The surfaces of the LD samples remained relatively smooth during grooving; the BK and ADL samples developed facets. Further, after only one hour at 1600°C the groove sizes were nearly equal for the pure and Lucalox samples. These differences suggest that the presence of higher levels of Mg, Si and Ca prevents the formation of facets and that facets have low surface diffusion. However, the lowest calculated surface diffusivity at 1600°C is from the MSS samples where the profile was nearly sinusoidal, the  $(11\bar{2}3)$  surface by Henrichsen (1973). Therefore, low surface diffusivities are possible on "clean," nonfaceted surfaces.

The development of faceting should not result in lower implied  $\omega D_s$  values unless facet translation is rate limiting or diffusion on the facet is slow (small  $\Lambda$ ), as discussed earlier in relation to Figure 35 and 36. The results of this study, and those previously reviewed indicate that cleaner surfaces have lower effective surface diffusivities at  $T > 1500^\circ\text{C}$ .

However, all the measurements on clean sapphire surfaces [Huang et al., (1975), Shackelford and Scott, (1968), Achutaramayya, (1972), and possibly Robertson and Ekstrom (1969)] indicate only a 10X spread in the diffusivities on different surfaces. The transport rates on expected facet planes do not give the lowest diffusivities, although neglect of the  $\gamma''$  terms in analysis of the MSS experiments may cause this ranking to be erroneous. Thus, there is no unambiguous evidence for  $\Lambda=0$  on facet planes for pure surfaces. This suggests that facet translation, diffusion around corners, or boundary migration is the difficult step causing  $d \log W/d \log t \approx 1/6$  to  $1/20$  for the ADL samples.

For the MgO-doped ADL samples (GBG32), no significant change was noted in the grooving rate or extent of faceting on the grooves, as compared to undoped ADL samples. By comparison, enhanced surface diffusion is found for Lucalox material with Mg, Si and Ca on the surfaces. Apparently more than one impurity is necessary for such enhancement. This is consistent with Robertson's (1969) intentional doping with CaO and SiO<sub>2</sub>, discussed previously.

#### D. Interpretation of Grooving Behavior for Low Temperatures ( $T < 1500^\circ\text{C}$ )

In the temperature range of 1400-1500°C, only Lucalox materials were annealed. The ranges of implied diffusivities for these samples are larger than those at 1600°C. This fact is consistent with the development of faceted groove profiles leading to a broader range of groove widths. The distribution of the  $\log \omega D_s$  values calculated from the individual groove widths (using the average of the extremes in assignable width for each groove) is approximately normal within this range and similar to the distribution at 1600°C. This suggests that the best estimate of the "average diffusivity" is at the center of the band of  $\omega D_s$  values.

This is the temperature range where lattice diffusion apparently has a significant contribution, as indicated by the agreement of the band of implied  $D_L$  values with an extrapolation of  $D_L^{\text{creep}}$  [Cannon and Coble (1975)]. Note however, that the band of implied  $D_L$  values extends below the extrapolated line. This suggests that the variability in grooving rates is largely caused by the orientation dependence of  $\gamma$  and the geometry coefficient  $A$ , not by a variability in the diffusivities. The growth of small groove widths is probably controlled by surface diffusion; at larger groove widths, lattice diffusion is the primary mass transport mechanism.

In general, the thermal grooving behavior below 1400°C shows that:

- (a) the bands of implied diffusivities are larger than at higher temperatures;
- (b) there is no systematic variation of the magnitude of the implied diffusivities with sample purity level;
- (c) groove widths near the limit of resolution in the SEM are usually those giving low magnitudes of  $\omega D_s$  and usually narrow ranges in  $\log \omega D_s$ ;
- (d) the samples where second phase precipitated along boundaries gave lower magnitudes for the  $\omega D_s$  values;
- (e) the tendency for surface faceting increased with lower temperature, higher purity samples, and with less assurance that MgO is on the surface;
- (f) faceting is observed when the groove width is  $> \sim 0.25 \mu\text{m}$  for samples where second phase was not exsolved along boundaries; for the latter samples, no faceting was observed; and
- (g) for widths near the limit of resolution, it is not possible to distinguish whether faceting or asymmetric profiles are present.

In this low temperature regime: (a) lattice diffusion is not an important mass transport mechanism; the extrapolated  $D_L^{\text{creep}}$  intersects only the lowest values of the implied  $D_L$  ranges; (b) many impurities are above their solubility limit; (c) however, at the lower temperatures

appreciable time is required to bring these impurities/dopants to the polished surface by lattice diffusion (or from a combination of boundary and surface diffusion) or by vapor transport from the packing powders; and (d) a strong anisotropy in  $\gamma$  is present as evidenced by the faceting. Given all these contributing factors, it is concluded that thermal grooving for all samples at temperatures below 1400°C is dominated by complex impurity/orientation interactions.

#### E. Summary of the Surface Diffusivities

For the high temperature grooving data, lines representing the best estimates of the surface diffusivity for the pure and Lucalox materials are shown in Figure 38. The activation energy for the pure materials is 120 to 130 kcal/mole, for the Lucalox material, 160 to 170 kcal/mole. In the low temperature regime, a band defined by lines with an activation energy of  $\sim 65$  kcal/mole adequately represents all samples. The actual magnitude for  $\omega D_s$  may be quite orientation and composition specific. These activation energies compare with 114 to 140 kcal/mole for lattice diffusion, and  $\sim 100$  kcal/mole for boundary diffusion of Al [Palodino and Kingery (1962), Cannon and Coble (1975), Hollenberg and Gordon (1973), and Lessing and Gordon (1977)]. Extrapolating these lines to the melting point yields  $D_s$  values ( $\omega = \Omega^{1/3}$ ) of  $\sim 10^{-6}$  cm<sup>2</sup>/sec and  $\sim 10^{-4}$  cm<sup>2</sup>/sec for the pure and least pure materials. These values are less than that observed for fcc-metals,  $10^{-3}$  cm<sup>2</sup>/sec [Gjostein (1967), Bonzel (1975)].

The surface diffusivities calculated from the thermal grooving data are extremely variable, especially at lower temperatures. The variability extends beyond a presumed maximum of  $\sim 3X$  in  $\gamma$ . It is not possible to determine the actual variability in  $\omega D_s$  because the numerical coefficient

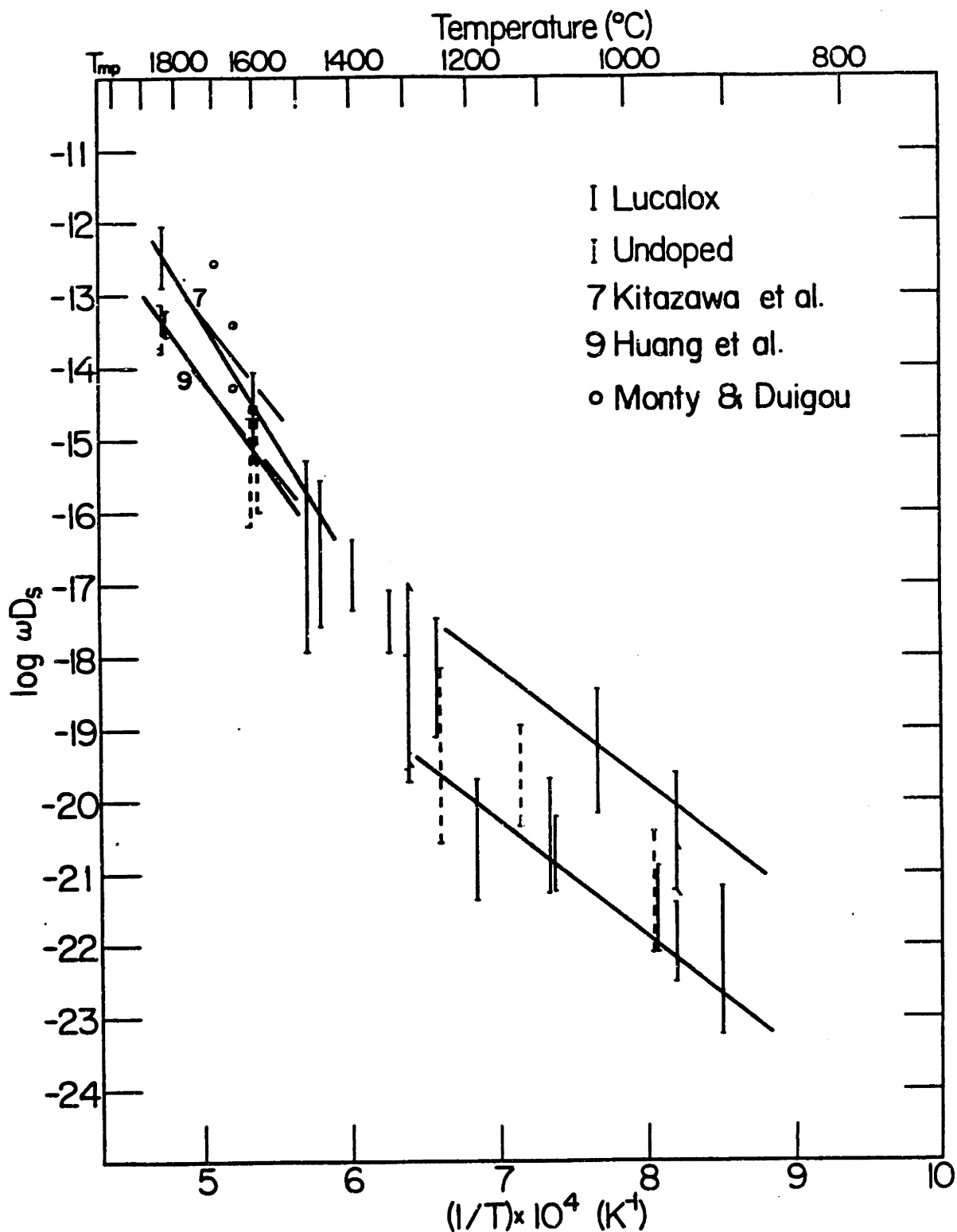


Figure 38 - Log  $\omega D_s$  versus  $1/T$ . Lines represent estimates for  $\omega D_s$ : for  $T > 1500^\circ C$ ,  $\Delta H(\text{pure}) = 125 \text{ kcal./mole}$ ,  $\Delta H(\text{Lucalox}) = 165 \text{ kcal./mole}$ ; for  $T < 1300^\circ C$ ,  $\omega D_s$  lies within a band defined lines with  $\Delta H = 65 \text{ kcal./mole}$ .

is  $\sim 5X$ , based on the range of  $W/W_{iso}$  for various facet orientations (Figure 35). A 5X difference in  $A_i$  corresponds to a 625X variability in  $\omega D_s$ . Thus, the variability in  $A_i$  could account for the ranges in the calculated  $\omega D_s$  values. The observed groove profiles do not exhibit characteristics indicative of such extremes in the  $A_i$ -values, particularly at the higher temperatures (small  $|\alpha|$ , i.e., a facet plane nearly parallel to the sample surface). The groove profiles are often distorted only slightly where surfaces are smooth; further, the occurrence of both half-groove widths with either very small or very large  $W/W_{iso}$  values is infrequent. A better estimate for the variability in  $A_i$  is 2X, resulting in a possible 16X variability for  $\omega D_s$ . This variability in  $A_i$  could account for the ranges in  $\omega D_s$  at the higher temperatures, but not at the lower temperatures.

#### F. Dependence of Faceting on Impurities and Temperature

The presence of excess MgO in the embedding powder reduced the degree of faceting on LTVA samples. The following is an interesting example showing this. Less faceting was observed on the samples where MgO was added to the alumina embedding powder (GBG12); this sample presumably contained less magnesia and other impurities due to its longer annealing in vacuum at high temperature and slower cooling rate. More faceting was observed on the samples where no MgO was added to the alumina powder; these samples were annealed for longer time. However, the longer annealing time should not influence the result if facets develop in proportion to  $t^{1/4}$ , e.g., the relative facet size for the shorter time is  $(t_1/t_{TOTAL})^{1/4} = (1/3)^{1/4} = 0.76$ . Instead of observing smaller facets when excess magnesia is present at the shorter time, the surfaces are smoother (linear faceting rather than choppy networks are often present).



In general, the amount of faceting depends on the impurity level of the sample and the annealing temperature. For the samples with the highest impurity levels (the LD material), little faceting was noted down to the lowest temperature used, 1092°C; in fact, considerable amounts of second phase were exsolved at the lower temperatures. For the purest samples (ADL material) faceting was observed at all temperatures, even where the material was doped with MgO (GBG32). For a material with an intermediate impurity level (BK material), the amount of faceting was decreased by increasing the annealing temperature, [compare GBG29 (1600°C) with GBG31 (1840°C)].

At higher temperature for the freely evaporating samples, relatively smooth surfaces and raised thermal groove profiles were noted. Such profiles have been observed in other doped materials under nonequilibrium conditions between the solid and vapor. Coblenz (1981) found a similar behavior for B-doped Si. Allen (1966) observed such profiles for Mo-33Re at 2200°C and for W-25Re at 3000°C. Presumably this raised profile is caused by a reduction in the evaporation kinetics near the grain boundaries by the interactions of dopants or impurities with kinks and ledges; this assumes that the surface concentrations of the impurities or dopants are increased due to fast transport of these by boundary diffusion. Winterbottom (1973) has reported that hillocks on the surfaces of freely evaporating Ag are due to clustering of impurities. Further documentation of these effects using Auger electron spectroscopy is necessary and can, in principle, yield information on the shape of the  $\gamma$ -plot and its dependence on surface impurities.

### G. The Role of Surface Diffusion in Initial Stage Sintering

In a recent review of the initial stage sintering mechanisms by Dynys et al. (1979), Appendix I, it was concluded that the boundary diffusivity deduced from steady state creep [Cannon and Coble (1975)] is the only plausible (and reliably known) diffusion mechanism which could account for the observed shrinkage of alumina powder compacts; lattice diffusivities are too low. Those boundary diffusivity data are also used here to evaluate the importance of surface diffusion as a contributint or controlling initial stage sintering mechanism.

There are three ways in which surface diffusion may contribute to initial state sintering when the only other operative mechanism is boundary diffusion: (1) If  $\omega D_s > 8\delta D_b$ , then coarsening by surface diffusion is the dominant transport mechanism [based on the best set of models, as reviewed by Coblenz et al. (1979)]. (2) If  $\omega D_s \lesssim 0.05 \delta D_b$ , then surface diffusion will limit the redistribution of mass transported to the surface by boundary diffusion, i.e., shrinkage is controlled by surface diffusion [Coblenz (1981)]. (3) If  $8\delta D_b > \omega D_s \gtrsim 0.05\delta D_b$ , then boundary diffusion is the dominant and controlling sintering mechanism. Using these criteria, lines defining these regimes are drawn on a plot including the implied  $\omega D_s$  values, Figure 39. For  $\omega D_s$  values above the  $\omega D_s / \delta D_b$  line, coarsening by surface diffusion is the dominant sintering mechanism; for  $\omega D_s$  values below the  $\delta D_b / SRC$  line, surface redistribution control (SRC) by surface diffusion controls sintering; between these lines, boundary diffusion is the dominant transport mechanism.

The results of this study show that for  $T \geq 1600^\circ\text{C}$  or  $T < 1100^\circ\text{C}$  boundary diffusion is the dominant initial stage sintering mechanism. For  $1100 < T < 1400^\circ\text{C}$ , surface redistribution controlled sintering may occur for

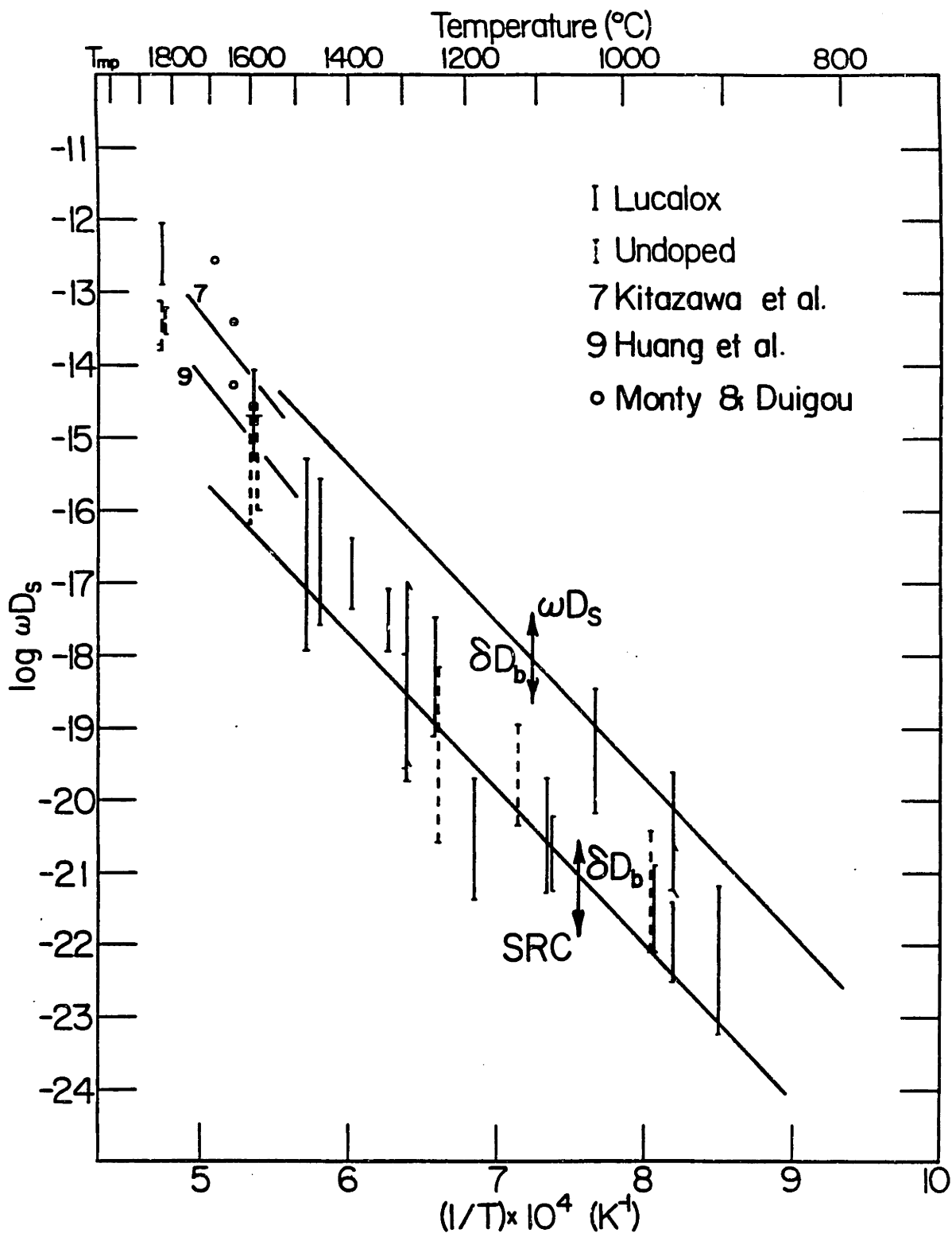


Figure 39 -  $\log \omega D_s$  versus  $1/T$ . Lines separate regimes for: coarsening by surface diffusion ( $\omega D_s$ ), shrinkage by boundary diffusion ( $\delta D_b$ ), and surface diffusion redistribution controlled shrinkage (SRC).

orientations or compositions where  $\omega D_s$  is slow; for orientations or compositions where  $\omega D_s$  is higher, boundary diffusion is again the dominant transport path in sintering. Note with respect to the uncertainty in  $\omega D_s$ , these trends would hold regardless of where a line is drawn in the low temperature regime.

In a previous work (Appendix I), it was noted that for  $T < 1500^\circ\text{C}$  neck growth in large spheres was slower than predicted by boundary diffusion. Data for shrinkage of powder-compacts (Figure 40) shows that, in some cases, the rates are very similar to those predicted by boundary diffusion and in others the rates are much lower. These low shrinkage rates have been attributed to the adverse effects of competitive coarsening by surface diffusion [Johnson (1971)]. The present results suggest that surface diffusion is not large enough to cause the low shrinkage rates, i.e.,  $\omega D_s / \delta D_b < 8$  for all temperatures. It is also of interest that the surface diffusivities determined from surface area reduction (not permeability change) on classified powders agree with those deduced from thermal grooving, but the rates of surface area reduction are less than anticipated if boundary diffusion were also considered. These results suggest that for fine powders as well as the large spheres, boundaries may not always act efficiently as point defect sources or sinks, as suggested in Appendix I. The creep data on fine grained  $\text{Al}_2\text{O}_3$  [Cannon, Rhodes and Heuer (1981)] also suggests that boundary sliding or point defect annihilation is sometimes rate controlling.

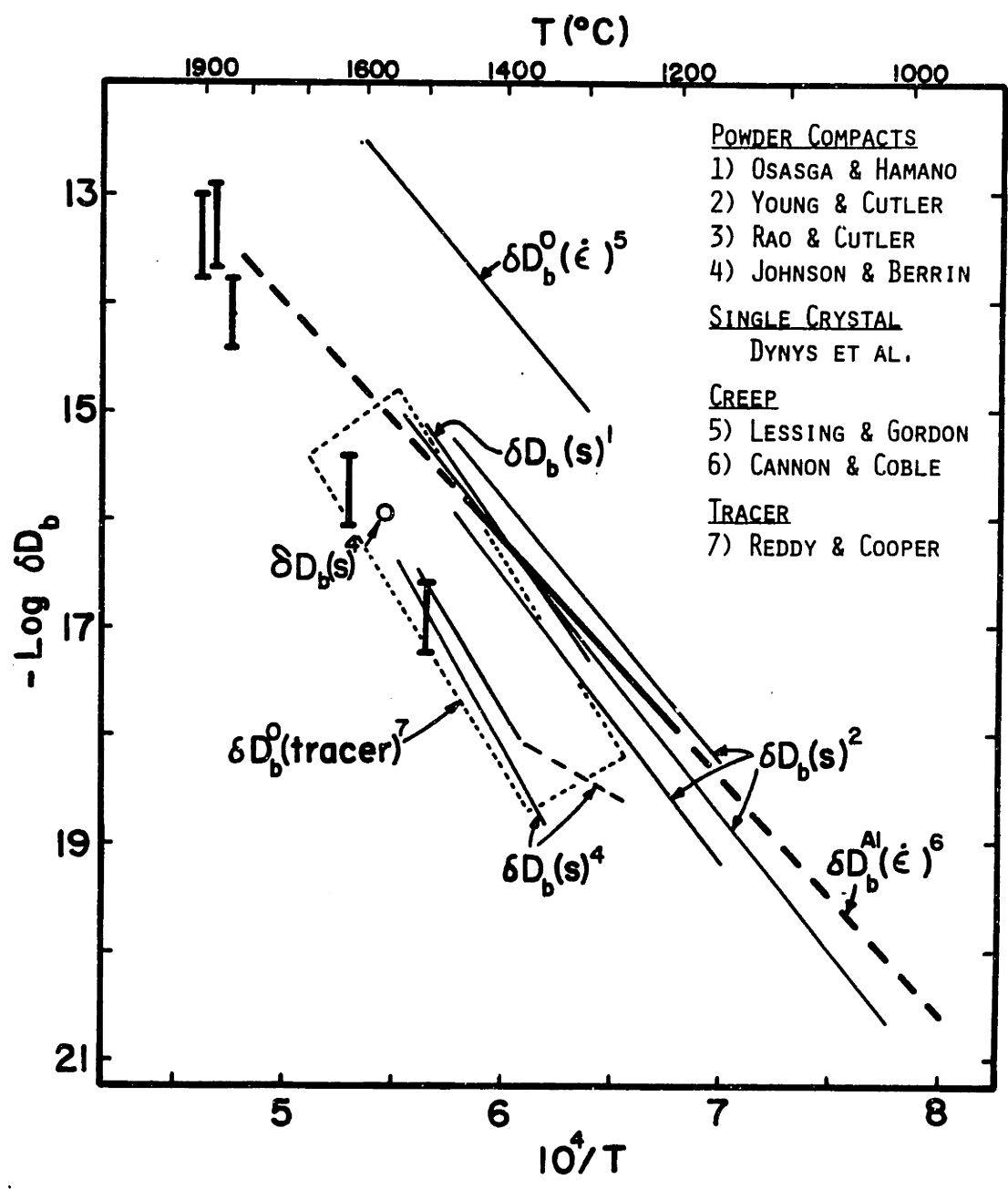


Figure 40 - Log  $\delta D_b$  versus  $1/T$

### VIII. CONCLUSIONS

1. Thermal grooving at grain boundaries for the  $\text{Al}_2\text{O}_3$  materials studied occurs primarily by surface diffusion. This is indicated by the magnitudes of the grooving rates and by the time dependence for material for which there is no significant faceting on the groove profiles. The next most important alternative mass transport mechanism is lattice diffusion. Based on a comparison of the implied  $D_L$  values with literature values for Lucalox materials, lattice diffusion may make an appreciable contribution at larger groove widths in the temperature range of 1400 to 1500°C.

2. The thermal grooving rates are variable for all samples annealed between 900 and 1840°C; the variability is attributed primarily to the orientation dependencies of  $\gamma$  and  $\omega D_s$ , although impurity effects may also be important. The variability increases with decreasing temperature.

3. The surface diffusivities calculated from the thermal grooving data are extremely variable. This variability results from using models assuming isotropic surface energy and surface diffusivities. The coefficient ( $A_i$ ) in the grooving models depends on orientation dependencies of  $\gamma$  and  $\omega D_s$ . The variability in  $A_i$  could account for the variability in the calculated  $\omega D_s$  values.

4. At 1600°C, the time dependence for the grooving of the undoped ADL samples is  $d \log W/d \log t \approx 1/6$  to  $1/20$ . This results because the groove morphology is changing due to faceting and indicates that either slow diffusion on the facet plane or that facet translation (adding atom layers to or subtracting layers from the facet plane) is the rate controlling process.

5. At 1600°C and 1840°C, the presence of Mg, Si, and Ca on the surface enhances the surface diffusivities.

6. The implied  $D_s$  values are non-Arrhenius. At the lower temperatures, ( $<1300^\circ\text{C}$ ) an activation energy of  $\sim 65$  kcal/mole adequately represents the results for all materials studied; at higher temperatures ( $>1400^\circ\text{C}$ ),  $\sim 125$  kcal/mole represents the results in the pure materials, and an activation energy of  $\sim 165$  kcal/mole fits the results for the Lucalox materials.

7. The development of faceting is decreased for higher impurity levels and higher temperature.

8. For Lucalox samples, the tendency for faceting was decreased by preventing the loss of magnesia.

9. At  $1600^\circ\text{C}$ , magnesia doping by itself does not prevent faceting in otherwise pure materials. Comparison with Lucalox materials indicates that the presence of additional impurities, such as calcia and silica, is necessary to decrease faceting.

10. Based on boundary diffusivity data from creep experiments [Cannon and Coble (1975)] and this surface diffusivity data, the initial stage sintering of  $\text{Al}_2\text{O}_3$  occurs by boundary diffusion below  $1100^\circ\text{C}$  and above  $1500^\circ\text{C}$ ; in the temperature range  $1100$  to  $1400^\circ\text{C}$ , surface redistribution (of matter transported by boundary diffusion) could control sintering for orientations or sample compositions with low surface diffusivity.

## IX. SUGGESTIONS FOR FUTURE WORK

- (1) Determination of the low energy planes for  $\text{Al}_2\text{O}_3$ .

Experiments need to be done under near-equilibrium conditions thereby avoiding free evaporation or rapidly changing shapes. It is anticipated that useful information could be obtained by: (a) indexing the planes that develop from thermal faceting; methods for indexing include x-ray techniques, and electron channeling (Choates) patterns (information could also be deduced from the orientations of the facets with respect to the initial surface of a crystallographic direction in the plane of the initial surface is known), and (b) study of the orientations of faceted pores entrapped within single grains using the TEM.

- (2) Effects of various facet planes on thermal grooving kinetics.

With prior knowledge of which planes form facets, and by knowing the orientations of both grains, the effects of facets on thermal grooving kinetics could be documented.

- (3) Accurate measurement of dihedral angles and the amount of asymmetry near the groove root.

- (4) Simultaneous measurement of surface area reduction and shrinkage for powder compacts composed of a reasonably spherical, very narrow size distribution powder.

For uniformly-packed compacts, useful information about the relative magnitudes of the surface and boundary diffusivities could be measured. By adding detailed neck size measurements, the absolute magnitudes of diffusivities could be inferred.



REFERENCES

- Achutaramayya, G. (1972), Doctoral Thesis, University of Washington.
- Allen, R.C. (1966), Trans. AIME, Vol. 236, 915.
- Amelinckx, S. (1953), Physica, 19
- Blendell, T. E. (1979), Ph.D. Thesis, Massachusetts Institute of Technology.
- Bonzel, H.P. (1973) in "Structure and Properties of Metal Surfaces," 248.
- Bonzel, H.P. and Latta, E.E. (1978), Surf. Sci., 76, 275.
- Cannon, R.M., Rhodes, W.H. and Heuer, A.H. (1980), J. Am. Ceram. Soc. 63. 46.
- Coble, R.L. (1961), J. Appl. Phys., 32, 793.
- Coblentz, W.S., Dynys, J.M., Cannon, R.M. and Coble, R.L. (1980) in "Sintering Processes," Materials Science Research, Volume 13.
- Davis, L.E., MacDonald, N.C., Palmberg, P.W., Riach, G.E. and Weber, R.E. (1976), Handbook of Auger Spectroscopy, Physical Electronics Industries.
- Feingold, A.H., and Li, C.Y. (1968), Acta Met., 16, 1101.
- Gjostein, N.A. (1967), in "Surfaces and Interfaces, I," Syracuse Univ. Press.
- Gjostein, N.A. (1970), Met. Trans., 1, 315.
- Gjostein, N.A., and Rhines, F.N. (1959), Acta Met., 7, 319.
- Gupta, T.K. (1978), J. Am. Ceram. Soc., 61, 191.
- Hearle, J.W.S., Sparrow, J.T., and Cross, P.M. (1972), "The Use of SEM," Pergamon Press.
- Henrichsen, R.A. (1973), Ph.D. Thesis, Cornell University.
- Herring, C. (1951), Physics of Powder Metallurgy, 143.
- Hollenberg, G.W., and Gordon R.S. (1973), J. Am. Ceram. Soc., 56, 140.
- Huang, F.H., Henrichsen, R.A., and Li, C.Y. (1975), in "Sintering and Catalysis."

- Johnson, W.C., and Coble, R.L. (1978), J. Am. Ceram. Soc., 61, 110.
- Johnson, W.C. and Stein, D.F. (1975), J. Am. Ceram. Soc., 58, 485.
- King, R.T., and Mullins, W.W. (1962), Acta Met., 10, 601.
- Kitazawa, K., Komaki, I., Matsukawa, K., and Fueki, K. (1979), J. Jap. Ceram. Soc.
- Latta, E.E. and Bonzel, H.P. (1977), Phys. Rev. Letters, 38, 389.
- Lessing, P.A., and Gordon R.S. (1977), J. Mat. Sci., 12, 2291.
- Maruyama, T., and Komatsu, W. (1975), J. Am. Ceram. Soc., 58, 338.
- McAllister, P.V., and Cutler, I.B. (1970), Met. Trans., 1, 313.
- McAllister, P.V., and Cutler, I.B. (1972), J. Am. Ceram. Soc., 33, 351.
- Monty, C., and Duigou, J.Le (1981), to be published in High Temperature, High pressures.
- Moon, S., Yoo, K. and Kim, H. (1977). J. Korean Ceram Soc., 14
- Moriyoshi, Y. and Komatsu, W. (1973), Yogyo-Kyokai-Shi, 81, 103.
- Moriyoshi, Y. and Komatsu, W. (1976), Yogyo-Kyokai-Shi, 84, 348.
- Moriyoshi, Y. and Komatsu, W. (1978), Yogyo-Kyokai-Shi, 86, 130.
- Mullins, W.W. (1957), J. Appl. Phys., 28, 333.
- Mullins, W.W. (1960), Trans. AIME, 218, 354.
- Mullins, W.W. (1961), Phil. Mag., 6, 1313.
- Mullins, W.W. (1964), in "Metal Surfaces," Am. Soc. for Metals.
- Mullins, W.W. and Shewmon, P.G. (1959), Acta Met., 7, ;63.
- Nichols, F.A. and Mullins, W.W. (1965), J. Appl. Phys., 36, 1826.
- Nichols, F.A. (1976), J. Mater. Sci., 11, 1077.
- Paladino, A.E., and Kingery, W.D. (1962), J. Chem. Phys., 33, 480.
- Prochazka, S. and Coble, R.L. (1970), Phys. Sintering, 2, 15.
- Rao, W.R. and Cutler, I.B. (1972), J. Am. Ceram. Soc., 55, 170.
- Rhead, G.E. (1975), Sur. Sci., 47, 207.

- Rhodes, W.H., and Cannon, R.M. (1969), Summary Rept., U.S. Naval Air Systems, Contract N00019-69-C-0198.
- Robertson, W.M. and Chang, R. (1966), Materials Science Research, 3, 49.
- Robertson, W.M. and Ekstrom, F.E. (1969), Materials Science Research, 4, 273.
- Robertson,, W.M.(1971), J. Appl. Phys. 42, 463.
- Roy, S.K. and Coble, R.L. (1968), J. Am. Ceram. Soc., 51, 1.
- Shackelford, J.F., and Scott, W.D. (1968), J. Am. Ceram. Soc., 51, 688.
- Winterbottom, W.L. (1973), in "Structure and Properties of Metal Surfaces", Maruzen Co., 35.
- Yen, C.F. and Coble, R.L. (1972), J. Am. Ceram. Soc., 55, 507.
- Cannon, R.M. and Coble, R.L. (1975), "Deformation of Ceramic Materials," Plenum Press, N.Y.
- Dynys, J.M., Coble, R.L., Coblenz, W.S., and Canon, R.M. (1979), "Sintering Processes," Materials Science Research, Vol. 13, Plenum Press, N.Y.
- Johnson, D.L. and Berrin, L. (1967), "Sintering and Related Phenomena," Gordon and Breach, N.Y.
- Johnson, D.L. (1969), "Ultrafine-Grain Ceramics," Syracuse University Press.
- Oishi, Y. and Kingery, W.D. (1960), J. Chem. Phys. 33, 480.
- Osaga, and Hamano, Y. (1974), J. Jap. Ceram. Soc., 82, 239.
- Reddy, K.P.R. (1977), Ph.D. Thesis, Case Western Reserve University.
- Young, W.S. and Cutler, I.B. (1970), J. Amer. Ceram. Soc., 53, 659.

APPENDIX I

The material in this appendix was published in "Sintering Processes", Materials Science Research, Volume 13, Edited by G. C. Kuczynski, Plenum Press, New York, 1980, pages 391-404.

MECHANISMS OF ATOM TRANSPORT DURING  
INITIAL STAGE SINTERING OF  $Al_2O_3$

J. M. Dynys, R. L. Coble, W. S. Coblenz  
and R. M. Cannon

Ceramics Division  
Department of Materials Science and Engineering  
Massachusetts Institute of Technology  
Cambridge, MA 02139

ABSTRACT

Neck growth data from model experiments on  $Al_2O_3$  were analyzed assuming various initial stage sintering mechanisms. These results, along with mass transport coefficients reported in other studies, are used to deduce the probable transport paths. Sintering maps were constructed to delineate the ranges of temperature, particle size, and neck size over which surface diffusion, boundary diffusion, or lattice diffusion is dominant. Inconsistencies among the reported diffusion coefficients are defined and discussed.

INTRODUCTION

Many sintering studies have been conducted on alumina over the last twenty years. Although the sintering of alumina is generally thought to occur by solid state diffusion over most of the conditions of interest, there is no consensus regarding the dominant or rate controlling transport path. Furthermore, there are no adequate explanations for the effects of additives, such as  $MgO$ , on the sintering behavior of  $Al_2O_3$ . There are several reasons for this state of affairs: (1) disagreement has existed as to the "proper" sintering model for each transport path, (2) the data base for the mass transport coefficients is incomplete and unreliable, and (3) complications from size distribution effects, packing irregularities, and particle rearrangement make interpretation of sintering behavior of powder compacts difficult.

This paper is a companion to our Critical Review of the Initial Stage Sintering Models<sup>(1)</sup> in which the most appropriate model is identified for each transport path. In this paper the initial stage sintering behavior of  $\text{Al}_2\text{O}_3$  is examined. The neck growth from sphere-plate experiments from this and previous studies<sup>(2,3)</sup> is analyzed by using the various sintering models in an attempt to confirm the choice of models and identify the controlling sintering mechanisms in  $\text{Al}_2\text{O}_3$ . The results from these model experiments are used to calculate various apparent diffusivities ( $\omega D_s$ ,  $\delta D_b$ , and  $D_L$ )<sup>†</sup> which are then compared to transport data for  $\text{Al}_2\text{O}_3$ , taken from the literature and recent unpublished results. This data base comes from many different types of experiments, including tracer measurements and creep rate measurements for lattice and grain boundary diffusivities, and surface smoothing or grain boundary grooving experiments for surface and/or lattice diffusivities. Some inconsistencies are indicated by these comparisons which we attempt to resolve or put into focus by considering the implications with regard to observed sintering and creep behavior.

Several mechanisms for material transport are possible for initial stage sintering: vapor transport, dislocation motion, and lattice, surface or grain boundary diffusion. For initial stage sintering of  $\text{Al}_2\text{O}_3$ , vapor transport need not be considered because the vapor pressures<sup>(4)</sup> needed to dominate diffusive transport are much greater than those calculated from the thermochemical data for alumina under the experimental conditions used here. Ogbuji, et al.<sup>(5)</sup> have observed that dislocation formation and motion occurs during early stage sintering of micron sized alumina powders heated through a rapid firing cycle (1 hour) with a maximum temperature of  $1500^\circ\text{C}$ . Morgan<sup>(6)</sup> has also observed dislocations apparently formed during sintering. In contrast to these observations, Ashby<sup>(7)</sup> has predicted that the contribution from dislocation activity will be relatively small, and only exhibited in early transients. These studies indicate that the conditions under which dislocation motion contributes to sintering are not well understood or documented. Since observed particle size effects on the sintering rates support diffusional transport mechanisms, only surface, boundary, and lattice diffusion mechanisms are discussed here as potentially providing contributions to sintering in  $\text{Al}_2\text{O}_3$ . Analysis of diffusion controlled sintering is complicated by the requirement that both ions must be transported in a stoichiometric ratio between sources and sinks. The rate for any process will be limited by the slowest ion along its fastest path. Thus, in principle, several possibilities for the

---

<sup>†</sup>  $D_L^i$  = lattice diffusion coefficient of species i

$\delta D_b^i$  = boundary width-diffusivity product for species i

$\omega D_s^i$  = surface width-diffusivity product for species i

rate limiting process exist, i.e., either species along the boundary, surface, through the lattice or gas phase. For example, tracer diffusion studies<sup>(8,9,10)</sup> have shown that oxygen has a much lower lattice diffusivity than aluminum in  $\text{Al}_2\text{O}_3$ . Consequently, in order for either aluminum boundary or lattice diffusion to control the shrinkage process, oxygen boundary diffusion must be relatively rapid. In creep studies, fast boundary oxygen transport has been postulated to explain lattice diffusion controlled creep kinetics<sup>(11,13)</sup>. In sintering studies, however, lattice diffusion kinetics could be observed even when  $\delta D_b^O$  is small enough to control mass transport from the grain boundary. If  $\omega D_s^O$  is larger than  $\delta D_b^O$ , neck growth could be dominated by transport from the sphere surface which would be limited by  $D_L^{Al}$  or  $\omega D_s$ , and no shrinkage would occur.

Further difficulties arise in interpreting mass transport phenomena because of uncertainties regarding the effects of impurities on the diffusivities. Enhancement of  $D_L^{Al}$  by both divalent ( $\text{Fe}^{+2}, \text{Mg}^{+2}$ ) and tetravalent ( $\text{Ti}^{+4}$ ) additives has been postulated to explain increased diffusional creep<sup>(11,12)</sup> and sintering rates<sup>(14,15)</sup> observed for specific grain or particle sizes. In contrast, tracer measurements<sup>(10)</sup> of  $\delta D_b^O$  and values of  $\delta D_b^{Al}$  deduced<sup>(12)</sup> from creep rates of fine-grained  $\text{Al}_2\text{O}_3$  appear to be unaffected by Mg or Y additions. Values of  $\delta D_b^O$  have also been determined<sup>(11)</sup> from the transition from lattice to boundary diffusion controlled creep in iron oxide doped, large grain size  $\text{Al}_2\text{O}_3$ . These  $\delta D_b^O$  values are much larger than the results of the tracer measurements by Reddy. The major differences appear to result from the method of measurement and not simply from impurities. The surface diffusivity data do not indicate a significant dependence on cation impurities, except when a CaO-SiO<sub>2</sub> second phase is present which significantly increases the surface transport rate in localized areas.<sup>(16)</sup>

If the grain boundaries fail to operate as efficient sources and sinks for point defects, then the sintering rates would be lower than predicted by the models which assume diffusion control. There is evidence of imperfect boundary behavior in the creep of fine grained  $\text{Al}_2\text{O}_3$  ( $< 10 \mu\text{m}$ ).<sup>(17)</sup> However, this behavior can be explained either by imperfect source and sink operation or by difficult grain boundary sliding.

#### EXPERIMENTAL PROCEDURE

Sphere-plate model experiments were performed in a vacuum furnace equipped with tantalum heating elements and shields. Polished sapphire (3.0, 2.0, 1.0, and 0.40 millimeter diameter) and ruby (0.14 millimeter) spheres<sup>†</sup> were sintered at temperatures from 1500 to 1900°C at times from 0.6 to 70.0 hours. The spheres were held on

---

<sup>†</sup> Adolf Meller Company

a polished sapphire plate\* by means of a sapphire lamp tube\*\* which was covered by another sapphire plate. This sample enclosure, used to reduce vaporization effects, was placed over a partially sintered, coarse, high-purity alumina powder† held within a covered tungsten or alumina crucible. Doping with magnesium was accomplished prior to the sintering experiments by vapor phase exposure of the sapphire plates and balls to a two-phase mixture of spinel and alumina at the sintering temperature. Neck sizes and shapes were subsequently recorded by fracturing the spheres from the plate and then photographing the necks found on the plate. The neck patterns on a few spheres were examined and found to be mirror images of those found on the plate. Consequently, most observations were made only on the plates.

## RESULTS

In contrast to the radial neck growth assumed in modeling, irregular or faceted neck growth patterns were observed for all sphere sizes, Fig. 1. These irregular growth patterns may result from a neck surface instability which is perhaps analogous to dendritic growth instability. A micrograph of the smallest diameter spheres (0.135 mm), Fig. 1a, shows a somewhat faceted neck cross-section for the sphere-sphere case, while in the sphere-plate neck, the instability is more evident. Greater neck surface instability was found for smaller relative neck sizes and larger sphere sizes. This is seen in Fig. 1b for the largest spheres (3.0 mm). Here, a tendency for cross-growth between the fingers is evident with a resultant entrapment of pores on the grain boundary; this effect was found only for the larger spheres studied. Additionally, preferred growth directions are suggested because uniform spacings and lengths of the fingers are seldom observed. A high magnification micrograph of another finger growth area, Fig. 1c, shows the presence of faceted fingers indicating slow growing planes. These observations of the neck morphology suggest an anisotropy in  $\omega D_s$  and/or  $\gamma_{sv}$ .†

Another feature of neck growth, indicated by the bright ridge on the sphere surface adjacent to the neck surface in Fig. 1a, is undercutting. This is also clearly evident in Fig. 1c. Undercutting implies that either  $\omega D_s$  or  $D_L$  provides a major contribution to the sintering. (1)

One observation of the dihedral angle was made on a pair of spheres sintered together and cooled from 1870°C. The measured

---

\* (1120) Linde

\*\* A.D. Little

† Alcoa, XA-139

† The effect of the  $Cr_2O_3$  dopant in the ruby spheres was presumed to be negligible.



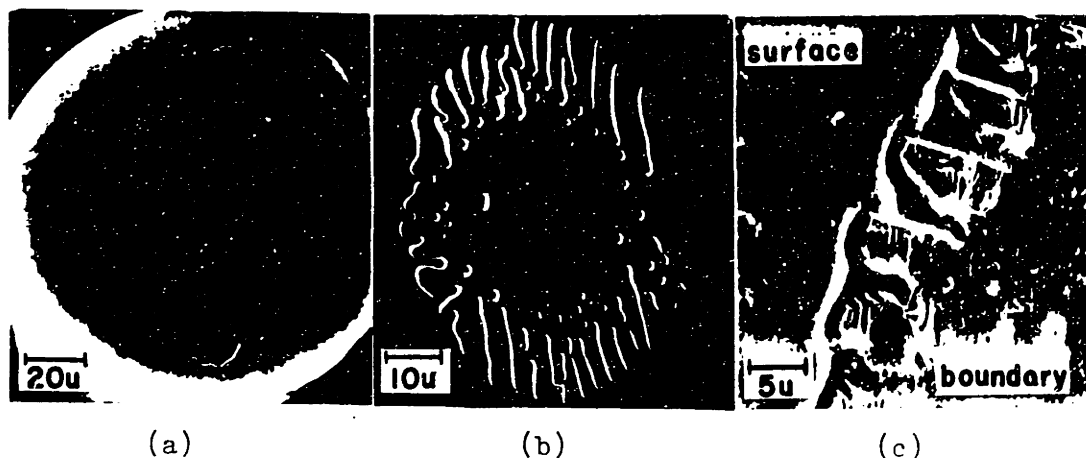


Fig. 1. Observed neck growth features, SEM micrographs:  
 a)  $(x/a) \sim 0.60$  for 0.14 mm, b)  $(x/a) \sim 0.017$  for 3.0 mm, and c) 3.0 mm.

angle was  $110^\circ$  which is less than the  $150^\circ$  dihedral angle usually quoted for  $\text{Al}_2\text{O}_3$ .<sup>(18)</sup>

Due to the neck surface instability, the data were analyzed in terms of normalized neck sizes,  $(x/a)$ , defined by the maximum (circumscribed) and minimum (inscribed) circle diameters observed for each neck. The  $(x/a)$  values obtained were between 0.002 and 0.230. Hence, for these neck sizes the small neck assumptions discussed by Coblenz, et al.<sup>(1)</sup> are valid. The variability in  $(x/a)$  for each neck precludes determination of an exact size or time dependence. However, by comparing the slopes of the results when plotted as either  $(x/a)$  versus time (for each sphere size) or  $(x/a)$  versus size (at constant times) the analysis reveals that either surface, boundary or lattice diffusion could be the dominant mechanism. That is, the data are adequately described by  $(x/a) \propto (t/a^4)^{1/6}$  or  $(t/a^3)^{1/5}$  with a slight preference for the first relation. We note that the data also fit  $(x/a) \propto (t/a^4)^{1/7}$  adequately but not as well as the previous two relations and are not well described by  $(x/a) \propto (t/a^3)^{1/4}$ ; this is consistent with the choice of surface and lattice models of Coblenz, et al.<sup>(1)</sup>

The data were subsequently converted to average diffusion coefficients with standard deviations.\* In all cases, we assumed that

\* The diffusivities were calculated from Eqs. (16), (24), and (31) of Ref. (1) except the coefficients  $K$  were corrected for the sphere-plate geometry:  $K(\text{surface}) = 116$ <sup>(19)</sup>;  $K(\text{boundary})$  and  $K(\text{lattice})$  of Eqs. (24) and (31), are increased by a factor of four which results from an increase of the curvature by a factor of two and decreasing the left side of Eq. (22) by a factor of two.

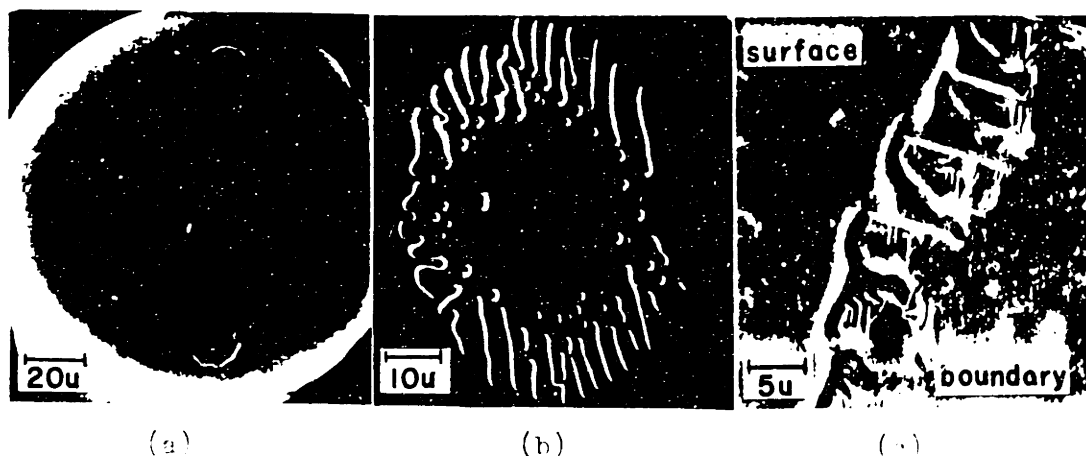


Fig. 1. Observed neck growth features, SEM micrographs: a)  $(x/a) \approx 0.60$  for 0.14mm, b)  $(x/a) \approx 0.017$  for 3.0mm, and c) 3.0mm.

angle was  $115^\circ$  which is less than the  $150^\circ$  dihedral angle usually quoted for  $Al_2O_3$ .<sup>(18)</sup>

Due to the neck surface instability, the data were analyzed in terms of normalized neck sizes,  $(x/a)$ , defined by the maximum (circumscribed) and minimum (inscribed) circle diameters observed for each neck. The  $(x/a)$  values obtained were between 0.50 and 1.00. Hence, for these neck sizes the small neck assumptions discussed by Coblenz, et al.<sup>(1)</sup> are valid. The variability in  $(x/a)$  for each neck precludes determination of an exact size or time dependence. However, by comparing the slopes of the results when plotted as either  $(x/a)$  versus time (for each sphere size) or  $(x/a)$  versus size (at constant time) the analysis reveals that either surface, boundary or lattice diffusion could be the dominant mechanism. That is, the data are adequately described by  $(x/a) \propto (t/a^4)^{1/5}$  or  $(t/a^3)^{1/5}$  with a slight preference for the first relation. We note that the data also fit  $(x/a) \propto (t/a^4)^{1/7}$  adequately but not as well as the previous two relations and are not well described by  $(x/a) \propto (t/a^3)^{1/4}$ ; this is consistent with the choice of surface and lattice models of Coblenz, et al.<sup>(1)</sup>

The data were subsequently converted to average diffusion coefficients with standard deviations.\* In all cases, we assumed that

\* The diffusivities were calculated from Eqs. (16), (24), and (31) of Ref. (1) except the coefficients  $K$  were corrected for the sphere-plate geometry:  $K(\text{surface}) = 116$ <sup>(19)</sup>;  $K(\text{boundary})$  and  $K(\text{lattice})$  of Eqs. (24) and (31), are increased by a factor of four which results from an increase of the curvature by a factor of two and decreasing the left side of Eq. (22) by a factor of two.

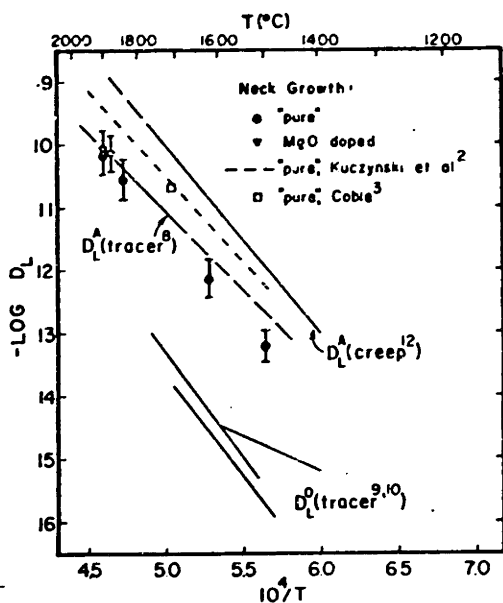


Fig. 2. Lattice Diffusivities

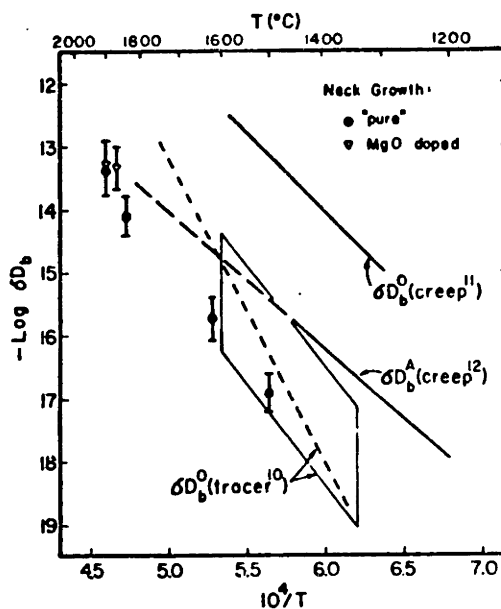


Fig. 3. Boundary Diffusivities

only one mechanism was operative and that the neck surface instability does not completely invalidate the model expressions. As would be expected, given the ranges and inexact size and time dependencies of the observed neck sizes, no systematic variation of the calculated diffusivities with sphere size or length of time (variable  $(x/a)$ ) was observed. Calculated diffusivities for each interpretation were plotted with diffusion coefficients from other sources for comparison in Figs. 2, 3, and 4.

Lattice diffusivities estimated from the experimental data are plotted in Fig. 2 along with those calculated from creep behavior of magnesia saturated alumina<sup>(12)</sup>, tracer values<sup>(8,9,10)</sup> and from the sphere sintering experiments of Kuczynski, et al.<sup>(2)</sup> and Coble.<sup>(3)</sup> Data from the latter two studies were re-evaluated using the Coblenz, et al.<sup>(1)</sup> model set. The apparent  $D_L$  from the present data is less than those found in either of the sintering experiments and has a slightly higher activation energy. The  $\Delta H$  apparent  $\approx 135$  kcal/mole; whereas the re-evaluated  $\Delta H$  from Kuczynski, et al.  $\approx 120$  kcal/mole. The magnitudes and activation energy of the  $D_L$  agree reasonably well with the aluminum lattice tracer diffusivity. However, assuming  $D_L^{Al}$  is rate controlling, magnesium doping is expected to alter  $D_L^{Al}$  and the neck growth rate. In contrast to this, no effect of magnesium doping on the relative neck sizes was observed.

The boundary width-diffusivity products evaluated from the neck growth data are presented in Fig. 3. Also plotted are  $\delta D_b$ 's for both ions as deduced from creep studies<sup>(11,12)</sup> and the  $\delta D_b^O$  determined by Reddy<sup>(10)</sup>. Reddy reported  $\delta D_b^O$  as a set of data points which fall within the box outlined in Fig. 3. No effect of the magnesia was

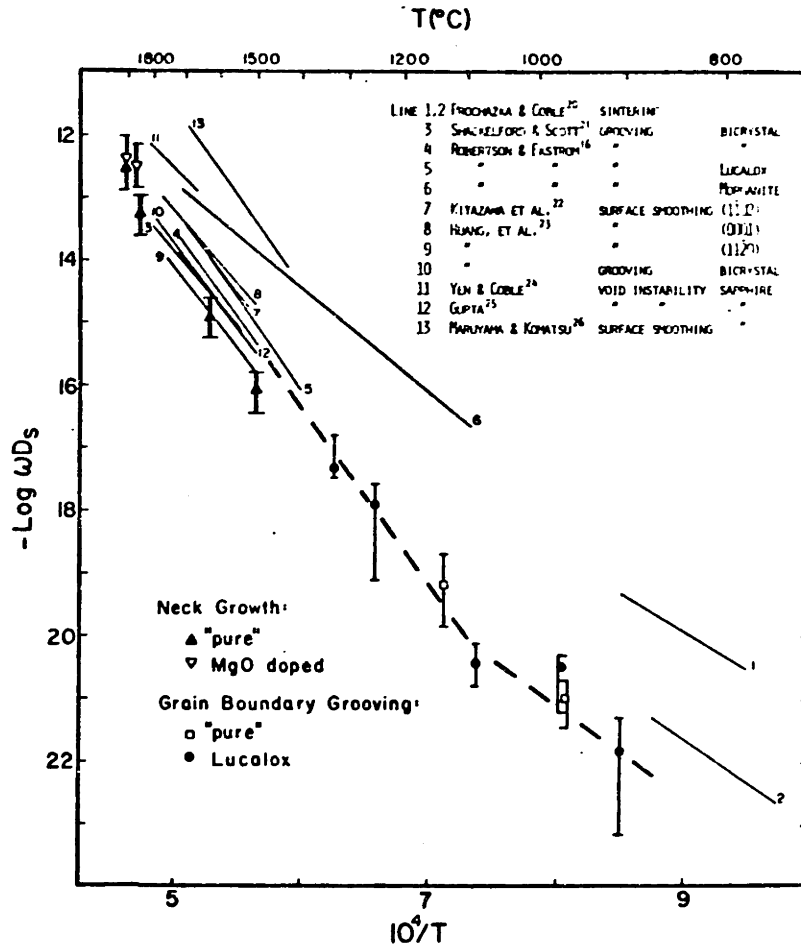


Fig. 4 Surface Diffusivities

evident. The dashed line indicates a coarse fit of this data. The  $\delta D_b$  values deduced from the neck growth data agree reasonably well with the magnitude of Reddy's  $\delta D_b^0$  data, particularly at the lower sintering temperatures. However, the activation energy of Reddy's  $\delta D_b^0$  ( $\sim 220$  kcal./mole) is much larger than that deduced from the present and previous<sup>(2)</sup> neck growth data ( $\sim 160$  kcal./mole).

The other boundary diffusion data comparison is with the  $\delta D_b^{Al}$  values calculated from creep results.<sup>(12)</sup> In this case, the  $\delta D_b$  from sintering agrees well with the extrapolated  $\delta D_b^{Al}$  from creep at the higher temperatures. However, the agreement is poor at lower temperatures. Interestingly, no effect of magnesia doping was observed on the creep strain rates for grain sizes where boundary diffusion was dominant, indicating an apparent insensitivity of  $\delta D_b^{Al}$  to this dopant.

Estimates of the surface width-diffusivity product deduced from neck growth data are plotted in Fig. 4. Also included in this figure are all published  $\omega D_s$  values, measured by a variety of tech-

niques (16,20-26), and recent  $\omega D_S$  data by Dynys, et al. (27) obtained from grain boundary grooving results of high-purity<sup>†</sup>  $Al_2O_3$  and Lucalox (R). The  $\omega D_S$  ranges correspond to the minimum and maximum groove widths determined. The symbols represent the  $\omega D_S$  calculated from the median values of the groove widths. The published values have been re-evaluated to include the assumed surface width, and a constant surface energy (905 ergs/cm<sup>2</sup>) and molecular volume ( $2.2 \times 10^{-23}$  cm<sup>3</sup>). Most of these results lie within a band, a factor of ten wide, defined by lines 8 and 9 in Fig. 4. These two lines were obtained from surface smoothing measurements on (0001) and (11 $\bar{2}$ 0) planes of sapphire by Huang, et al. (23). The only other possible contributing mechanism for these experimental conditions is volume diffusion. However, based on tracer  $D_V$  values for Al the expected volume diffusion contribution to surface smoothing is approximately 1/100 of that measured. Hence this band of  $\omega D_S$  values is regarded as reliable. Grain boundary grooving studies on pure bicrystals (16,21,23) and Lucalox (16) fall within this band, so our present conclusion is that magnesia doping has little effect on  $\omega D_S$ . Additionally, the data from surface diffusion measurements which fall within this band are essentially independent of an air versus vacuum environment. Using the band of published values and our grain boundary grooving results, the heavy dashed line with the break is considered to be a good approximation of  $\omega D_S$ . The high-temperature line has a  $\Delta H = 126$  kcal./mole. For the low temperature line, the magnitude of the grain boundary grooving data was regarded as more reliable than the values deduced from permeability changes in sintered compacts. (20) None of these experiments indicate which ion is rate limiting although it is frequently assumed the  $\omega D_S$  values are for Al diffusion and that oxygen transport, perhaps through the vapor, is easier.

Comparing the  $\omega D_S$  values calculated from the neck growth data with the band of values discussed above shows good agreement except at the lowest sintering temperature, although the apparent activation energy of 160 kcal./mole is high. The results of Kuczynski, et al. (2) and Coble (3) also give similar agreement.

## DISCUSSION

The diffusivities calculated from the neck growth data show reasonable agreement with the magnitudes of either the aluminum lattice tracer or surface diffusion coefficients, especially at the higher sintering temperatures. Either mechanism is consistent with the observed undercut neck profiles. Reasonable agreement was also found with the magnitude of the  $\delta D_b^O$  reported by Reddy at the lower sintering temperatures. For assumed surface or boundary transport paths, the apparent activation energy was significantly different

---

<sup>†</sup> Samples with 220 ppm total anion and cation impurity from W. H. Rhodes, AVCO Corp., Lowell, Massachusetts.

than that for the comparison values. Thus assuming only one transport path, comparisons of the activation energies favors the interpretation that neck growth is controlled by  $D_L^{Al}$ . However, the absence of an effect of magnesia doping on the neck growth rates is inconsistent with lattice diffusion controlled sintering.

The possibility of contributions from several paths must also be considered. There are two potential sources of matter, the grain boundary and the sphere surface. Mass flow from the boundary results in shrinkage and for  $Al_2O_3$  is limited by the slower transport rate of  $\delta D_b^O$  versus the faster of the  $\delta D_b^{Al}$  or  $D_L^{Al}$  transport rates. Alternatively, diffusion from the sphere surface is limited by the slower transport rate of  $\omega D_s^O$  as compared to the larger of the  $\omega D_s^{Al}$  or  $D_L^{Al}$  transport rates. Neck growth will be dominated by the faster of these pairs. By comparing the magnitudes of the diffusivities, neck growth limited by  $\delta D_b^O$  (Reddy) at the lower temperatures and by  $D_L^{Al}$  (tracer) at higher temperatures is suggested for the shrinkage process. Either  $\omega D_s$  or  $D_L^{Al}$  are plausible controlling diffusivities for the coarsening mechanisms.

For most interpretations the neck sizes and hence the calculated diffusivities tend to be smaller than expected. A possible cause is the low dihedral angle which decreases the driving force for each sintering mechanism. Although the existent models do not adequately account for the effects of low dihedral angles when undercutting occurs<sup>(1)</sup>, approximate corrections for a dihedral angle of  $110^\circ$  will increase the estimated diffusivities by a factor of 2 to 50. For the observed neck sizes, calculated boundary or lattice diffusivities may be increased by a factor of 2 to 4. The factor for surface diffusion is of order 10 or more and increases with  $(x/a)$ . These factors would be smaller but important for the  $144^\circ$  to  $160^\circ$  dihedral angles observed for symmetric tilt boundaries<sup>(21)</sup>; more observations of dihedral angles are needed. These approximate changes in the calculated diffusivities improve the  $D_L^{Al} - \delta D_b^O$  data fit at lower temperatures but do not alter the overall interpretation. The  $\omega D_s$  interpretation becomes significantly better at lower temperatures but at higher temperatures appears unable to account for all the neck growth. The effect of the neck surface instability on these comparisons is uncertain, but it is thought that the instability indicates significant transport from the sphere surface.

In comparing diffusivities from various studies we are puzzled that the neck sizes observed are significantly smaller than predicted by the  $\delta D_b^{Al}$  deduced from creep. Although boundary diffusivities estimated from sintering of compacts<sup>(14,28)</sup> are also often lower than this  $\delta D_b^{Al}$ , uncertainties caused by size distribution and packing problems in compacts may undermine confidence in the values of apparent diffusivities from compacts. The smaller than predicted neck sizes suggest that interface control may be important, especially for the sphere-plate geometry for which Cu spheres have been found

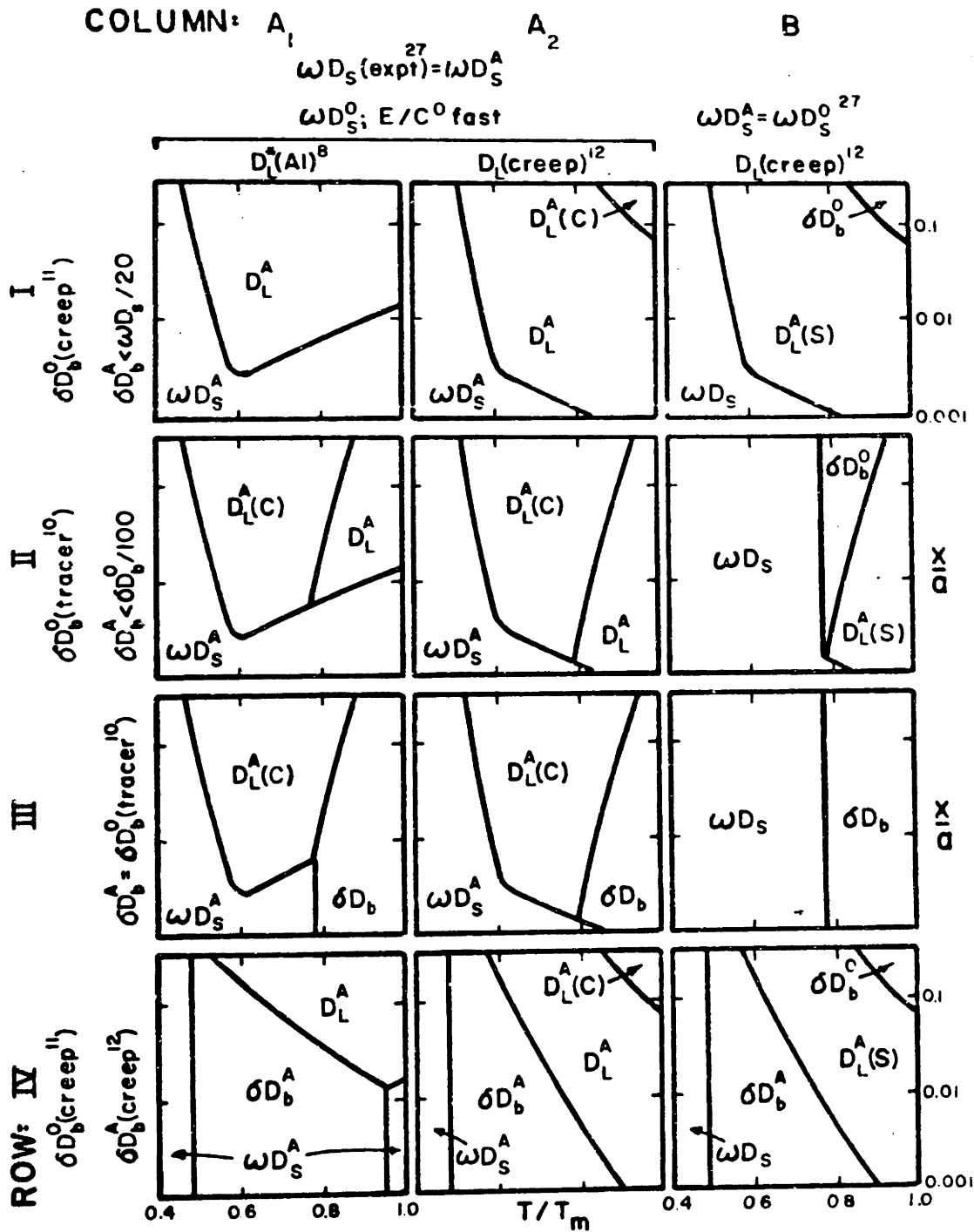


Fig 5. Array of sintering maps for  $\text{Al}_2\text{O}_3$ . The rows are for various possible  $\delta D_b$  values for each ion; the columns represent alternative aluminum lattice diffusivities and oxygen surface transport rates.  $D_L^A(\text{S})$ ,  $D_L^A(\text{C})$ , and  $D_L^A$  denote fields where aluminum lattice diffusion is controlling and only shrinkage, only coarsening, or both shrinkage and coarsening occur, respectively.

to rotate to special orientations while sintering<sup>(29)</sup>. Presumably rotation to special boundaries can lower the  $\delta D_b$  for either species or cause difficult defect annihilation or creation. The net result of these is that shrinkage mechanisms are inhibited.

A more troublesome aspect of the diffusivities used for the above comparisons is that predicted behavior based on these values is substantially different and often not in agreement with observed behavior. In order to elaborate the implications of the various plausible  $\delta D_b$  values, a matrix of sintering diagrams has been formulated as shown in Fig. 5. In the rows, we alternately assumed that  $\delta D_b^O$  was Reddy's value or that from creep and  $\delta D_b^{Al}$  was of comparable or lower magnitude than  $\delta D_b^O$  (Reddy) or the value from creep. Two comparisons are introduced in the columns. One is the effect of rapid surface oxygen transport compared to an assumed equal  $\omega D_s$  value for both ions. The other shows the behavior for the two plausible  $D_L^{Al}$  values. The intent of this array of maps is to pictorially represent the implications of these various possible diffusivities with respect to the behavior of sphere-plate experiments and powder compacts for the range of possible diffusion coefficients.

The array of sintering maps shown is for the initial stage sintering of 3.0 millimeter spheres. These diagrams are formulated<sup>(7)</sup> by equating the neck growth rate expressions for any two mechanisms. The resulting lines define fields in which one transport path dominates or controls the sintering process, but is not necessarily the only contributing mechanism. Transition temperatures for boundary to surface diffusion control are size invariant. However, the  $(x/a)$  values for a transition from either boundary to lattice or surface to lattice diffusion controlled neck growth scale approximately with inverse particle size. Decreasing the sphere size by a factor of ten increases the  $(x/a)$  value at which the transition occurs by approximately a factor of ten. Hence, the fields at the bottom of the maps indicate the controlling sintering mechanism for 10 $\mu$ m sized powder at the end of the initial stage (beginning of the intermediate stage).

Of the diffusivities considered, the various  $\delta D_b$  values provide the most significant differences and conflicts with observations. Both  $\delta D_b$ 's deduced from diffusional creep are much larger than Reddy's value. Although studies of metals indicate that diffusivities deduced from diffusional creep may be a factor of 3 to 4 too high<sup>(30)</sup>, this factor is insufficient to account for the discrepancy between these values. If Reddy's value of  $\delta D_b$  is correct, two problems are indicated. First, most of the creep rates reported in a dozen or so studies<sup>(11,12)</sup> are 1 to 4 orders of magnitude higher than oxygen transport would allow. Second, lattice diffusion kinetics are frequently indicated by the grain size dependence and the apparent diffusivities for medium grain sized  $Al_2O_3$ <sup>(11,12,31-33)</sup>. This can



only be possible if  $\delta D_b^O / \delta D_b^{Al} > 100$  (12), which would require a much lower  $\delta D_b^{Al}$  than indicated or  $\delta D_b^O$  higher than the tracer value. The situation is similar for sintering, Fig. 5. If  $\delta D_b^O < \delta D_b^{Al}$  (row III), boundary, but not lattice controlled kinetics would be predicted to control shrinkage. Assuming Reddy's value of  $\delta D_b^O$  (rows II or III) coarsening mechanisms by either  $D_L^{Al}$  or  $\omega D_s$  would dominate shrinkage mechanisms below 1500°C for all particle sizes. Assuming large  $\delta D_b^O$  and small  $\delta D_b^{Al}$  (row I), coarsening dominates shrinkage below 1500°C for micron sized particles. For submicron particles virtually no shrinkage would be expected below 1500°C for any of the assumptions in rows I-III, i.e., small  $\delta D_b^{Al}$  or  $\delta D_b^O$  (Reddy). The predictions from rows I-III are incorrect because shrinkage is observed below 1100°C (28). The most satisfying set of  $\delta D_b$ 's with respect to shrinkage of powder compacts and creep behavior is that deduced from creep studies (row IV). We do not understand the extreme disagreements between the  $\delta D_b$  values indicated by mass transport and tracer studies.

For the sphere-plate experiments the behavior appears to be more like that indicated in rows I, II, or III. We do not believe this supports the tracer value of  $\delta D_b^O$  for general grain boundaries. Instead we are inclined to attribute this behavior to the formation of special boundaries with low  $\delta D_b^{Al}$  or poor source/sink efficiency in these model experiments.

For micron sized powder compacts, the behavior indicated by row IV indicates surface diffusion would be dominant at very low temperatures. Above 800°C the sintering would be dominated by boundary diffusion controlled shrinkage, with some coarsening from  $\omega D_s$ . At higher temperatures and larger neck sizes, surface (coarsening only) or lattice diffusion (coarsening and shrinkage) make increasingly important contributions. Simultaneous shrinkage and coarsening is then predicted and is experimentally observed.

An effect of rapid oxygen surface transport is to allow coarsening controlled by  $D_L^{Al}$  to dominate neck growth. At large neck sizes for assumed large  $\delta D_b^O$ , it would normally be expected that a transition from  $D_L^{Al}$  to  $\delta D_b^O$  controlled shrinkage should occur. Rather a transition from the  $D_L^{Al}$  controlled coarsening and shrinkage regime to a  $D_L^{Al}$  controlled coarsening field occurs. Alternatively, when both ions have the same  $\omega D_s$  the lattice fields are for transport from the grain boundary only (this is equivalent to surface diffusion being limited by oxygen transport). In this case, shrinkage with no undercutting would prevail when  $D_L^{Al}$  is dominant. Our observations of undercutting indicate that either  $\omega D_s^{Al}$  is important for all our experiments or that there is either a large  $\omega D_s^O$  or rapid vapor transport of oxygen which allows  $D_L^{Al}$  controlled undercutting.

The most apparent effect of increasing  $D_L^{Al}$  is to enlarge the  $D_L^{Al}$  fields. However, an interesting situation is seen for the case of the smaller  $D_L^{Al}$  (tracer) and  $D_b^{Al}$  (creep), row IV-column A.

Here, due to the break in the proposed  $\omega D_s$  curve,  $\omega D_s$  dominates both at low and high temperatures and obviously is never completely negligible in the  $\delta D_b^{Al}$  fields.

#### SUMMARY

Neck growth in sphere-plate sintering of  $Al_2O_3$  is most probably controlled by aluminum lattice or surface diffusion. The lattice diffusion contribution may represent transport primarily from the sphere surfaces rather than the grain boundaries. Inconsistencies among the published data on boundary diffusion of Al and O exist which preclude an unambiguous understanding of the sintering behavior of  $Al_2O_3$ .

The sintering rates calculated from our neck growth data are lower than those predicted assuming control by  $\delta D_b^{Al}$ . These lower rates may reflect the development of special boundaries in these sphere-plate experiments which have low  $\delta D_b$ 's or are inefficient vacancy sinks or interstitial sources. The behavior of powder compacts seems to be different than indicated by the sphere-plate experiments in that boundary diffusion controlled shrinkage may be more important in powder compacts.

#### ACKNOWLEDGEMENTS

The authors gratefully acknowledge the skill and patience of Mrs. D. Borsuk in preparation of this manuscript. This work was supported by D.O.E. contract #EY-76-S-02-2390.A002.

#### REFERENCES

1. W. S. Coblenz, J. M. Dynys, R. M. Cannon, and R. L. Coble, in this proceedings.
2. G. C. Kuczynski, L. Abernethy, and J. Allan, in Kinetics of High-Temperature Processes, Ed. by W. D. Kingery, M.I.T. and Wiley, 1959.
3. R. L. Coble, J. Am. Ceram. Soc., 41, 55 (1958).
4. JANAF Thermochemical Tables, Second Edition, D. R. Stull and H. Prophet, NSRDS-NBS 37, 1971.
5. L. U. Ogbuji, T. E. Mitchell, and A. H. Heuer, in this proceedings.
6. C. S. Morgan and V. J. Tennery, in this proceedings.
7. M. F. Ashby, Acta Metal., 22, 275 (1974).
8. A. E. Paladino and W. D. Kingery, J. Chem. Phys., 37, 957 (1962).
9. Y. Oishi and W. D. Kingery, J. Chem. Phys., 33, 480 (1960).
10. K. P. R. Reddy, Ph.D. Thesis, Case Western Reserve University, 1979.
11. P. A. Lessing and R. S. Gordon, J. Mat. Sci., 12, 2291 (1977).

12. R. M. Cannon and R. L. Coble, in Deformation of Ceramic Materials, Ed. by R. E. Tressler and R. C. Bradt, Plenum, N.Y. 1974.
13. A. E. Paladino and R. L. Coble, J. Am. Ceram. Soc., 46, 133 (1963).
14. W. R. Rao and I. B. Cutler, J. Am. Ceram. Soc., 56, 588 (1973).
15. R. D. Bagley, I. B. Cutler, and D. L. Johnson, J. Am. Ceram. Soc., 53, 136 (1970).
16. W. M. Robertson and F. E. Ekstrom, in Kinetics and Reactions in Ionic Systems, Ed. by T. J. Gray and V. D. Frechette, Plenum, N.Y., 1969.
17. R. M. Cannon, A. H. Heuer, N. J. Tighe, in press, J. Am. Ceram. Soc.
18. R. L. Coble and J. E. Burke, in Progress of Ceramic Science, Vol. 3, Ed. by J. E. Burke, Macmillan, N.Y., 1963.
19. F. A. Nichols and W. W. Mullins, J. Appl. Phys., 36, 1826 (1965).
20. S. Prochazka and R. L. Coble, Phys. Sintering, 2, 15 (1970).
21. J. F. Shackelford and W. D. Scott, J. Am. Ceram. Soc., 51, 688 (1968).
22. K. Kitazawa, I. Komaki, K. Matsukawa, and K. Fueki, to be published in the J. Jap. Ceram. Soc.
23. F. H. Huang, R. A. Henrichsen, and Che-Yu Li, in Sintering and Catalysis, Ed. by G. C. Kuczynski, Plenum, N. Y., 1975.
24. C. F. Yen and R. L. Coble, J. Am. Ceram. Soc., 55, 507 (1972).
25. T. K. Gupta, J. Am. Ceram. Soc., 61, 191 (1978).
26. T. Maruyama and W. Komatsu, J. Am. Ceram. Soc., 58, 338 (1975).
27. J. M. Dynys, R. L. Coble, and R. M. Cannon, to be published.
28. W. S. Young and I. B. Cutler, J. Am. Ceram. Soc., 53, 659 (1970).
29. H. Mykura, Acta Metal., 27, 243 (1979).
30. B. Burton, Diffusional Creep in Polycrystalline Materials, Diffusion and Defects Monograph #5, Trans. Tech. Publications, Bay Village, O, (1977).
31. R. C. Folweiler, J. Appl. Phys., 32, 773 (1961).
32. S. I. Warshaw and F. H. Norton, J. Am. Ceram. Soc., 45, 479 (1962).
33. W. R. Cannon and O. D. Sherby, J. Am. Ceram. Soc., 60, 44 (1977).

Appendix II. Correction for the Specimen Tilt in the SEM

A representation of the image formation geometry in the SEM is shown in Figure A1 (Hearle et al. (1972)) where the specimen tilt axis is parallel to the flat sample surface and normal to the optic axis; F is the focal point of the electron beam. It is shown here that the error in determining the distance ac by use of the right-triangle ehk is small;  $ac = eg/M$ , where M = the magnification. An upper limit for the angle  $\epsilon$  is:

$$\epsilon = \tan^{-1} \frac{\text{object size}}{\text{working distance}} = \tan^{-1} \frac{ad}{bF} = 0.86^\circ ,$$

where the maximum value of ad is  $30\mu\text{m}$  and the minimum value for bF is 2mm. The greatest error occurs for the maximum sample tilt used,  $\theta' = 60^\circ$ . Consequently,  $eh = 2ek$ ,  $hk = \sqrt{3}/2 ek$ , where ek is the measured value. Since  $\epsilon$  is small,  $ih \approx hk \sin \epsilon$  and  $gh \approx ih \csc 30^\circ$ . Using the appropriate quantities,  $gh/eh = \sqrt{3}/2 \sin \epsilon = 1.3\%$ . Using more typical values for ad and bF,  $gh/eh \ll 1\%$ . Tilt corrections are needed for measurements parallel to the tilt axis.

The largest error in using the SEM for measurement of the groove widths results from error in tilt angle. Using equation (28), the maximum error occurs when  $\phi' = 0$ , then  $W \propto 1/\cos \theta'$ . A  $2^\circ$  variation of the tilt angle results in an error of approximately 6% when  $\theta' = 60^\circ$ , for  $\theta' = 45^\circ$ , the error is approximately 4%.

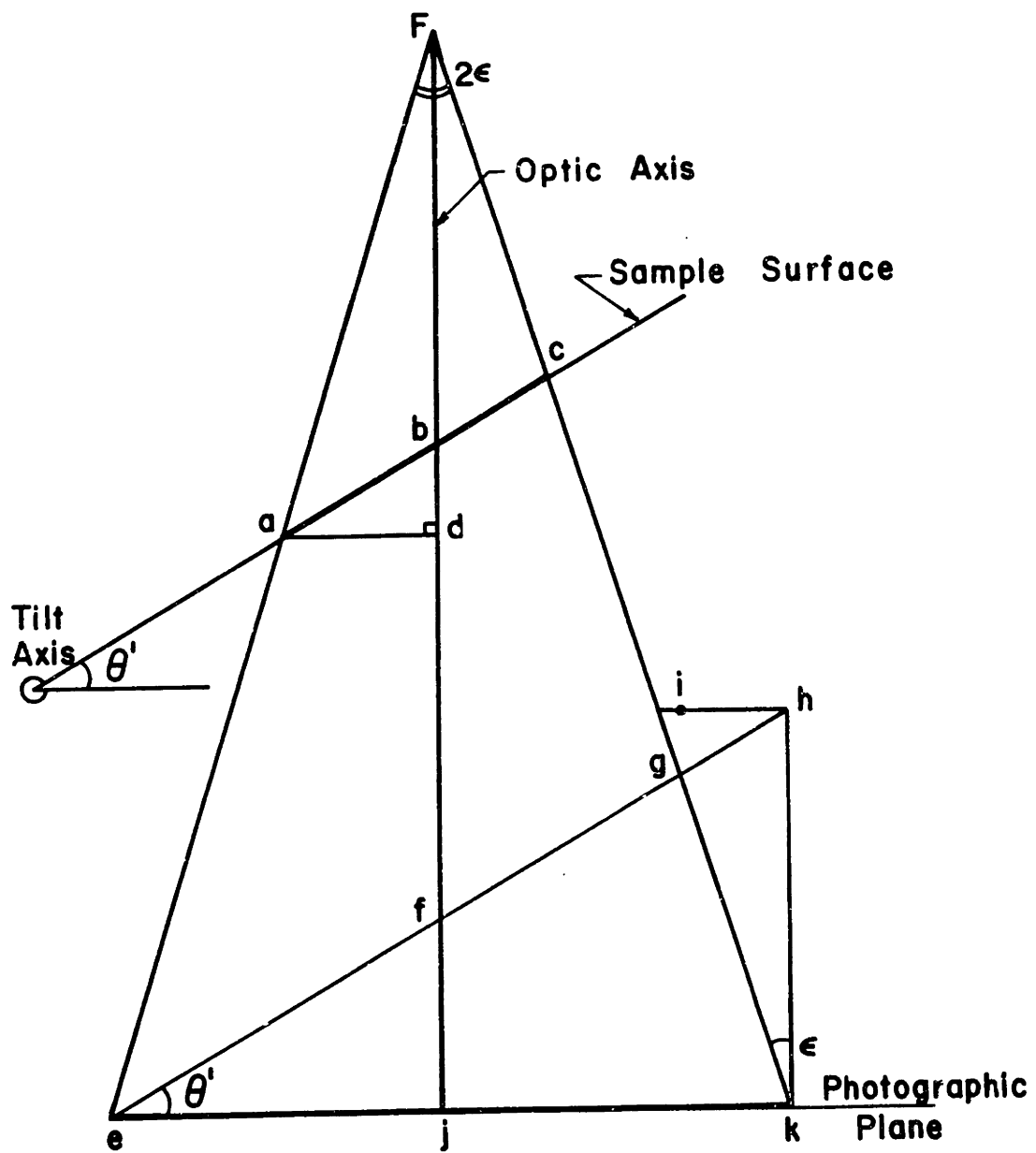


Figure A1 SEM projection geometry

Appendix III. Comparison of Thermal Groove Widths Measured by the SEM-Technique with Two-Beam Interferometry.

The thermal groove widths of specific boundaries, measured by the SEM-technique and by 2-beam interferometry, were compared, see Table A1. Good agreement is found for both samples, although the agreement is better on the sample which has a faceted surfaces, GBG29F (ADL material).

Table A1

<u>Sample</u>	<u>Boundary</u>	<u><math>\theta'</math></u>	<u><math>\phi'</math></u>	<u>Width-Eqn(28)</u>	<u>Width (2-beam interferometry)</u>
GBG27F	3-1	45°	51°	5.91-7.49	6.25-6.46
	3-1	45°	8°	6.10-7.04	"
	3-1	60°	0°	6.25-6.87	"
	3-1	SEM tilt correction	0°	5.94-6.25	"
	31-3	60°	5°	6.87-7.50	6.74-7.10
	4-1	60°	0°	7.73-9.02	8.33-8.54
	4-2	60°	20°	5.10-6.37	5.83-6.04
	4-3	60°	30°	4.00-5.33	4.58-4.79
GBG29F	2a	45°	30°	2.31-2.48	2.20-2.40
	2c	45°	62°	2.43-2.87	2.40-2.80
	6a	45°	45°	2.30	2.40-2.60
	6b	45°	25°	2.10-2.32	2.40
	6c	45°	48°	2.08	2.00
	6d	45°	25°	2.08-2.18	2.00-2.40
	6e	45°	5°	1.74-1.85	1.60-1.80

Appendix IV. Correction for Temperature Drift, GBG27 and 29.

The temperature drifted during the final time interval of the experiments where the rates of thermal groove formation on individual boundaries were being monitored, upward by 15° experiment GBG27 and 15°C downward for GBG29. An upper bound on the effect of this can be calculated by assuming the altered temperature for the entire time period, and by knowing the diffusion mechanism and its activation energy.

$$W_*^n = k_1(t_1 + t_2)$$

$$W^n = k_1t_1 + k_2t_2 \quad ,$$

where  $n = 3, 4$  corresponds to volume or surface diffusion, respectively;  $t_i$  time interval the experiment;  $k_i$  the kinetic coefficient at  $T_i$ ;  $W$ , the observed thermal groove width; and  $W_*$  is the groove width which would have been obtained if the entire experiment were at the initial temperature. For this case,  $t_1/(t_1+t_2) = 1/2$ . Values of the ratio,  $W/W_*$ , have been calculated for a range of plausible activation energies, where  $T_2 > T_1$ , see Table A2. The largest conceivable error is 7%; this value has been used to extend the ranges of certainty for the appropriate data as plotted in Figures 31 and 32. Clearly, the resulting error does not significantly alter the tendency of many of the lines to exhibit upward curvature.

Table A2. Ratios Showing the Increased Thermal Groove Width Due to a Step Increase of 15°C for a Surface or Lattice Diffusion Process Assuming Plausible Activation Energies.

$$W/W_* = \left[ 1/3 + 2/3 \exp \frac{Q}{R} \left( \frac{1}{T_1} - \frac{1}{T_2} \right) \right]^{1/n}$$

<u>Q(kcal./mole)</u>	<u>n = 4</u>	<u>n = 3</u>
100	1.037	1.050
110	1.041	1.055
120	1.045	1.061
130	1.049	1.066
140	1.053	1.072



BIOGRAPHICAL NOTE

Joseph Michael Dynys was born on 14 July 1954 in Jamestown, New York. After graduating from Jamestown High School in 1972, he attended Alfred University where he received a Bachelor of Science in Ceramic Science and Bachelor of Arts in Chemistry, both in 1976. He married Janet Michelle Servoss in 1972 and is now the father of four children. The author has accepted employment at the IBM Corporation, located at East Fishkill, New York. He is a member of the American Ceramic Society, Sigma Xi and Keramos.